GW APPROXIMATION STUDY OF COMPTON PROFILES OF SOME TRANSITION METAL OXIDES AND SEMICONDUCTORS

SIDIQ BIN MOHAMAD KHIDZIR

FACULTY OF SCIENCE
UNIVERSITY OF MALAYA
KUALA LUMPUR

2018

GW APPROXIMATION STUDY OF COMPTON PROFILES OF SOME TRANSITION METAL OXIDES AND SEMICONDUCTORS

SIDIQ BIN MOHAMAD KHIDZIR

**THESIS SUBMITTED IN FULFILMENT OF THE
REQUIREMENTS FOR THE DEGREE OF
DOCTOR OF PHILOSOPHY**

**DEPARTMENT OF PHYSICS
FACULTY OF SCIENCE
UNIVERSITY OF MALAYA
KUALA LUMPUR**

2018

UNIVERSITI MALAYA

ORIGINAL LITERARY WORK DECLARATION

Name of Candidate: **SIDIQ BIN MOHAMAD KHIDZIR**

Registration/Matric No: **SHC100086**

Name of Degree: **DOCTOR OF PHILOSOPHY**

Title of Project Paper/Research Report/Dissertation/Thesis (“this Work”):

GW APPROXIMATION STUDY OF COMPTON PROFILES OF SOME TRANSITION METAL OXIDES AND SEMICONDUCTORS

Field of Study: **THEORETICAL PHYSICS**

I do solemnly and sincerely declare that:

(1) I am the sole author/writer of this Work;
(2) This Work is original;
(3) Any use of any work in which copyright exists was done by way of fair dealing and for permitted purposes and any excerpt or extract from, or reference to or reproduction of any copyright work has been disclosed expressly and sufficiently and the title of the Work and its authorship have been acknowledged in this Work;
(4) I do not have any actual knowledge nor do I ought reasonably to know that the making of this work constitutes an infringement of any copyright work;
(5) I hereby assign all and every rights in the copyright to this Work to the University of Malaya (“UM”), who henceforth shall be owner of the copyright in this Work and that any reproduction or use in any form or by any means whatsoever is prohibited without the written consent of UM having been first had and obtained;
(6) I am fully aware that if in the course of making this Work I have infringed any copyright whether intentionally or otherwise, I may be subject to legal action or any other action as may be determined by UM.

Candidate’s Signature　　　　　　　　Date:

Subscribed and solemnly declared before,

Witness’s Signature　　　　　　　　Date:

Name:

Designation:

GW APPROXIMATION STUDY OF COMPTON PROFILES OF SOME TRANSITION METAL OXIDES AND SEMICONDUCTORS

ABSTRACT

Ground state Density Functional Theory (DFT) calculations via the Localized Density Approximation (LDA) functional has shortcomings in explaining experimental Compton profiles, typically seen in disagreement of the lower momenta regions as a result of an incomplete description of correlation effects. In constructing the momentum densities via the LDA functional, which will subsequently be used to construct the Compton profiles, the input required is the occupation number density which is dependent on the initialized state. Obtaining the band structure, we can confirm the largest contributing orbitals to the momentum density. Knowledge of the contributing orbital states alone is inadequate to completely explain the shortcomings behind the LDA momentum density. Using the GW (Green's function-Dielectric screening) Approximation, the momentum density is constructed from the spectral function which is a Lorentzian as a function of self-energy. This self-energy term itself is dependent on the dielectric screening term. In this work, Compton profiles constructed via the GW Approximation will be shown to provide not only greater insight via the dielectric screening and self-energy terms, it will also provide better agreement to experiment compared to the LDA Compton profiles. In our study of NiO, we observe that the sum of absolute values of the difference profiles is smaller in the case of GWA compared to LDA indicating generally better agreement. For TiO_2, we observe that the GWA reproduces a smaller difference profile at higher momenta compared to LDA. To further investigate the well known strongly correlated system NiO, we have compared it to other Mott insulators FeO and CoO. We observe that NiO has twice broadened spectral functions compared to FeO and CoO. This has been attributed to the twice larger d-orbital contribution as observed in the partial density of states. The NiO momentum density is more occupied in the low momentum region compared to FeO and CoO and this confirms the role of NiO as a strongly correlated system. The amplitude of the anisotropy of NiO is seen to be larger than FeO and CoO. This is attributed to asymmetry of valence electron profiles induced by spectral functions and vertex corrections. In our study of ZnSe, we observe between 0-1.5 a.u, there is better agreement to the previous study via the GWA difference profile compared to the LDA difference profile.

Keywords: Compton Profile, GW Approximation, Density Functional Theory

KAJIAN PENGHAMPIRAN GW KE ATAS PROFIL COMPTON UNTUK BERBERAPA OXIDA LOGAM PERALIHAN DAN SEMIKONDUKTOR

ABSTRAK

Pengiraan teori fungsian ketumpatan keadaan (DFT) pada peringkat tenaga terendah melalui fungsian penghampiran ketumpatan keadaan setempat (LDA) memiliki kekurangan dalam menerangkan pemerhatian eksperimen profil Compton, di mana perbezaan dilihat pada bahagian momentum kecil disebabkan ketaksempurnaan penghuraian kesan korelasi. Dalam pembinaan ketumpatan keadaan momentum melalui fungsian LDA, yang akan seterusnya diguna untuk membina profil Compton, kemasukkan yang diperlukan adalah ketumpatan nombor penghunian yang bergantung pada keadaan awal. Selepas memperolehi struktur jalur, kita boleh mengenalpasti penyumbangan orbital terbesar kepada ketumpatan momentum. Pengetahuan penyumbang keadaan orbit sendiri tidak mencukupi untuk menerangkan kekurangan pada ketumpatan momentum LDA. Menggunakan penghampiran GW (fungsi Green-penghadang dielektrik), ketumpatan momenta dibina dari fungsi spektra yang merupakan fungsi Lorentzian yang bergantung pada swatenaga. Swatenaga ini pula bergantung pada penghadangan dielektrik. Di dalam kerja ini, profil Compton akan dibina dari penghampiran GW yang akan ditunjukkan memberi bukan sahaja gambaran yang lebih besar dengan penggunaan sebutan penghadangan dielektrik dan swatenaga, kita juga akan perolehi persetujuan yang lebih baik dengan eksperimen berbanding profil Compton LDA. Di dalam pengajian NiO, kita perhati jumlah nilai mutlak profil bezaan lebih kecil dalam kes GWA berbanding LDA menunjukkan persetujuan lebih tinggi berbanding LDA. Bagi TiO_2, kita perhati bahawa GWA menujukkan profil bezaan yang lebih kecil pada momenta tinggi berbanding LDA. Untuk menyelidiki sistem korelasi kuat NiO dengan lebih lanjut, kita membandingkannya dengan sistem penebat Mott yang lain seperti FeO dan CoO. Kita memerhati bahawa NiO memiki fungsi spektra yang dua kali lebih tebal berbanding FeO dan CoO. Ini disebabkan sumbangan orbital-d adalah dua kali ganda dalam NiO seperti yang dilihat dari ketumpatan keadaan separa. Ketumpatan momenta NiO lebih dihuni di rantau momentum rendah berbanding FeO dan CoO dan ini mengesahkan peranan NiO sebagai sistem korelasi kuat. Amplitud anisotropi NiO dilihat lebih besar berbanding FeO dan CoO. Ini disebabkan asimetri profil elektron valens disebabkan fungsi spektra dan pembetulan verteks. Di dalam kajian ZnSe, kita perhatikan bahawa diantara 0-1.5 a.u, terdapat persetujuan lebih baik berbanding kajian sebelum ini dengan membanding profil bezaan GWA dan LDA.

Kata Kunci: Profil Compton, Penghampiran GW, Teori Fungsian Ketumpatan

ACKNOWLEDGEMENT

The completion of this work is greatly assisted by the kind assistance of a number of Professors and colleagues. The first being my supervisor, Professor Dr. Wan Ahmad Tajuddin, who has given me the freedom to pursue topics of my own interest and inclinations, to which I naturally gravitated towards first principles techniques. Professor Dr. David Bradley from the University of Surrey, who suggested the topic of Compton profiles which allowed me to zero-in on an end result from the first principles techniques. Dr. Valerio Olevano from CNRS Grenoble, who has kindly guided me towards the nuances behind obtaining the Compton profile from first principles. My lab partners, collaborators and friends, Hadieh Monajemi, Ephrance Abu Ujum, Amir Fawwaz, Anuar Alias, Naharuddin Mustapha, Akmal Ashraf, Fadeli Halid, Khairul Nizam Ibrahim, Khairunnisa Raman and Fahmi Maulida who have greatly assisted in this work by discussions or in various other processes of completing this work. I would lastly like to provide the greatest acknowledgement to my Mother, Father and Sister who have supported me through the ups and downs of this journey. I finally dedicate this work to my dear late Brother.

TABLE OF CONTENTS

LIST OF FIGURES

LIST OF TABLES

LIST OF APPENDICES

LIST OF SYMBOLS AND ABBREVIATIONS

$\psi^{\dagger}(x)$: Annhilation Operator

μ : Chemical Potential

$\psi(x)$: Creation Operator

$S(q,\omega)$: Dynamic Structure Factor

V_{xc} : Exchange Correlation Potential

ω : Frequency

$G(x,x')$: Green’s Function

H_o : Hamiltonian

V_H : Hartree Potential

E_{ion} : Ionic Potential

q : Modulus of Transferred Momenta

$n(p)$: Momentum Density

p_j : Momentum Operator

ε : Polarization Vector

Σ : Self-energy

H_{int} : Semiempirical Interaction Hamiltonian

$d═/d\omega$: Thomson Cross Section

$G_2(1,2,3,4)$: Two Particle Green's Function

$A(r_j)$: Vector Potential

Γ : Vertex Correction

k	:	Wave Vector
CIF	:	Crystallographic Information File
DFT	:	Density Functional Theory
DDSCS	:	Double Differential Scattering Cross Section
FFT	:	Fast Fourier Transform
GWA	:	Green's Function-Dielectric Screening Approximation
KS	:	Kohn-Sham
LPC	:	Lam-Platzman Correction
MBPT	:	Many Body Perturbation Theory
PDOS	:	Partial Density of States
PPM	:	Plasmon Pole Model
QPRF	:	Quasiparticle Renormalization Factor
RPA	:	Random Phase Approximation
SCF	:	Self-Consistent Field
TMO	:	Transition Metal Oxides

CHAPTER 1 : INTRODUCTION

1.1 Background

Understanding the bulk structure of matter is fundamental in the study of materials science and devices. The field of study that describes the fundamental properties of these bulk structures is Fermiology. It discusses the Fermi surface which is an abstract boundary in reciprocal space useful for predicting the thermal, electrical, magnetic, and optical properties of metals, semimetals, and doped semiconductors. It is well known that a probe of the Fermi surface is via Compton scattering (Bansil et al., 1997).

The Compton effect refers to the Doppler broadening of inelastically scattered x-ray radiation where information on the initial momentum density of recoiled electrons can be obtained. A projection of this momentum density onto a line through the origin is defined as the Compton profile. Momentum density is defined as the probability to observe electrons with momentum p. Experimentally, this term can be obtained from performing an x-ray Compton scattering experiment in which the momentum density is reconstructed from the observed differential scattering cross section. Using intense synchrotron radiation allows to image a momentum density a few percent of the Fermi momentum. Specifically, the electron wavefunction in *k-space* is observed since it samples the bulk properties of the sample making it a very useful tool for studying the Fermi surface, particularly studying quasiparticles. If the energy and momentum transfers of the probe energies are larger than the binding energies of the sample, in which the impulse approximation is obeyed, we can obtain quasiparticle peaks, satellite structure, discontinuity and renormalization factor from the momentum density which can be used to obtain insight on electron-electron correlation around the Fermi surface break. We describe in detail these topics in Section 2.1 of Chapter 2.

1.2 Problem Statement and Objective

Theoretical studies of momentum densities takes into account valence energy bands, Fermi surface topology and breaks, electron correlation effects and character of wavefunctions. Discrepancies between experiment and theory are attributed to ignoring correlation effects in the independent particle model. Specifically, ground state calculations are able to explain the overall shape and fine structures of the observed profile but the momentum densities at the origin are greater than experimental values at the origin but opposite in the high momentum case and a renormalization of the height of break at the Fermi surface is seen. Overall, a momentum density resembling a step function is observed in accordance with the one electron approximation at zero temperature. Excited state calculation on the other hand describes long range correlation effects and valence band narrowing due to the dynamical screening effects. These effects broaden fine structures in the Compton profile which are observed to be sharper in the ground state. This makes the momentum density which is expected to follow a step function due to a non-interacting system be a continuous function. It is also possible to study individual spin states in which the Pauli exclusion principle can be observed. These traits make the Compton profile a sensitive test of validity of band structure calculations. The alkali and alkali-earth metals in particular have been actively studied for their correlation effects as they are closest to the homogeneous electron gas and have isotropic momentum distributions. The use of the GW Approximation is said to improve the comparison to observation for the Compton profile (Schulke et al., 1996). Compton profiles for Li, Be, Na, Cr , Ni and Cu have been obtained from the GW Approximation. For shallow d-orbital systems such as transition metals, observation of these terms indicate a breakaway from an equilibrium ground state theory. This can be seen in momentum density calculations where it is observed that there is some agreement in high momentum region but discrepancies in the low momentum region. This problem has been improved with the Lam-Platzmann correction. Nevertheless, the agreement of theory to experiment from using this correction shows small improvements. Furthermore, there seems to be the observation of fine structures in theoretical Compton profiles compared to experiment. We describe in detail these topics in Section 2.1-4 of Chapter 2.

1.3 Scope of Calculations

Nickel Oxide (NiO) has been widely studied as the prototypical system undergoing metal-insulator transition (Imada et al., 1998) and Titanium dioxide (TiO_2) has been widely studied as a wide bandgap semiconductor (O'regan et al., 1991). Recently, these oxides have been actively studied as resistive random access memories (ReRAM) sandwich layer. ReRAMs have emerged as a strong candidate to replace FLASH-based memories as the need to construct integrated circuits go beyond the CMOS architecture. In studies concerning these systems, the transition metal oxide is treated as an ion conducting layer and is sandwiched between two inert metal electrodes. The mechanism behind its operation is named resistive switching. It is achieved by the formation and destruction of a conductive filament in the dielectric between two electrodes (Akinaga et al., 2010). The device works by firstly having the insulating switching material be in a high resistance state. By applying the electroforming voltage, a conductive filament is formed which creates a low resistance state. When a lower voltage is applied, the conductive filament is destroyed and the device is returned to a high resistance state (Jeong et al., 2012). The central tools used to visualize the conductive filament in all these studies start with the Kohn-Sham electron wave function obtained from a first principles density functional theory calculation, followed by the electron localization function which measures the likelihood to find an electron near a reference electron at a given point with the same spin (Becke et al., 1990). This would then be used to perform the Bader charge density analysis which is an algorithm to integrate the electronic charge density around ions (Bader, 1990). This method however neglects strongly correlated effects which is relevant to the study of charge transfer. This is because the construction of the charge density from a ground state calculation with a Hubbard term, *U* as has been the case in the above mentioned studies will not adequately take into account electron correlation commonly studied as self-energy effects. Its importance has been highlighted by Peng (Peng et al., 2012) who has determined that strongly correlated effects in a NiO supercell affect transport properties during resistive switching. Other highlights regarding correlation effects include the construction of other beyond CMOS devices, for example the application of VO_2 to construct a metal insulator transition tunnel junction (Martens et al., 2012; Huefner et al., 2014). Studying the momentum density instead of just the charge density of these oxides should provide a more accurate description of the charge transfer. In Section 4.1 of Chapter 4, we firstly calculated the excited state and ground state band structure calculations for NiO and TiO_2. We then calculated the Fermi energy and Fermi momenta which will be subsequently used to obtain the spectral functions. These functions will be used to obtain the momentum density. We then compared and explained the differences between GW Approximation and ground state momentum densities. Finally we use the momentum densities to construct the Compton profile. The profiles will be analyzed in terms of difference profiles and anisotropy. We end this section by discussing the quasiparticle renormalization factor.

The late TMOs FeO, CoO and NiO are said to be the prototypical Mott insulators. Above the Neel temperature, these oxides are paramagnetic insulators (Rodl et al., 2012). Below the Neel temperature they are known to be antiferromagnetic insulators where MnO and NiO have underestimated band gaps using LDA/GGA electronic structure calculations while FeO and CoO have been characterized as antiferromagnetic phased metals (Massida et al., 1997). Antiferromagnetic ordering is said to lower the symmetry of the FCC lattice in which certain lattices degenerated to paramagnetic state split by antiferromagnetic field at low temperature (Peter et al., 1993). In Section 4.2 of

Chapter 4., we are interested in studying the effects of a self-energy correction on the late TMOs. These effects can be studied by observing the smearing of the occupational number before and after the Fermi break. We account for the differences between LDA and GWA via the correlation correction. This correction is analogous to the Lam-Platzman correction (LPC) which is defined as the difference between the occupation function for a non-interacting and homogeneous interacting electron gas, effectively estimating the correlation effects in the Compton profile. We can further analyze this promotion of electrons by studying the directional differences which is a measure of anisotropy. Anisotropy is strongly dependent on the Fermi surface and can be used to locate the position of oscillations in the Fermi surface.

Zinc monochalcogenides are the prototype II-VI semiconductors. These semiconductor compounds can be employed as the base materials for optical devices such as visual displays, high density optical memories, transparent conductors, solid state laser devices, photodetectors, quantum dots, thermoreflectance, electroreflectance and solar cells. Due to its tremendous commercial value, a complete description of its electronic structure is essential. While ground state density functional theory (DFT) calculations based on the pseudopotential method is able to give accurate band gaps for group IV and III-V semiconductor materials , the ab-initio description of II-VI compounds is more complex than IV/III-V semiconductors due to *sp*-*d* orbital interaction. In this work, we firstly compared our ground state and excited state band structure with previous results. We then proceed to obtain the spectral function and momentum distributions. With the momentum distributions, we then proceed to obtain the Compton profile. We discuss our calculations on these systems in detail in Section 4.3 of Chapter 4.

CHAPTER 2 : COMPTON PROFILES FROM FIRST PRINCIPLES : THEORETICAL BACKGROUND

In this chapter, we will discuss in detail the theories and models used to describe the Compton profile from first principles methods. We start with Section 2.1 which provides an overview of Compton scattering (Section 2.1.1 and Section 2.1.2) and its relation to momentum density (Section 2.1.3). We then discuss how the momentum density is obtained from DFT (Section 2.1.4) and discuss how it is influenced by the Marzari-Vanderbilt cold smearing (Section 2.1.5). Section 2.2 discusses how the Compton profile is obtained beyond the impulse approximation (Section 2.2.1) as discussed in Section 2.1. These methods are constructed from the Green's function (Section 2.2.2) to obtain Hedin's GW Approximation (Section 2.2.3). With the energies from the GW Approximation, we can obtain the spectral functions which will be used to construct the momentum density (Section 2.2.4). Now that we are able to construct the momentum density from both the ground state DFT and the excited state GW Approximation, we are able to construct their respective Compton profiles. We discuss methods to compare these two profiles in Section 2.3. We firstly discuss the Lam Platzman correction (Section 2.3.1) which allows us to directly compare the two methods via the Kubo's correlation correction (Section 2.3.2) which is similar to studying the difference profile in comparison with experimental Compton profiles. We finally discuss the anisotropy in Section 2.3.3. We end this chapter with a discussion on previous studies to obtain the Compton profile via the GW Approximation.

2.1 Compton Scattering : Physics and First-Principles Calculations

In this section, we will firstly define the kinematics of the inelastic scattering process. We show how the first and second order non-relativistic double differential scattering cross section (DDSCS) for charge scattering can be obtained in terms of the

Thomson cross section and the dynamic structure factor by expanding a semiempirical interaction Hamiltonian using Lehman's representation and standard second quantization tools. We will then layout the Compton regime based on impulse approximation which yields the fundamental relation between the DDSCS and momentum distribution of scattering electrons and finally describe the implementation of the impulse approximation in condensed systems. The formalisms and discussions used in these sections are presented in (Cooper et al.,2004; Cooper, 1985) and we have explicitly defined the derivation steps from that work.

2.1.1 DDSCS and Kinematics

A typical inelastic scattering experiment consists of first producing a well collimated beam of monochromatic photons, select a solid angle element $d\Omega$ of scattered beam and analyze the energy of this angle with a resolution $d\omega$. We layout the kinematics behind this Compton scattering experiment and outline the DDSCS in terms of a semi-empirical interaction Hamiltonian.

In Figure 1.1 we show the schematics of a Compton scattering experiment. A photon of energy $\hbar\omega_1$, wave vector k_1 and polarization vector ε_1 impinges on target I with initial energy E_I then scatters as a photon of energy $\hbar\omega_2$, wave vector k_2 and polarization vector ε_2 leaving the target as state F and final energy E_F. The energy

$$\hbar(\omega_1 - \omega_2) \tag{2.1}$$

and momentum

$$\hbar(k_1 - k_2) \tag{2.2}$$

are transferred to the target. As a result, the energy of the target due to energy conservation is

$$\hbar\omega = E_F - E_I \tag{2.3}$$

The modulus of transferred momentum is given by

$$q = \left(\omega_1^2 + \omega_2^2 - 2\omega_1\omega_2\cos\phi\right)^{1/2}/c \tag{2.4}$$

if

$$\omega \ll \omega_1 \tag{2.5}$$

$$q \approx 2k_1\sin(\phi/2) \tag{2.6}$$

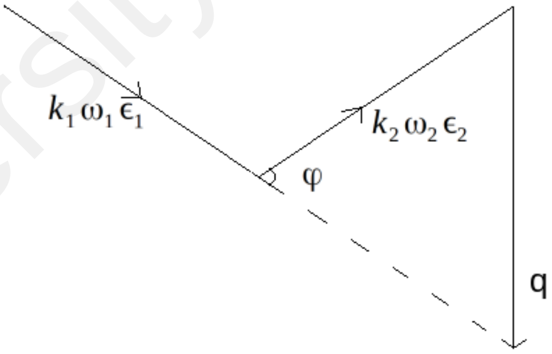

Figure 2.1: Compton scattering schematics.

Within the limits of a non-relativistic lowest order perturbation theory and neglecting resonance phenomena, the DDSCS which is a function of q and ω can be defined qualitatively as

$$\frac{d^2\sigma}{d\Omega\, d\omega^2} = \left(\frac{d\sigma}{d\Omega}\right)_{Th} S(q,\omega) \tag{2.7}$$

where

$$\left(\frac{d\sigma}{d\Omega}\right)_{Th} \tag{2.8}$$

is the Thomson cross section and

$$S(q,\omega) \tag{2.9}$$

is the dynamic structure factor. The dynamic structure factor reflects the properties of the target in absence of a perturbing probe (Platzman, 1974). The Thomson cross section is the coupling to an electromagnetic (EM) field which is treated to the lowest order Born approximation (Hawkes et al., 1980). The DDSCS will allow us to learn about the dynamic properties of matter from this inelastic scattering experiment and is a measure of probability (Olevano et al., 2012). We will show later that this term can be derived from the correlation function of an electron system undergoing scattering (Kubo, 1996).

The non-relativistic DDSCS for charge scattering is defined by the Klein-Nishina cross-section for scattering from a single free electron at rest (Carlson et al., 1982). It is derived from a complete second order relativistic scattering cross section. The problem with the relativistic total cross section is the mixed properties of probe with target. A non-relativistic DDSCS handles the coupling of the EM field to the scattering electron system. This is defined by a semiempirical interaction Hamiltonian

$$H_{int}=\sum_{j}(e^2/2mc^2)A(r_j)^2-\sum_{j}(e/mc)A(r_j)p_j \tag{2.10}$$

where p_j is the momentum operator. $A(r_j)$ is the vector potential operator of the EM field which expresses the photon creation and annihilation operators given by

$$A_j = \sum_l \{ a_l A_l(r_j) + a_l^* A_l^\dagger(r_j) \} \tag{2.11}$$

where

$$A_l(r_j) = V^{-1}/2\left(4\pi c^2\right)^{½} \hat{\epsilon}_l e^{(ik_l . r_j)} \tag{2.12}$$

The DDSCS can be obtained by expanding H_{int} using the Lehmann's representation (Mattuck, 2012) and the standard second quantization tools to finally obtain

$$\begin{array}{l} \dfrac{d^2\sigma}{d\sigma d\omega_2} \\ = \dfrac{\omega_2}{\omega_1} r_o^2 \sum_F \left| \begin{array}{c} \langle F | \sum_j \exp(iq . r_j) | I \rangle (\hat{\epsilon}_1 \hat{\epsilon}_2) \\ - \dfrac{1}{m} \sum_N \dfrac{\langle F | \hat{\epsilon}_2^* \sum_j p_j \exp(-i k_2 r_j) | N \rangle \langle N | \hat{\epsilon}_1 \sum_j p_j \exp(i k_1 r_j) | I \rangle}{E_N - E_I - \hbar\omega_1 + i\Gamma_N/2} \\ \dfrac{- \langle F | \hat{\epsilon}_1 \sum_j p_j \exp(i k_1 r_j) | N \rangle \langle N | \hat{\epsilon}_2^* \sum_j p_j \exp(-i k_2 r_j) | I \rangle}{E_N - E_I - \hbar\omega_2} \end{array} \right|^2 \\ \qquad\qquad\qquad * \delta(E_f - E_i - \hbar\omega) \end{array} \tag{2.13}$$

Thus, for a non-resonant case, the dynamic structure factor is given by

$$S(q, \omega) = \sum_F |\langle F | \sum_j \exp(iq . r_j) | I \rangle|^2 \delta(E_F - E_I - \hbar\omega) \tag{2.14}$$

with the Thomson scattering cross section given by

$$\left(\frac{d\sigma}{d\Omega}\right)_{Th}=r_o^2(\hat{\epsilon}_1\,.\,\hat{\epsilon}_2^*)^2\left(\frac{\omega_2}{\omega_1}\right) \tag{2.15}$$

In this formalism, the dynamic structure factor gives information on the dynamic behavior of scattering electron systems in terms of excitation from initial to final states. The delta function represents a combined density of initial and final states.

The integral representation of the delta function reveals better information about the correlated motion of the scattering particles in the dynamic structure factor. It is given by

$$S(q\,,\omega)=(1/2\pi\hbar)\int_{-\infty}^{\infty} dt\, e^{-i\omega t}\sum_F \langle I|\sum_j e^{-iq\,.\,r_j}|F\rangle\langle F|e^{iHt/\hbar}\sum_j e^{iq.\,r_j}e^{-iHt/\hbar}|I\rangle \tag{2.16}$$

The response of the system strongly depends on how $2\pi/q$ compares with the characteristic length l_c and how ω compares with characteristic frequencies ω_c . If $ql_c < 2\pi$ and $\omega\approx\omega_c$, the interference between waves scattered from many particles at different times is of importance. It is used to probe collective behavior of many particle systems. If $ql_c > 2\pi$ and $\omega>\omega_c$, the waves scattered from different particles do not interfere, probing one particle at a time. In this range, the timescale of the probe is small enough to prevent the system from rearranging itself. This is the impulse approximation of the Compton scattering regime.

2.1.2 The Compton Scattering Regime and Impulse Approximation

The Compton scattering regime describes the inelastic scattering regime with high momentum and energy transfer. In the high momentum transfer region (i.e large enough to treat ejected electrons as a free noninteracting particle (Soininen et al., 2001) due to slow electron probes (Huotari et al., 2007)), interference effects between waves scattered from different particles at different times are neglected. Thus, we are observing single particle properties specifically the same particle at different times. These time intervals are so short that the system does not undergo rearrangement during scattering. This requires an energy transfer greater than characteristic energies of the scattering system. For information on momentum density of valence electrons the energy transfer need not be as large as core electron information.

In the impulse approximation, the DDSCS follows the assumption that energy and momentum transfer is valid only for the Compton scattering regime. Starting from the Hamilton operator

$$H = H_o + V \qquad (2.17)$$

We expand from Equation 2.9 the term

$$e^{iHt} = e^{iH_O t} e^{iVt} e^{-[H_o,V]t^2/2\hbar^2} \qquad (2.18)$$

As mentioned above, if the energy and momentum transferred from the probe is larger than the binding energy of the sample , the impulse approximation is valid and the measured spectra takes into account core and valence electron binding energy (Huotari et al., 2010). In analytical terms,

$$\hbar\omega \gg \left(\langle [H_o, V] \rangle\right)^{1/2} \qquad (2.19)$$

which gives

$$e^{-i[H_o,V]t^2/2\hbar^2} \approx 1 \qquad (2.20)$$

This is valid if the transferred energy is larger compared with the characteristic energies of the system. We then insert Equations 2.18 and 2.20 to 2.16 to obtain

$$\frac{d^2\sigma}{d\Omega\, d\omega^2}=\left(\frac{d\sigma}{d\Omega}\right)_{Th}\left(\frac{1}{2\pi\hbar}\right)\int dt\, e^{-i\omega t}\langle I|e^{-iq.r}\, e^{i(H_o+V)t/\hbar}e^{iq.r}e^{-i(H_o+V)t/\hbar}|I\rangle \tag{2.21}$$

Since r commutes with V,

$$\vec{r}\,V-V\,\vec{r}=0 \tag{2.22}$$

We obtain

$$=\left(\frac{d\sigma}{d\Omega}\right)_{Th}\left(\frac{1}{2\pi\hbar}\right)\int dt\, e^{-i\omega t}\langle I|e^{-iq.r}\, e^{i(H_o)t/\hbar}e^{iq.r}e^{-i(H_o)t/\hbar}|I\rangle \tag{2.23}$$

Since the kinetic energy operator corresponds to a complete set of eigenfunctions p_F , we can write Equation 2.23 as

$$\frac{d^2\omega}{d\Omega\, d\omega^2}=\left(\frac{d\sigma}{d\Omega}\right)_{Th}\left(\frac{1}{2\pi\hbar}\right)\int dt\, e^{-i\omega t}\langle I|e^{-iq.r}e^{iq.r}|p_F\rangle e^{-i\epsilon t/\hbar}e^{i\epsilon t/\hbar} \tag{2.24}$$

Placing in the delta-function

$$=\left(\frac{d\sigma}{d\Omega}\right)_{Th}\left(\frac{1}{2\pi\hbar}\right)\int dt|\langle I|e^{-iq.r}|p_F\rangle|^2\,\delta(\epsilon(p_F)-\epsilon(p_F-\hbar q)-\hbar\omega) \tag{2.25}$$

From the kinetic energy operators

$$\epsilon(p_F)=\epsilon(p+\hbar q)=(p^2+2\hbar\, p.q+\hbar q^2)/2m \tag{2.26}$$

Thus,

$$\frac{d^2\sigma}{d\Omega d\omega^2}=\left(\frac{d\sigma}{d\Omega}\right)_{Th}\left(\frac{1}{2\pi\hbar}\right)\int|\langle I|p\rangle|^2\delta\left(\hbar^2q^2/2m+\hbar p.q/m-\hbar\omega\right)dp \tag{2.27}$$

The momentum space wave function is the Fourier transform of the position space wave function

$$\begin{aligned}\rho(p)&=(1/2\pi\hbar)^3|\langle I|p\rangle|^2=|\chi(p)|^2\\&=(1/2\pi\hbar)^3|\int\psi(r)e^{-(ip.r/\hbar)}dr|^2\end{aligned} \tag{2.28}$$

It gives the probability of finding the initial electron with momentum p.

If the delta function in Equation 2.27 is true

$$\hbar^2q^2/2m+\hbar p.q/m-\hbar\omega=0 \tag{2.29}$$

We obtain,

$$p.q=\frac{\omega m}{q}-\frac{\hbar q}{2}=\frac{m}{q}\left(\omega-\frac{\hbar q^2}{2m}\right) \tag{2.30}$$

where

$$q=\left(\omega_1^2+\omega_2^2-2\omega_1\omega_2\cos\phi\right)^{½}/c \tag{2.31}$$

Thus

$$=\frac{mc\{\omega-\frac{\hbar(\omega_1^2+\omega_2^2-2\omega_1\omega_2\cos\phi)}{2mc^2}\}}{(\omega_1^2+\omega_2^2-2\omega_1\omega_2\cos\phi)^{1/2}} \tag{2.32}$$

Multiply by $\frac{\hbar}{\hbar}$

$$=\frac{mc\{\hbar\omega_1-\hbar\omega_2-\frac{\hbar^2}{2mc^2}(\omega_1^2+\omega_2^2-2\omega_1\omega_2\cos\phi)\}}{(\hbar^2\omega_1^2+\hbar^2\omega_2^2-2\hbar^2\omega^1\omega^2\cos\phi)^{1/2}} \tag{2.33}$$

Add

$$-2\omega_1\omega_2+2\omega_1\omega_2 \tag{2.34}$$

to the third term

$$=\frac{mc\{\hbar\omega_1-\hbar\omega_2-\frac{\hbar^2}{2mc^2}(\omega_1^2+\omega_2^2-2\omega_1\omega_2+2\omega_1\omega_2-2\omega_1\omega_2\cos\phi)\}}{(\hbar^2\omega_1^2+\hbar^2\omega_2^2-2\hbar^2\omega^1\omega^2\cos\phi)^{1/2}} \tag{2.35}$$

Omitting

$$\frac{\hbar^2(\omega_1-\omega_2)^2}{2mc^2} \tag{2.36}$$

$$=\frac{mc\{\hbar\omega_1-\hbar\omega_2-\frac{\hbar^2}{2mc^2}(1-\cos\phi)\}}{(\hbar^2\omega_1^2+\hbar^2\omega_2^2-2\hbar^2\omega^1\omega^2\cos\phi)^{1/2}} \tag{2.37}$$

Thus, Equation 2.25 can be simplified to

$$\begin{aligned}\frac{d^2\sigma}{d\Omega\, d\omega^2}&=\left(\frac{d\sigma}{d\Omega}\right)_{Th}(m/\hbar q)\int\int\rho(p_x,p_y,p_z=p_q)\,dp_x\,dp_y\\&=\left(\frac{d\sigma}{d\Omega}\right)_{Th}(m/\hbar q)\,J(p_q)\end{aligned}\tag{2.38}$$

where

$$J(p_q)=\int\int\rho(p_x,p_y,p_z)\,dp_x\,dp_y\tag{2.39}$$

is the directional Compton profile.

The essence of impulse approximation thus consists of replacing the initial and final state energies in the argument of the delta-function by the kinetic energy because the potential, V commutes with r. This assumes the electron to be free with momentum p_F in its final state and the momentum is conserved. However, the bonding of the electron to the scattered atom , V is not completely neglected and can be accounted for via $\rho(p)$. If we define the system as single-particle wavefunction $≣_i(r_j)$, each scattering process will involve only one-particle of the system.

We have thus observed that under the impulse approximation, the Compton profile is the projection of electron momentum density which can be deduced by the DDSCS (Sternemann et al., 2000). This cross section of inelastic x-ray scattering at high momentum transfer limit is related to the electronic ground state wave function and is the key observation in the study of Fermiology. In Section 2.2, we will show that it is possible to observe quasiparticle peaks, satellite structure, discontinuity and renormalization factor from the momentum density which can be used to obtain insight on electron-electron correlation around the Fermi surface break. To study these ground state correlation effects, the momentum space resolution must be maximized while the final state effects must be minimized (Huotari et al., 2007). In this work, Huotari investigated the effects of not obeying the impulse approximation by studying the broadening of the experimental spectra to obtain the Fermi surface. It outlines the experimental motivations behind using the GWA to study the Fermi surface via Compton profile.They found that the Compton profile peak height has been found to be lower than theoretically predicted and this is said to be due to correlation effects. The features from the Fermi surface from experiment is observed to be broader compared to LDA+GWA calculations. This could be accounted for by using the antisymmetrized germinal product.

The impulse approximation however breaks down for tightly bound core electrons where even at high momentum and energy transfers, the binding energy of the excited core electron to its core neighbors will be too strong to neglect (Soininen et al., 2001). Besides core electrons, final state electrons are also an indication that the impulse approximation is not obeyed (Sternemann et al., 2000). Improvement on scattering intensity of the Compton scattering experiment allows a comparison of the Compton profile which is closer to the model which assumes impulse approximation. In an earlier work, Platzman (1970) observed that a 10 keV probe can explain ground state electron behavior within the impulse approximation. In a later study, it is observed that applying x-ray energies between 16-18 keV shows that a small increase in probing X-ray energies reduces the influence of the spectral functions significantly (Huotari et al., 2007). They observed that even if an intense probing energy of ~10 keV was applied, there is still broadening in the spectral function compared to the Fermi energy of 14.3 eV. This is also seen in probes with a momentum resolution of 0.02 a.u (Soininen et al., 2001). They conclude that the lifetime width of the spectral function reacts slowly compared to the change of the momentum and energy transfer of the probing energies. However, (Soininen et al., 2001) observed that at 30 keV, final state effects are negligible.

EELS, LEED, XAS etc. also demand detailed knowledge of electron scattering, inelastic mean free path (IMFP) and dielectric response of medium probed. Bourke (Bourke et al., 2012) introduced a causally constrained momentum dependent broadening theory providing electronic/optical resonances in better agreement with optical attenuation and electron scattering data. Specifically, they developed a theory to calculate the electron IMFP in the low energy region (< 100 eV). With their model, they could probe effects of a free electrons material with a single dominant resonance peak or complex electron system with many optical resonances. Existing models of dielectric response systematically overestimate IMFP due to poor account of lifetime broadening or exchange correlation effects.

They begin with the optical data model used by Tanuma (Woicik et al., 2016). It deals with the determination of electron loss function related to IMFP,

$$\lambda(E)^{-1}=\frac{\hbar}{a_o\,\pi E}\int_{0}^{\frac{(E-E_F)}{\hbar}}\int_{q}^{q_t} Im\,\frac{-1}{\epsilon(q\,,\omega)}\,dq\,d\,\omega \tag{2.40}$$

The electron loss function is represented as susceptibility to plasmon excitation of a given energy and momentum. It is defined as the relative probability of an excitation of energy and momenta propagating in a medium. λ is thus obtained from the momentum dependent dielectric function. The complex dielectric function is a fundamental material parameter determining optical and electronic scattering behavior of the medium. λ is however obtainable only for the case of the free electron gas. Thus, its resonance behavior can be described by the Lindhard theory for lossless free electron gas or Mermin theory which accounts for lifetime broadening.

The optical data model is given by the momentum dependent electron loss function of a solid which is constructed by summing the free electron gas type resonances matching optical behavior of materials.

$$Im[-\frac{1}{\epsilon_{data}}]=\sum of\ I\ A_I\ Im\frac{-1}{\epsilon_{FEG}(0,\omega;\omega_p=\omega_i)} \tag{2.41}$$

Thus the free electron gas optical loss function is obtain from the single resonance peak at optical limit of the plasmon frequency ω_p. Lindhard type functions model resonance described by delta functions. This is unphysical due to lack of lifetime broadening. The Drude/Mermin approach includes an additional lifetime broadening for each plasmon/scattering resonance. This implies that Drude/Mermin approaches are many pole models. Authors have shown that low and medium energy ELFs and IMFPs are not consistent and have not converged to a unique result. It does not preserve the local electron number in the electron loss function which disagrees with Kramers-Kronig sum rule. Bourke (Bourke et al., 2015) later introduced an alternative description of the Lindhard equation which preserves the sum rule.

2.1.3 Momentum Density

Fundamentally important to solid state physics is the shape of the momentum density near the Fermi surface. The momentum density is defined as the probability to observe electron with momentum, p (Huotari et al., 2010). As shown in Equation (2.39), assuming the impulse approximation, the Compton profile gives a two component average of the 3-d momentum density taking intrinsic inhomogeneities and Coulomb correlation into account (Lam et al., 1974). These profiles are thus built up from slices through the Fermi surface of radius, p_F in momentum space. In the case of the ideal Fermi gas of free noninteracting electrons, the momentum density is given by the Fermi-Dirac distribution. At equilibrium at zero temperature, a step function with a discontinuity of slope 1 at the Fermi surface sphere is observed and is attributed to collisions between electrons. This is reflected experimentally where the Compton profile will have a discontinuity in the first derivative of the Fermi break (Huotari et al., 2010). This derivative discontinuity of the Compton profile is an unambiguous quantification of the level of correlation (Olevano et al., 2012).

Broadened excitation spectra and smoothened discontinuity of the momentum density at the Fermi break causes anomalously large smearing of the Compton profile. It can be explained as an incomplete incorporation of electron-electron correlation effects in momentum density (Soininen et al., 2001). This refers to the case of the Fermi liquid where the momentum density departs from the step function and a spill out of density from lowest to highest momenta is observed. This make the momentum density which is expected to follow a step function due to a non-interacting system be a continuous function. In a normal Fermi liquid, if excitations are dampened, broadening vanishes and a delta peak is obtained (Olevano et al., 2012). An example would be the interaction of scattering electron and the rest of an electron gas causing further broadening of measured Compton profiles (Huotari et al., 2010). In this situation, the probability to observe an electron above the Fermi momenta is finite above the zero temperature. Thus, measuring momentum density can provide direct evidence of Fermi liquid behavior. Specifically, one can obtain information on the shape of the Fermi surface and thus study short range electron-electron and electron ion collision which can be accounted for by correlation and the jump magnitude. These terms represent a direct measure of strength of quasiparticle excitations at the Fermi surface (Olevano et al., 2012). Furthermore, experimental observation of the momentum density allows to compare accuracy of approximate many body wave functions.

In previous studies of momentum density smearing, (Huotari et al., 2007), Huotari studied the impact of the impulse approximation to experimental data. Experiment shows the obtained Fermi surface to be sharp, however the theoretical spectra is broadened. This can be attributed to correlation effects. Peter (Peter et al., 1993), has pointed out that the solution to the two particle momentum density restores cyllindrical symmetry unavailable to the solution of a Hamiltonian in Landau gauge. This allows comparison to spread in angle of annihilation radiation which is wide enough that different n-states under the Fermi sphere or Fermi cylinder are smeared. This smearing is determined by a perturbing potential which gives a break of angular width instead of the sharp Fermi break. Barnes (Barnes et al., 1991) has also mentioned that spinon and holon effects change superconduction ordering which smears out a sharp Fermi surface in the state. In this work, we have adopted the quasiparticle description for interacting fermions *D*>1. At *D*=1, it is non-analytic at mass shell. This is reflected in the perturbation theory the spectral function. This can be solved by the Tomonaga-Luttinger liquid model which rewrites the fermionic fields in terms of bosonic fields (Imambekov et al., 2012). In this case, the dispersion curvature of the structure factor in a Luttinger liquid is treated as a perturbation. For free fermions, the peak is narrow and non-analytical at the curvature. We can thus write the Hamiltonian for the linear Luttinger liquid as

$$H=H_{kin}+H_{int}=A[(\delta_x\,\psi_{[L]})^2+(\delta_x\,\psi_{[L]})^2]+B\,\delta_x\,\psi_L\,\delta_x\,\psi_R \tag{2.42}$$

where

$$A=V_{LL}+\frac{V_F}{2}\quad\text{or}\quad V_{RR}+\frac{V_F}{2}\quad\text{and}\quad B=2V_{LR} \tag{2.43}$$

Diagonalization would give

$$\begin{aligned}H&=V/2[(\delta_x\,\psi_{[L]})^2+(\delta_x\,\psi_{[L]})^2]\\&=\exp(-1/2\,\alpha_R^2\langle(\psi_R(x,t)-\psi_R(0,0))\,\psi_R(0,0)\rangle_H)\end{aligned} \tag{2.44}$$

where the correlation function can be simplified to

$$\langle(\psi_R(x,t)-\psi_R(0,0))\,\psi_R(0,0)\rangle=\ln[(x_0 vt)/x_o] \tag{2.45}$$

For non-linear Luttinger liquids, the excitation energies at any given momentum are finite. This results in low energy dynamics at an arbitrary momentum which allows power law threshold singularities in the response functions. This allows us to write the mapping on free chiral fermions as

$$H_o=\frac{V}{2\pi}\int dx\,((\Delta\,\psi_L)^2+(\Delta\,\psi_R)^2) \tag{2.46}$$

$$H_d=dx\,d^{\dagger}(x)(\epsilon(k)-I\,v_d\frac{\delta}{\delta_x}) \tag{2.47}$$

$$H_{int}=\int dx(V_L\Delta\frac{\psi_L}{2\pi}-V_R\Delta\frac{\psi_R}{2\pi})d(x)d^{\dagger}(x) \tag{2.48}$$

where H_o describes free chiral (L,R) fermions, H_d describes the impurity and H_{int} the forward scattering of L and R fermions off impurity. This allows us to write the spectral function in terms of

$$A(k,\omega)=\Theta(\epsilon(k)-\omega)\left|\frac{1}{\epsilon(k)-\omega}\right|^{1-\frac{(\delta_{(k)})^2}{2\pi}-(\frac{\delta_{(k)}}{2\pi})^2} \tag{2.49}$$

where

$$\frac{\delta_{\pm¿}(k)}{2\pi}=\frac{(1/\sqrt{(k)}(\frac{k}{m}-\frac{\delta\epsilon(k)}{\delta(k)})\pm\sqrt{(k)}(1/\pi\frac{\delta\epsilon(k)}{\delta(p)}+\frac{v}{k}))}{2(\pm\frac{\delta\epsilon(k)}{\delta k}-v)}¿ \tag{2.50}$$

Setting k=±k_F will thus resort to broadened mass shell states, holons or spectral edge states, spinons. Barbiellini (Barbiellini, 2000) obtained the occupation numbers from natural orbital eigenvalues of single Kohn-Sham energy bands. This eigenvalue contains the pairing term which is obtained by the Kohn-Sham exchange integral. The pairing term is constructed from a two particle spin singlet function called a generating geminal with coefficients obtained from a Cooper-pair like function. With this construct a correlation effect is introduced and can be adjusted to produce a smearing in momentum space of 0.07 a.u. Recently, Aguiar (Aguiar et al., 2015) confirmed the importance of the pairing correlations by showing that the reason fitting parameters of the momentum density obtained from a semi-empirical approach for Li, B and C differs from its other column members in the periodic table is due to the existence of significant pairing correlations in the ground state identified in terms of electron transfers from *s* to *p* like character. Besides many body effects, quantum confinement effects also smear the momentum density. This is seen in (Saniz et al., 2002) study of Compton scattering and positron annihilation of a simple quantum dot model. They observe that the momentum density tends to a homogeneous electron gas step function as dot radii increases but has increased structure at small radii. At low electron densities, the atomic-like form of wavefunction becomes evident and at higher electron densities the dot Fermi momenta is represented by the homogeneous electron gas value. Compton scattering is also useful for studying spin systems where metals with highly isotropic momentum density are most suited for study via Compton scattering. The momentum density is a quantity showing direct evidence of the Pauli principle (Olevano et al., 2012). If we know the momentum density per spin state, we can observe a basic many body observable dependent on the Pauli principle (Huotari et al., 2010).

2.1.4 Electron-Electron Interaction

The momentum density is a term which can be obtained from first principles calculations. In this work, we have employed the DFT (Hohenberg et al., 1964; Kohn et al., 1965) and DFT based calculations to obtain the momentum density. In this section we outline the formalism behind DFT which is able to predict the total energy of a system of electrons and nuclei. Hamiltonians constructed to calculate the total energy of a one atom system can be used to model real atomic systems while more complicated systems are linearly combined extensions of atomic Hamiltonians. With the total energy or differences between total energies one can obtain the equilibrium lattice constant of a crystal, surface and defect states, bulk moduli, phonon states, piezoelectric constants and phase transition pressures and temperatures. The formalism and discussions for this section are obtained from the review paper by Payne (Payne et al., 1992).

According to the Born-Oppenheimer approximation (Sholl et al., 2011), due to large differences in mass between electrons and nuclei, electrons respond instantaneously to the motion of nuclei. Thus, nuclear coordinates are treated separately from electron coordinates in the many body wave function. Based on the Born-Oppenheimer approximation comes DFT which can be used to model electron-electron interaction. It allows to map exactly a strongly interacting electron gas onto a single particle moving in an effective nonlocal potential.

It is a nontrivial problem in electronic structure calculations to account for effects of electron-electron interaction specifically exchange and correlation between electrons. The exchange term originates from the antisymmetry of the electron wavefunction. It produces a spatial separation of the same spin electron which reduces Coulombic energy. This reduction of energy is referred to as exchange energy (Jones et al., 1989). The correlation energy is defined as the difference between the many body energy of an electronic system and its energy via the Hartree-Fock approximation (Payne et al., 1992). DFT is a widely used method for calculating ground state properties and electronic structure of solids. It is a simple method to describe the effects of exchange and correlation in an electron gas. It is built upon the Hohenberg-Kohn theorem and the Kohn-Sham (KS) equation. The Hohenberg-Kohn theorem states that the total energy of an electron gas is a unique functional of an electron density. The minimum value of this total energy functional is the ground state energy of the system and its electron density is the exact single particle momentum density. In practice, this can be done by replacing the many electron problem with an exactly equivalent set of self-consistent one-electron equations. Starting from the Kohn-Sham equation,

$$\left[\frac{-\hbar^2}{2m}+V_{ion}(r)+V_H(r)+V_{xc}(r)\right]\psi_i(r)=E_i\psi_i(r) \tag{2.51}$$

where the Hartree potential, $V_H(r)$and the exchange correlation potential, $V_{XC}(r)$ is given by

$$V_H(r)=e^2\int\frac{n(r')}{|r-r'|}d^3r' \quad \text{and} \quad V_{xc}(r)=\frac{\delta E_{xc}[n(r)]}{\delta n(r)} \tag{2.52}$$

The KS equation gives a self-consistent solution as wave functions which minimize the Kohn-Sham total energy functional. It represents a mapping of interacting many electron systems onto noninteracting electrons moving in an effective potential due to other electrons. The total energy functional is given by

$$\begin{aligned}E[\psi_i]=2\sum_i\int\psi_i-\frac{\hbar^2}{2m}\nabla^2\psi_i d^3r+\int V_{ion}(r)n(r)d^3r\\+\frac{e^2}{2}\int\frac{n(r)n(r')}{|r-r'|}d\vec{r}\,d\vec{r}\,'+E_{xc}[n(r)]+E_{ion}(R_I)\end{aligned} \tag{2.53}$$

where $V_{ion}(r)$ is the static electron-ion potential, $E_{XC}[n(r)]$ are the exchange correlation functional and $E_{ion}(R_I)$ is the Coulomb energy between the nuclei. The simplest method to describe the exchange correlation energy is the localized density approximation (LDA) (Kohn et al., 1965). It describes the exchange correlation energy per electron in a homogeneous electron gas which has the same density as the electron gas at point r. It is given by

$$E_{xc}[n(r)] = \int \epsilon_{xc}(r) n(r) d^3 r \tag{2.54}$$

where $\varepsilon_{XC}(r)$ is the exchange correlation energy at point r in the electron gas. The LDA ignores correction to $E_{XC}(r)$ due to inhomogeneities in the electron density.

As stated previously, only the minimum of the Kohn-Sham energy functional has physical meaning. This energy is equal to the ground state energy of a system with electrons of ions at positions R_I. The KS equations are solved self-consistently. We can then obtain the occupied electronic states, the charge density and the electronic potential. The highest occupied eigenvalue in an atomic/molecular calculation is equal to the unreleased ionization energy of the system. The wavefunctions used are solutions of one-electron Schrodinger equation which includes exchange and correlation in the form of local potential. The solution to the KS equation is not a one-particle wave function. It cannot be used to simply calculate momentum density, only ground state position electron density.

2.1.5 Finite Temperature DFT

The electron density can be deduced from a ground state calculation while the momentum density is obtained from

$$n(p)=\sum_{i=1}^{n} n_i |\psi_i(p)|^2 \tag{2.55}$$

which is the Fourier transform of real-space one electron wavefunction, Ψ_i and occupation number, n_i . For our work, the occupation number density is written in terms of an entropy function which results in a smeared occupation number density. This description is based on the finite temperature DFT technique of Marzari-Vanderbilt which we elaborate on in this section. We point out that we follow the interpretation of Luttinger and Schulke who have stated that the momentum distribution function is defined as the mean occupation number of the state k (Luttinger, 1960; Schulke et al., 1996).

Marzari (Marzari, 1996; Marzari et al., 1997; Marzari et al., 1999) introduced a reformulation of finite temperature electronic structure. They define an invariant free energy functional with respect to unitary transformation which allows a projected functional which is dependent only on orbitals where its one particle statistical operator commutes with the non-self consistent Hamiltonian. The subsequent minimization to self-consistency of the functional does not depend on occupations and rotations of orthonormal orbitals and requires doubly preconditioned all-band conjugate gradient methods. Each iteration will ensure that the statistical operator commutes with the current orbital representation of the Hamiltonian.

Finite temperature DFT requires an ad-hoc procedure for updating the orbitals in the occupied subspace. The evolution of occupancies is driven by rescaled diagonal elements of the Hamiltonian. It is expressed in terms of statistical mechanics based operators and traces. The Helmholtz free energy functional

$$A[\Gamma_N]=tr\,\Gamma_N\left(\frac{1}{\beta}\ln\Gamma_N+\hat{H}\right) \tag{2.56}$$

where Γ_N is the many body operator, is rewritten as

$$A[T;\{\psi_i\};\{f_i\}] = \sum_{ij} f_{ji} \langle \psi_i | \hat{T}_l + \hat{V}_{nl} | \psi_j \rangle + E_{xc}[n] - TS[f_{ij}] \tag{2.57}$$

The wavefunction should be normalized and orthogonal while the trace *f* should be equal to *N* number of electrons. With this functional, one can obtain a rotation invariant projected functional

$$G[T;\{\psi_i\}] = min\, A[T;\{\psi_i\};\{f_i\}] \tag{2.58}$$

The functional *G* is brought to self-consistency with a minimization with respect to the wavefunctions. After each iteration, the f_{ij} are updated to minimize *A*. Using the notation

$$h_{ij} = \langle \psi_i | \hat{T}_l + \hat{V}_{nl} | \psi_j \rangle \quad \text{and} \quad V_{ij}^n = \langle \psi_i | V_{xc}^n | \psi_i \rangle \tag{2.59}$$

we can write the minimum conditions for *A* as

$$\begin{aligned} \frac{\delta A}{\delta f_{ji}} &= h_{ij} + \frac{\delta E_{xc}}{\delta f_{ji}} - T\frac{\delta S}{\delta f_{ji}} - \mu\,\delta_{ij} \\ &= h_{ij} + V_{ij}^n - T[S'(f)]_{ij} - \mu\,\delta_{ij} = 0 \end{aligned} \tag{2.60}$$

The third term contains the Fermi-Dirac entropy derivative written in terms of occupation numbers calculated by diagonalizing *f*. The fourth term is the Lagrange multiplier. With this term, one can obtain the smearing technique for the density of states which is dependent on the entropic term in the total energy functional.

The deterioration of sampling accuracy in calculating the total charge density, kinetic and nonlocal terms in the total energy functional is directly related to the presence of discontinuity in functions to be integrated. This is a characteristic of the electron gas at zero temperature where the occupation numbers drop to zero when the band energy is above the Fermi surface. Electrons of this system will be distributed according to the Fermi-Dirac distribution which will have a smoother discontinuity as the electronic temperature or precision of sampling mesh increases. By generalizing beyond the Fermi-Dirac distribution, entropy is expressed as a function of energy instead of occupation numbers. Thus, we describe an unsmeared density of state as

$$n(\epsilon)=\sum_{ik}\delta(\epsilon-\epsilon_{ik}) \qquad (2.61)$$

which will be used to obtain a smeared density of state via convolution with $\tilde{\delta}$

$$\tilde{n}(\epsilon)=\int_{-\infty}^{\infty} d\epsilon'\frac{1}{\sigma}\tilde{\delta}\left(\frac{\epsilon-\epsilon'}{\sigma}\right)n(\epsilon') \qquad (2.62)$$

The smeared DOS is used to obtain the smeared band energy

$$\tilde{E}_{band}=\int_{-\infty}^{\mu} d\epsilon\,\hat{n}(\epsilon) \qquad (2.63)$$

Here, the smeared total energy functional is equivalent to the generalized free energy whose form depends on the choice of broadening. With some algebra, we can rewrite the band energy into two terms

$$\tilde{E}_{band}=\int_{-\infty}^{\infty} d\epsilon'\epsilon' n(\epsilon')\int_{-\infty}^{\frac{\mu-\epsilon'}{\sigma}} dx\,\tilde{\delta}(x)+\sigma\int_{-\infty}^{\infty} d\epsilon' n(\epsilon')\int_{-\infty}^{\frac{\mu-\epsilon'}{\sigma}} dx\,x\,\tilde{\delta}(x) \qquad (2.64)$$

We can rewrite this equation in terms of the occupation function and entropy function for first and second term respectively

$$\widetilde{E_{band}}=\sum_{ik}\epsilon_{ik} f\left(\frac{\mu-\epsilon_{ik}}{\sigma}\right)-\sigma\sum_{ik} S(\mu-\epsilon_{ik}) \tag{2.65}$$

Assuming an unsmeared DOS expanded in powers of ε

$$n(\epsilon')=\frac{1}{k!}\sum_{k=0}^{\infty}\frac{d^k n}{d\epsilon^k}(\epsilon'-\epsilon)^k=\frac{1}{k!}\sum_{k=0}^{n} n^k(\epsilon)(\epsilon'-\epsilon)^k \tag{2.66}$$

we can write the entropy as

$$S=\sum_{k=0}^{\infty} c_k n^{k-1}(\mu)\sigma^k \tag{2.67}$$

where coefficient

$$c_k=(-1)^{k+1}\frac{1}{k!}\int_{-\infty}^{\infty} x^{k+1}\hat{\delta}(x)\,dx \tag{2.68}$$

We will define the $\delta(x)$ which is used in the calculations of this work in Chapter 3.

2.2 Obtaining the Compton Profiles from the GWA

In this section, we will outline the tools that are used to describe Compton scattering beyond impulse approximation. We start with defining the Green's function and self-energy terms. These terms are then used to obtain Hedin's GWA equations. We finally discuss the spectral function and its properties.

2.2.1 Compton Scattering Beyond Impulse Approximation

KS eigenvalues should be interpreted as quasiparticle energies directly measured by photoemission experiments (photons excite electrons out of a crystal leaving holes behind and providing information about occupied states). There is however no theoretical justification for this statement except for highest occupied states. Kohn-Sham DFT with the LDA functional is not an exact theory to calculate momentum density (Olevano et al., 2012). It is a local and energy independent approximation to the self-energy and gives the correct ground state density. The LDA can provide the overall description of Compton profiles and Fermi surface signatures. However, the LDA profile bears sharper fine structures than the observed profile. It yields profiles higher than experimental profile at small momenta and lower at higher momenta with a broadened Fermi surface. This drawback is said to be due to ignoring electron-electron correlation and quasiparticle behaviour in the independent particle model (Kubo, 2001). In the case of weakly correlated materials, the LDA gives a good description of ground state properties but not excited state properties.

The GW Approximation (GWA) enables first principles quasiparticle calculations for realistic materials. It is a first order perturbation theory where the starting Hamiltonian is as close as possible to that of the real system (Kubo, 1996). To calculate quasiparticle energies in our GWA study, Green's function theory is employed. In this formulation, the many body effects are contained in self-energy operators which are non-local and energy dependent. The equation of motion is developed via the Heisenberg representation to obtain the equation of motion of the Green's function referred to as the Dyson's equation. With this term, we then obtain the two particle Green's function. To evaluate the perturbation expansion of the self-energy, the functional derivative technique is employed. Using the Dirac picture, we can obtain a perturbation expansion of the self-energy and rewrite the two particle Green's function in terms of the single particle Green's function and its perturbation expansion.

With this single particle zeroth order Green's function we can then obtain the self-energy in terms of the GW Approximation via Hedin's equation. In this method, we find the product of the Kohn-Sham states as the Green's function with the irreducible polarizability represented by the dynamically screened interaction from the random phase approximation (RPA) which will give the dielectric function. In this formalism, the dynamically screened interaction splits the self-energy into an exchange and correlation term. In more technical terms, the irreducible polarizability, microscopic dielectric function and oscillator matrix elements is written in Fourier space where the exchange self-energy is a static term and has the same term as the Fock operators and the correlation part contains the calculation of dynamical effects in terms of either the plasmon-pole or contour deformation technique. The imaginary part of the Green's function is the calculated spectral function. This can be done by integrating the spectral function with respect to energy (Lebesgue et al., 2003). The GWA is a lowest order many body perturbation theory (MBPT) in terms of fully screened electron-electron interaction. The GWA is the simplest theory beyond the Hartree-Fock approximation (HFA) that takes into account screening (Hedin, 1965; Hedin et al., 1969). It is in fact a generalization of HFA but with dynamically screened interaction. It is the first term in the perturbation expansion of the self-energy in powers of screened interaction, W. A caveat in this calculation is that a higher level of self-consistency both on G and W reduces the level of correlation and increases discontinuity at the Fermi break (Olevano et al., 2012). However, excited state calculation is already calculated in the GWA with the self-energy (Huotari et al., 2007). In previous fully dressed Green's functions, the self-energies are obtained by screening the Coulomb potential by the RPA dielectric function and convoluting with the Green's function (Sternemann et al., 2000).

Besides the study of Compton profiles, the one electron Green's function methods can be used to determine the ionization potential since the poles of the one-particle Green's function correspond to the electron addition and removal energies and the smallest removal energy is just the ionization potential (Grüneis et al., 2014). Other methods to study the effects of self-energy in the ionization potential involve the Breit interaction and quantum electrodynamics (QED) terms (Pyykko, 2011; Pyykko et al., 1998). In these works, they studied the Lamb shift for groups 1 and 11 neutral atom valence electrons. The ionization potential contains two terms, the vacuum polarization term obtained from the Uehling potential (Uehling, 1935) which is strongly localized to the nuclear neighborhood and the self-energy term which can be treated by obtaining a complete set of one-particle states at the Dirac level then doing the Feynman diagram. In the field of few electron computations, the self-energy is evaluated from a non-relativistic density formula for light elements and is treated as a short distance effect. An effective atomic potential in the Dirac problem was then used to simulate the Dirac-Fock valence eigenvalues in terms of QED. Barbiellini (Barbiellini et al., 2004) proposed the application of Dyson orbitals to obtain the Kohn-Sham energies and observed that it can be made closer to experimental band gaps and eigenvalues when used in a quasiparticle correction. Rodl (Rodl et al., 2012) has used the Bethe-Salpeter equation to study the absorption spectra which is computed from the macroscopic dielectric function in the case of late transition metal oxides. Its real and imaginary parts describe the dispersion and abosrption of light. To solve the Bethe Salpeter equation, Rodl firstly obtained the electron hole pair Hamiltonian determined by quasiparticle states from the electronic band structure, matrix element of screened electron hole attraction and matrix elements of bare Coulomb interaction and local field effects. Spin degrees of freedom in terms of singlet and triplet excitations are not well defined as only vertical excitations from a valence to conduction band with same spin quantum number can take place. The eigenvalue is the solved as a time evolution initial value problem which yields the frequency dependent dielectric function but not individual excitonic eigenvalues/oscillator strengths. The matrix elements of electron hole attraction are obtained via analytic expression (Bechstedt et al., 1992). This is compared to the work of Vinson (Vinson et al., 2011) who presented a hybrid approach for BSE core excitation spectra calculations. It includes an explicit treatment of quasiparticle effects within Hedin's GWA and particle hole interactions. It is based on the quasiboson formalism and the many pole self-energy model to account for quasiparticle damping and self-energy shifts. Intraatomic Coulomb and spin orbit interaction are accounted for by atomic multiplet effects. Prange (Prange et al., 2009*)* has attempted to calculate the optical response for a variety of systems and spectral ranges. It is based on real space multiple scattering theory which treats arbitrary aperiodic systems over a broad frequency range. They have used the independent quasiparticle approximation for single particle states. Starting from the bare response function in terms of ψ_o

$$\chi^0(\vec{r},\vec{r}\,',\omega)=\frac{\sum_{i,j}(f_i-f_j)\,\psi_i^0(\vec{r})\,\psi_i^0(\vec{r}\,')\,\psi_j^0(\vec{r}\,'')\,\psi_j^0(\vec{r}\,')}{\omega-(E_j-E_i)+i\,\delta} \tag{2.69}$$

We can obtain the dielectric function as

$$\epsilon_2(\omega)=\frac{4\pi}{V}Im\int d\vec{r}\,d\vec{r}\,'Tr\,d\,\chi(\vec{r},\vec{r}\,',\omega)d^{\dagger} \tag{2.70}$$

These terms can now be written in terms of a single particle Green's function and density operator

$$\chi^0(\vec{r},\vec{r}\,',\omega)=\int_0^{E_F}\rho(\vec{r},\vec{r}\,',\omega)G^{+(\vec{r},\vec{r}\,',\omega)}+\rho(\vec{r},\vec{r}\,',\omega)\,G^{-(\vec{r},\vec{r}\,',\omega)}dE \tag{2.71}$$

And the dielectric function in terms of spectral functions

$$\frac{-Im\chi^0}{\pi}=\int_{E_{F-\omega}}^{E_F}\rho(\vec{r},\vec{r}\,',E)\rho(\vec{r},\vec{r}\,',E+\omega)dE \tag{2.72}$$

Electrons move in an effective quasiparticle scattering potential including the dynamic self-energy correction. Specifically, this potential is a muffin tin potential for a cluster of atoms at fixed location. The Green’s function for this potential is written as a double angular momentum expression

$$G(\vec{r},\vec{r}\,',\omega)=-2k\sum_{LL'} R_{\ln}\vec{r}_{n}G_{\ln,\hat{L}'n'}R_{\vec{L}'n'}(\vec{r}\,'_{n}{}')+\delta_{nn'}\sum_{L} H_{\ln}(\vec{r})R_{\ln'}(\vec{r}_{c}) \tag{2.73}$$

To include relativistic effects such as spin orbit interaction, the Green’s function is recast in terms of spinor solutions to Dirac’s equations.

2.2.2 Green's Function and Self-energy

The propagator is defined as the probability amplitude for the propagation of an added or removed electron in a many body system (Mattuck, 2012). The probability amplitude itself is the overlap between final and initial states in the Heisenberg representation (Heisenberg, 1925)

$$iG(x,x')=\langle\Psi|T[\hat{\psi}(x)\hat{\psi}^{\dagger}(x')]|\Psi\rangle=\begin{matrix}\langle\Psi|T[\hat{\psi}(x)\hat{\psi}^{\dagger}(x')]|\Psi\rangle & \mathit{for}\, t>t' \\ \langle\Psi|T[\hat{\psi}^{\dagger}(x')\hat{\psi}(x)]|\Psi\rangle & \mathit{for}\, t<t'\end{matrix} \tag{2.74}$$

Here, T is the time ordering operator, *G* contains information of charged excitations and $\widetilde{\psi}(x)\widetilde{\psi}^{\dagger}(x)$ is the ground state creation and annhilation field operators. Thus, the one-particle Green function describes the propagation of a hole or added electrons. The top-most relation describes the probability amplitude that creation of an electron at time *t*′ on *x*′ will propagate to *x* at time *t*. The bottom relation describes the probability amplitude that creation of a hole at time *t* on *x* will propagate to *x*′ at time *t*′. From the Green's function we can obtain the expectation value of the single particle operator in ground state, the ground state energy and the excitation spectrum. The formalisms and discussions used in this section is presented in Chapter 1 in (Anisimov, 2000) by Aryasetiawan and the review paper of Aryasetiawan (Aryasetiawan et al., 1998) and we have explicitly defined the derivation steps from that work. Other extremely useful reviews are (Migdal, 1957; Friedrich et al., 2006; Strinati 1988; Onida et al., 2002; Held et al., 2011; Hedin, 1999; Csanak et al., 1971; Aulbur et al., 1999).

The Heisenberg representation of field operators satisfy the equation of motion

$$i\frac{\partial\psi(x)}{\partial t}=[\hat{\psi}(x),\hat{H}] \tag{2.75}$$

whose Hamiltonian is

$$\hat{H}=\int dx\,\hat{\psi}^{\dagger}(x)H_o(x)\hat{\psi}(x)+\frac{1}{2}\int dx\,dx'\,\hat{\psi}^{\dagger}(x)\hat{\psi}^{\dagger}(x')V(x-x')\hat{\psi}(x')\hat{\psi}(x) \tag{2.76}$$

The first term involves the kinetic energy plus a local external field. Putting Equation 2.76 into Equation 2.75, we get

$$\begin{aligned}&\int dx\,\hat{\psi}(x)\hat{\psi}^{\dagger}(x)H_o(x)\hat{\psi}(x)+\frac{1}{2}\int dx\,dx'\,\hat{\psi}(x)\hat{\psi}^{\dagger}(x)\hat{\psi}^{\dagger}(x')V(x-x')\hat{\psi}(x')\hat{\psi}(x)\\&-\int dx\,\hat{\psi}^{\dagger}(x)H_o(x)\hat{\psi}(x)\hat{\psi}(x)-\frac{1}{2}\int dx\,dx'\,\hat{\psi}^{\dagger}(x)\hat{\psi}^{\dagger}(x')V(x-x')\hat{\psi}(x')\hat{\psi}(x)\hat{\psi}(x)\end{aligned} \tag{2.77}$$

Multiplying Equation 2.77 with $\widetilde{\psi}^{\dagger}(x)$ we get

$$\hat{\psi}^{\dagger}(x')\, i\frac{\partial\psi(x)}{\partial t}=\int dx\,\hat{\psi}^{\dagger}(x')\hat{\psi}(x)\hat{\psi}^{\dagger}(x)H_o(x)\hat{\psi}(x)$$
$$-\frac{1}{2}\int dx\,dx'\,\hat{\psi}^{\dagger}(x')\hat{\psi}^{\dagger}(x)\hat{\psi}^{\dagger}(x')V(x-x')\hat{\psi}(x')\hat{\psi}(x)\hat{\psi}(x) \tag{2.78}$$

After evaluating the commutator, we obtain the equation of motion of the Green's function

$$[i\frac{\partial}{\partial t}-H_o(x)]G(x,x')$$
$$+i\int d^3r\,V(r-r')\langle\Psi|T[\hat{\psi}^{\dagger}(r,t)\hat{\psi}(r,t)\hat{\psi}(r',t')\hat{\psi}^{\dagger}(r',t')]|\Psi\rangle \tag{2.79}$$

where the second term is the two particle Green's function which describes the propagation of two particles from 2,4 to 1,3 when written as

$$G_2(1,2,3,4)=i^2\langle\Psi|T[\hat{\psi}(1)\hat{\psi}(3)\hat{\psi}^{\dagger}(2)\hat{\psi}^{\dagger}(4)]|\Psi\rangle \tag{2.80}$$

It can be expressed in terms of one-particle Green's function by rewriting the equation of motion as

$$[i\frac{\partial}{\partial t}-H_o(x)]G(x,x')-\int dx\,M(x,x')G(x,x')=\delta(x-x') \tag{2.81}$$

In the case of molecules or finite systems, the self-energy is calculated via the finite order perturbation theory (Anisimov, 2000). This method does not work on extended systems due to the long range nature of Coulomb interaction. In this case, an infinite order sum of diagram is needed. To evaluate the perturbation expansion of the self-energy, the functional derivative technique is employed. The field operators are firstly rewritten in the Dirac picture

$$|\psi(r,t)\rangle=\hat{U}(t,t_o)|\psi(r,t_o)\rangle \tag{2.82}$$

where

$$\hat{U}(t,t_o)=T\exp[-i\int_{t_o}^{t} d\tau\,\hat{\phi}(t)] \tag{2.83}$$

and

$$\hat{\phi}(t)=\int d^3r\,\phi(r,t)\,\hat{\psi}_D^{\dagger}(r,t)\,\hat{\psi}_D(r,t) \tag{2.84}$$

Defining

$$\hat{S}=\hat{U}(\infty,-\infty) \tag{2.85}$$

we write

$$\hat{U}(\infty,-\infty)=T\exp[-i\int_{-\infty}^{\infty} dt\int d^3r\,\phi(r,t)\,\hat{\psi}_D^{\dagger}(r,t)\,\hat{\psi}_D(r,t)] \tag{2.86}$$

Finding

$$\frac{\partial\hat{S}}{\partial\phi(3)} \tag{2.87}$$

gives

$$i\frac{\partial\hat{S}}{\partial\phi(3)}=T[\hat{S}\,\hat{\psi}_D^{\dagger}(3)\,\hat{\psi}_D(3)] \tag{2.88}$$

where

$$\hat{\psi}_D^{\dagger}(3)\,\hat{\psi}_D(3) \tag{2.89}$$

is the coefficient to *$\phi(3)$*. With this result, we can write

$$i\frac{\partial \hat{G}(1,2)}{\partial \phi(3)} = \frac{\partial}{\partial \phi(3)} \frac{\langle \Psi_o | T[\hat{S}\,\hat{\psi}_D(1)\,\hat{\psi}_D^{\dagger}(2)] | \Psi_o \rangle}{\langle \Psi_o | \hat{S} | \Psi_o \rangle} \tag{2.90}$$

Using the formula

$$\frac{d}{dx}\{\frac{u}{v}\} = \frac{v\,du - u\,dv}{v^2} \tag{2.91}$$

we can rewrite Equation 2.90 as

$$\frac{\begin{aligned} &= \langle \Psi_o | \hat{S} | \Psi_o \rangle \langle \Psi_o | T[\frac{\delta \hat{S}}{\delta \phi(3)}\,\hat{\psi}_D(1)\,\hat{\psi}_D^{\dagger}(2)] | \Psi_o \rangle \\ &- \langle \Psi_o | T[\hat{S}\,\hat{\psi}_D(1)\,\hat{\psi}_D^{\dagger}(2)] | \Psi_o \rangle \langle \Psi_o | \frac{\delta \hat{S}}{\delta \phi(3)} | \Psi_o \rangle \end{aligned}}{\langle \Psi_o | \hat{S} | \Psi_o \rangle^2} \tag{2.92}$$

This will finally give

$$\frac{\partial G(1,2)}{\partial \phi(3)} = G(1,2)\,G(3,3^{+'}) - G_2(1,2,3,3^{+'}) \tag{2.93}$$

We can replace the two particle Green's function from Equation 2.93 into Equation 2.81

$$\int d^3 r'\, v(r-r')\, G_2(1,2,3,3^{+'}) = \int d^3 r'\, v(r-r')[G(1,2)\,G(3,3^{+'}) - \frac{\partial G(1,2)}{\partial \phi(3)}] \tag{2.94}$$

Defining

$$v_H(1)=\int d2\, v(1-2)\rho(2) \tag{2.95}$$

we conclude

$$\int d^3r'\, v(r-r')G_2(1,2,3,3^{+'})=v_H(1)G(1,2)-\int d^3r'\, v(1,3)\frac{\partial G(1,2)}{\partial\phi(3)} \tag{2.96}$$

The Dyson equation establishes a connection between fully interacting *G* and propagator *G_o* via the self-energy

$$G(12)=G_o(12)+\int G_o(13)\Sigma(34)G(42)\,d34 \tag{2.97}$$

The self-energy describes the quantum mechanical state of a renormalized electron in a many body system. It can be obtained by solving the quasiparticle equation

$$[\hat{h}_o(r_1)+v_H(r_1)]\Psi(r_1)+\int \Sigma(r_1,r_2,\epsilon^{QP})\Psi(r_2)\,dr_2=\epsilon^{QP}\Psi(r_1) \tag{2.98}$$

The quasiparticle eigenstates construct *G* according to Lehmann representation. The Lehmann spectral representation is used to define the propagator which gives information on charged excitations

$$\epsilon_i=\begin{matrix}E_i^{(N+1)}-E_0^N & \epsilon_i>\mu\\ E_0^N-E_i^{(N-1)} & \epsilon_i<\mu\end{matrix} \qquad\qquad \Psi_i(r)=\begin{matrix}\langle\Theta_o^N|\hat{\psi}(r)|\Theta_i^{N+1}\rangle\\ \langle\Theta_i^{N-1}|\hat{\psi}(r)|\Theta_o^N\rangle\end{matrix} \tag{2.99}$$

where E_O is the ground state energy, E_i is the excited state energy μ is the chemical potential and $\Psi_I(r)$ are the Lehmann amplitudes. It contains the complete excitation spectrum corresponding to excitations of *N-1* particles and *N+1* particles. The poles in the Green's functions provides the information needed to interpret processes measured in experiments where a single electron is added or removed. The quasiparticle eigenvectors and eigenvalues have direct physical meaning and can be used to obtain interacting system charge density and properties of charge excitations. The QP energies and wavefunction are determined from the solution of the QP equation

$$(T+v_{ext}+v_H)\Psi_{kn}(r)+\int d^3r'\Sigma(r,r',E_n(k))\Psi_{kn}(r)=E_n(k)\Psi_{kn}(r) \qquad (2.100)$$

The major difficulty is finding an adequate approximation of the self-energy operator. Hedin's GW Approximation can determine the self-energy by writing it as a product of the Green's function and screened Coulomb interaction. Both non-locality and dynamical correlations are included.

2.2.3 Hedin's Equations and GWA

The solution to Hedin's equation gives the exact self-energy and exact G. Its building blocks start with the irreducible polarizability

$$\chi(12)=\frac{\partial n(1)}{\partial U(2)}=-i\frac{\partial G(1 1^{+'})}{\partial U(2)} \qquad (2.101)$$

It describes the linear response of density to charges in total effective potential which consists of external field and Hartree potential. With the polarizability, we can then obtain the dielectric matrix

$$\epsilon(12)=\delta(1,2)-\int v(1,3)\chi(3,2)d3 \qquad (2.102)$$

Applying the RPA to the dielectric matrix (Stefanucci et al., 2013), we can obtain the dynamically screened interaction

$$W(1,2)=\int \epsilon^{-1}(1,3)\,v(3,2)\,d3 \tag{2.103}$$

which is the renormalized bare Coulomb interaction giving screened interaction. The next building block is to obtain the many body propagator, G. This is followed by the vertex function, ˆ which describes interactions between virtual hole and electron excitations. With these three building blocks we can finally obtain the self energy.

$$\Sigma=GW\Gamma \tag{2.104}$$

Hedin's GW Approximation can determine the self-energy by writing it as a product of the Green's function and screened Coulomb interaction. Both non-locality and dynamical correlations are included (Lebesgue et al., 2003). The direct evaluation of the vertex function is very challenging. The GW approximation approximates the vertex function with a local and instantaneous function

$$\Gamma(12;3)\approx\delta(1,2)\delta(1,3)\equiv\Gamma^{GW}(12;3) \tag{2.105}$$

From the neglect of vertex correction, the irreducible polarizability become

$$\chi(1,2)=-iG(1,2)G(2,1^{+'}) \tag{2.106}$$

The self-energy can be written in terms of propagator and dynamically screened interactions

$$\Sigma(1,2)=iG(1,2)W(1^{+'},2) \tag{2.107}$$

which when convoluted in frequency space

$$\Sigma(r_{1,}r_{2,}\omega)=\frac{i}{2\pi}\int e^{i\omega'\delta^{+'}}G(r_{1,}r_{2,}\omega^{+'})W(r_{1,}r_{2,}\omega^{+'})d\omega' \tag{2.108}$$

In practical terms, best G and W are used

$$\Sigma(12)=iG_o^{KS}(12)W_o(1^{+'}2) \tag{2.109}$$

where

$$G_o^{KS}(12) \tag{2.110}$$

represents the independent particle propagator of the KS Hamiltonian and

$$W_o(1^{+'}2) \tag{2.111}$$

represents the screened interaction calculated from RPA with KS energies and wavefunctions.

$$\chi_o(1,2)=-iG_o^{KS}(1,2)G_o^{KS}(2,1^{+'}) \tag{2.112}$$

2.2.4 Spectral Function

With the GWA we are able to model the final state interacting electron which may explain the deviation of the DDSCS beyond the impulse approximation, giving insight into experimental results. In this case, the final state electron is the polarized recoil electron which is affected by the so called self-energy effects. These effects are taken into account via the spectral density function *A(p,E)* which describes the relative probability per unit of energy for the system to be in a state with energy $E+\mu$ after the injection of one electron (Soininen et al., 2001; Ng et al., 1986). The spectral density function in terms of self-energy is given by

$$A(p,E)=-\frac{1}{\pi}\frac{Im\Sigma}{[E-\epsilon(p)-Re\Sigma(p,E)]^2+[Im\Sigma(p,E)]^2} \tag{2.113}$$

The first term in the denominator describes how far the energy of the centre of *A(p,E)* is from *ε(p)* while the second term describes the spectral width which is the reciprocal of the lifetime of the quasiparticle. Without the self-energy terms, the spectral function will only contain *E-ε(p)* in the denominator and is typical of ground state calculations. This explains why fine structures tend to be sharper compared to more broadened excited state calculations. The effect of the imaginary part of the self-energy can be obtained by replacing the delta function in Equation 2.27 with *A(p+ħq,E+ħω)*. Under the assumption of the impulse approximation, the spectral function can be modeled as a Dirac delta function and with the electron state given as a plane wave (Huotari et al., 2007; Olevano et al., 2012). Using Equation 2.113, instead of a Dirac delta function to define the occupation number density implies that our model will include correlation terms in particular the self energy. An occupation number density similar to a step function along the Fermi energy would be similar to the case of the LDA a noninteracting system at equilibrium at zero temperature.

This spectral function contains previously reported characteristics. The broadening of the Compton profile beyond impulse approximation can be explained by the finite width of the spectral function of the excited particle (Sternemann et al., 2000). This width grows with increasing electron density (Huotari et al., 2007). Characteristic peaks and structures in the spectral function are indicative of plasmaron and quasiparticles. These asymmetrical shapes are influenced by the polarization function to obtain the self-energy (Sternemann et al., 2000). The GWA reproduces the correct spectral weight repartition between quasiparticle peak and other satellites but the positioning of the satellites is inaccurate (Olevano et al., 2012). In the case of GWA, exclusion of plasmaron and vertex correction affect correlation and subsequently the spectral function (Soininen et al., 2001).

The momentum density can thus be obtained from the spectral function via

$$\rho(p)=\int_{-\infty}^{E_F}(dE/2\pi)A(p,E) \tag{2.114}$$

Thus, it can be seen that the spectral function for the interacting final state electron will modify the dynamic structure factor (Soininen et al., 2001) as given in Equation (2.39). We can now rewrite the dynamic structure factor in terms of the spectral functions in the high momentum transfer regions as the relation between *A(p,E)* and the dynamic structure factor *S(q,ω)* is given by

$$S(q,\omega)=\frac{2}{\hbar}\int_{-\infty}^{0}dE\int\frac{dp}{(2\pi)^3}A(p,E)A(p+q,\omega+E) \tag{2.115}$$

where *A(p,E)* and *A(p+q,E+ω)* is the spectral function for the final state hole and electron respectively. With this term, it is possible to study the correlation contribution to the momentum density. An occupation number density similar to a step function along the Fermi energy would be similar to the case of the LDA which describes a noninteracting system at equilibrium at zero temperature. Specifically, LDA calculations are able to explain the overall shape and fine structures of the observed profile but the momentum densities at the origin are greater than experimental values at the origin but opposite in the high momentum case. In addition, a renormalization of the height of break at the Fermi surface is seen (Olevano et al., 2012). In a previous study, using a dilogarithmic function and Legendre chi functions, Soininen (Soininen et al., 2001) constructed analytical spectral functions based on plasmon energy and ground state energy and equivalently obtained width and splitting of main and satellite peaks.

2.3 Comparative Tools between Experimental and Theoretical Studies

In this section, we introduce the Lam-Platzman correction (LPC) to the Compton profile. With this correction to the momentum density we are able to account for correlations between states. We then discuss the work of Cardwell who proposed an exchange correlation correction based on LPC. They firstly obtained a fit to the Lundqvist (1968) data, then the LPC is obtained by subtracting this fit from the free electron Compton profile. Kubo then observed that the homogeneous part can be modeled by GWA quite satisfactorily. We end this section by discussing anisotropy in Compton profiles.

2.3.1 Lam-Platzman Correction

The Lam-Platzman correction is defined as the difference between the occupation function for a non-interacting and homogeneous interacting electron gas (Huotari et al., 2007), effectively estimating the correlation effects in the Compton profile. Lam (Lam et al., 1974) firstly proposed a general formalism determining momentum density and Compton profiles for interacting electron systems based on the Feynman's theorem and the Hohenberg-Kohn theory. They assumed a non-relativistic and zero temperature system. The Feynman's theorem is given by

$$N(p)=\left[\frac{\partial E_p(\lambda)}{\partial \lambda}\right]_{\lambda=0} \qquad (2.116)$$

where $E_p(\lambda)$ is the ground state energy of

$$H_p(\lambda)=H+\lambda a_p^\dagger a_p \tag{2.117}$$

The Hohenberg-Kohn Hamiltonian is given by

$$H=T+U+V \tag{2.118}$$

where

$$T=\frac{1}{2}\int \nabla\psi^\dagger(\vec{r})\psi(\vec{r})d\vec{r} \tag{2.119}$$

$$U=\frac{1}{2}\int \frac{1}{|\vec{r}-\vec{r}\,'|}\psi^\dagger(\vec{r})\psi^\dagger(\vec{r}\,')\psi(\vec{r}\,')\psi(\vec{r})d\vec{r}\,'d\vec{r} \tag{2.120}$$

$$V=\int V(\vec{r})\psi^\dagger(\vec{r})\psi(\vec{r})d\vec{r} \tag{2.121}$$

can be written in terms of annhilation operators for plane wave states e.g.

$$T=\sum_k \epsilon_k(p)a_k^\dagger a_k \tag{2.122}$$

where

$$\epsilon_k=\frac{1}{2}k^2 \tag{2.123}$$

We can thus write Equation 2.118 as

$$H_p(\lambda)=T_p+U+V \tag{2.124}$$

where

$$T_p=\sum_k \epsilon_k(p)a_k^{\dagger}a_k \tag{2.125}$$

with

$$\epsilon_k(p)=\epsilon_k+\lambda\delta_{p,k} \tag{2.126}$$

Replace everywhere ε_k by $\varepsilon_k(p)$ in ground state energy E of H, we will get $E_p(\lambda)$ to fulfill Equation 2.113. Thus, to obtain Equation 2.113 from the above-mentioned Hamiltonian, we apply two assumptions from the Hohenberg-Kohn theorem

(a) Ground state energy E is a unique functional from of $n(r)$

(b) E is stationary with respect to $\partial n(r)$

Defining

$$n(\vec{r})=\langle\phi_o|\hat{\psi}^{\dagger}(\vec{r})\hat{\psi}(\vec{r})|\phi_o\rangle \tag{2.127}$$

we write

$$E[n]\equiv\int V(\vec{r})n(\vec{r})d\vec{r}+\frac{1}{2}\int\frac{n(\vec{r})n(\vec{r}\,')}{|\vec{r}-\vec{r}\,'|}d\vec{r}\,d\vec{r}\,'+G[n] \tag{2.128}$$

Since $n(r)$ can also be written in terms of annhilation operators, it also has a dependence on ε_k. We can thus write the momentum density and G terms in terms of λ which gives two sources of λ dependence in $E_p(\lambda)$, $G_\lambda[n_\lambda]$ and $n_\lambda(r)$. Based on assumption b),

$$[\frac{\partial E_p(\lambda)}{\partial \lambda}]_{\lambda=0} = [\frac{\partial G_\lambda(n)}{\partial \lambda}]_{\lambda=0} \quad (2.129)$$

We can thus rewrite Equation 2.116 as

$$N_p = \frac{\partial G(n)}{\partial \epsilon_p} \quad (2.130)$$

The exact form of *G[n]* is unknown. An approximation scheme must be used to calculate the Compton profile. Lam proposed a self-consistent scheme for utilizing the results of density calculations to obtain the approximate Compton profile. Based on the Kohn-Sham method, we replace the many electron problem via self-consistent one-electron equations. We firstly split *G[n]* to two terms

$$G[n] = T[n] + E_{xc}[n] \quad (2.131)$$

This can be related to

$$[\frac{p^2}{2m} + V_{eff}(\vec{r})]\psi_i(\vec{r}) = E_i \psi_i(\vec{r}) \quad (2.132)$$

where

$$V_{eff} = V(\vec{r}) + \frac{1}{2}\int \frac{n(\vec{r})n(\vec{r}\,')}{|\vec{r}-\vec{r}\,'|} d\vec{r}\, d\vec{r}\,' + V_{xc}(\vec{r}\,') \quad (2.133)$$

$$V_{xc}(\vec{r}) = \frac{\partial E_{xc}(n)}{\partial n(\vec{r})} \quad (2.134)$$

Putting Equation 2.133 into Equation 2.134 we write the energy as

$$E=\sum_{i=1}^{n} E_i-\frac{1}{2}\int\frac{n(\vec{r})n(\vec{r}\,')}{|\vec{r}-\vec{r}\,'|}d\vec{r}\,d\vec{r}\,'+E_{xc}[n]-\int V_{xc}(\vec{r})n(\vec{r})d\vec{r} \tag{2.135}$$

Taking into account the assumption (b) we write

$$N_p=\sum_{i=1}^{n}\frac{\partial E_i}{\partial\epsilon_p}+\frac{\partial E_{xc}[n]}{\partial\epsilon_p}-\int\frac{\partial V_{xc}}{\partial\epsilon_p}n(\vec{r})d\vec{r} \tag{2.136}$$

Using

$$N_p=\sum_{i=1}^{N}|\langle p|\phi_i\rangle|^2 \tag{2.137}$$

we write the first term in Equation 2.136 as

$$\frac{\partial E_i}{\partial\epsilon_p}=|\langle p|\psi_i\rangle|^2+\langle\psi_i|\frac{\partial V_{xc}(\vec{r})}{\partial\epsilon_p}|\psi_i\rangle \tag{2.138}$$

This gives Equation 2.136 to be

$$N_p=\sum_{i=1}^{n}|\langle p|\psi_i\rangle|^2+\frac{\partial E_{xc}[n]}{\partial\epsilon_p} \tag{2.139}$$

The second term represents corrections to momentum density which are due to correlations between states. We now have a formally exact definition of Equation 2.139 compared to Equation 2.137. Thus, for the local approximation in Equation 2.136

$$\begin{aligned}\frac{\partial E_{xc}[n]}{\partial\epsilon_p}&=\int\frac{\partial\epsilon_{xc}(n(\vec{r}))}{\partial\epsilon_p}n(\vec{r})d\vec{r}\\&=\int[N_p^O(n(\vec{r}))-N_p^F(n(\vec{r}))]n(\vec{r})d\vec{r}\end{aligned} \tag{2.140}$$

The integration is over the entire unit cell. The first term is from the homogeneous electron gas calculation while the second tern is from the free electron gas. This gives the Lam-Platzman correction term describing the effect of exchange correlation on Compton profiles

$$\Delta J^{LDA}(q)=\int_{unit\,cell}\rho(r)[J^{h}-H^{f}]\,d^{3}r \qquad (2.141)$$

This term is required when trying to obtain momentum density from LDA (Kubo, 2005). It improves the LDA momentum density by including the isotropic result of correlation correction (Soininen et al., 2001) and is insensitive to directional dependencies (Kubo, 2001). It is localized and spherically symmetric with no effect on anisotropy and takes into account ground state correlations. Thus, the LPC shows that accurate momentum space occupation numbers must include quasiparticle properties of homogeneous, interacting electron gas with the self-energy as a function of wave vector (Wakoh et al., 1990).

2.3.2 Correlation Correction

Cardwell (Cardwell et al., 1989a; Cardwell et al., 1989b) proposed an exchange correlation correction based on the Lam-Platzman correction (LPC). They firstly obtained a fit to (Lundqvist et al., 1968) data. Then the LPC is obtained by subtracting this fit from the free electron Compton profile. The form of the correction consists of a negative region in the origin, sharp peaks near the Fermi momentum and a high momentum tail.

Comparing the LDA correction with the Compton profile correction reveals that the LDA correction is of greater magnitude although similar in profile. LDA has consistently underestimated Compton profile. At the peak height, the theoretical profiles are overestimated due to neglect of exchange and correlation effects. The effect of exchange and correlation on the Compton profiles is to promote electrons from low to high momenta states (Cardwell et al., 1989). This is due to input difference normalized to one electron and magnified when integrated over unit cell. The high momentum tail is due to core electron distribution as a consequence of large Fermi momentum associated with high charge density. The magnitude of ΔJ^{LDA} at the origin is inversely proportional to the average charge density at the core in which the high exchange and correlation effects with low electron densities. The intermediate form by the distribution of conduction electrons. The LPC always results in a shift of electron density from low to high momenta. This shift reflects degree in which core and conduction electrons are correlated.

Similar to Cardwell's methodology, (Kubo, 1997) has previously observed that the homogeneous part can be modeled by GWA quite satisfactorily. It is based on the similarities between the GWA Compton profile and the Wakoh-Matsumoto empirical correlation correction which is by itself a good fit to experimental data (Wakoh et al., 1990). Kubo defined the difference between the free electron Compton profile and LDA. The experimental correlation corrections are given by

$$\Delta J_{\exp}^{corr}(p_z) = J_{\exp}(p_z) - J_{LDA}(p_z) \qquad (2.142)$$

They made the assumption that since LDA does not consider correlation, $\Delta J_{\exp}^{corr}(p_z)$ describes the correlation correction. Comparing $\Delta J_{\exp}^{corr}(p_z)$ and $\Delta J_{GWA}^{corr}(p_z)$, there are discrepancies. They observe that the correlation correction is a very small proportion of the profiles. Kubo (Kubo, 2001) has studied the correlation correction which is defined as

$$\Delta J_{GWA}^{corr}(p_z) = J_{GWA}(p_z) - J_{LDA}(p_z) \tag{2.143}$$

They observed anisotropic correlation effects due to 3d electrons in comparing the calculated correlation corrections, Wakoh-Matsumoto empirical corrections and Lam-Platzman correction. They also observed the differences lie mainly in the origin.

2.3.3 Anisotropy

We can further analyze this promotion of electrons by studying the directional differences which is a measure of anisotropy (Lam et al., 1974). Specifically it is the difference between the maximum and the minimum of the Compton profile (Cardwell et al., 1989). Anisotropy is strongly dependent on the Fermi surface (Sternemann et al., 2000) and can be used to locate positions of oscillations in the Fermi surface (Kubo, 1996). When comparing two sets of Compton profile experiments, the structure behind oscillations can be explained by the non-local correlations which smears occupied momentum density and populates empty regions. The minimum in the oscillations of the difference plots is due to the plane of integration intersecting the center of the Fermi spheres and the maximum is halfway between planes. The Compton profile based on band structure calculations has excessive anisotropies due to inadequate treatment of exchange and correlation. Positions of anisotropy oscillations is the same as experiment but larger.

2.4 Previous GWA Compton Profile Studies

In previous cases, the alkali and alkali-earth metals in particular have been actively studied for their correlation effects as they are closest to the homogeneous electron gas and have isotropic momentum distributions. The use of the GW Approximation is said to improve the comparison to observation for the Compton profile. Compton profiles for

Li, Be, Na, Cr, Ni and Cu have been obtained from the GW Approximation. Schulke (Schulke et al., 1996) was among the first to remark that final state interaction effects must be taken into account according to work performed on Li.

Kubo (1996) applied the full potential linearized augmented plane wave basis states as input to the GWA. Via the plasmon pole method, they observed plasmon and quasiparticle peaks in their spectral functions. The occupation number density is obtained from these spectral functions. In the case of Li, occupational number densities show directional dependence due to the anisotropy of the electron density distribution and shape of Fermi surface. Comparing the LDA occupation number density to the GWA occupation number density, GWA is found to fit the experimental spectra better than LDA. Fermi surface crossings can be observed by taking the first order differential of the Compton profile. They observe that the GWA Fermi surface crossings are better fits to experiment as well. Later on, it was argued that the Hamada plasmon pole model (Hamada et al., 1990) used by Kubo does not provide an accurate description of the imaginary part of the self-energy, hence momentum distribution (Schulke et al., 1996).

Kubo (1997) studied the sodium Compton profile and observed it can be reproduced from an interacting electron gas model. They also studied the Li Compton profile and determined that it requires the LPC. GWA for sodium reproduces the experimental Compton profile better than LDA. Li has a larger anisotropy on the Fermi surface owed to lattice potential. They used LDA instead of quasiparticle wavefunctions and used only diagonal occupation number densities.

In (Sternemann et al., 2000), the momentum density broadening is obtained from a convolution of the Compton profile with the spectral function. The smearing of the Fermi break is a unique fingerprint of the interaction of the excited electron with the rest of the system. They used a particle-hole vertex correction in their calculation where a

Coulomb interaction between particle and hole is dynamically screened by RPA. It was observed that the second derivative of the experimental Compton profile is closer to the LDA convoluted with the spectral function. The second order derivative reveals the position of the peak at the Fermi momentum (Ohata et al., 2000) and allows to study Fermi surface crossing and high momentum components (Sakurai et al., 1995). It was previously pointed out fine structures available in Al-Li alloy not observed in Al (Matsumoto et al., 2000). Even though Al is suppose to have an isotropic Fermi surface, Suortti (Suortti et al., 2000) observed anisotropy as a result of neglect of electron correlation in their study of Al based on the model of Schulke (Schulke et al., 1996). Valence Compton profiles are found to be asymmetric in shape and the sharp features of the Fermi break are drastically smeared out. Sternemann concluded that deviations in LDA and quantum Monte Carlo calculations from experiment can be understood in terms of how deviation from the impulse approximation affects experimental Compton profiles and momentum densities. An indication that the impulse approximation is not obeyed is the observation of final state interactions even during high probing energies. In the jellium model, the impulse approximation means neglecting final state interactions which are interactions of excited particle with hole left begin in the form of polarization.

Soininen et al. (2001) observed that the shape of the spectral function at high momentum regime changes quite slowly but resembles the quasiparticle peak. They calculated the self-energy analytically by firstly obtaining the plasmon energy and ground state energy of the system. Then, using the dilogarithmic functions and Legendre chi functions, they obtain the analytical spectral functions. The plasmarons are neglected and vertex corrections are neglected while the crystal potential is found to have a small effect on the final state electrons. Plasmarons are quasiparticles arising in a system containing strong plasmon electron interactions (Bostwick et al., 2012). They observe that the width and splitting of the main and satellite peaks are very close to each other. The spectral function changes shape over a small range of electron densities (electron densities are a function of atomic number). As momentum transfer increases, the spectral function becomes narrower and the satellite peak becomes broader as the spectral weight increases. At higher momentum transfer, final state effects become less important. The limitation of experiment in comparison to theory is determined by resolution and statistical accuracy. Unexplained differences are attributed to experimental profiles being broader than theoretical profiles.

Kubo (2001) observed that the GWA momentum densities of the first Brillouin zone is moved to a higher momenta which plays the same role as the Lam-Platzman correction with its shortcomings of isotropicity. They rationalize this result based on the work of Wakoh and Matsumoto (Wakoh et al., 1990) where the Fermi level is located in the middle of the d-bands, the radial wavefunction of d-components in higher energy states is more contracted compared to lower energy states and the momentum distribution from higher energy states is more extended compared to lower energy states. The GWA automatically fulfills this criteria as GWA correlation correction is similar to Wakoh-Matsumoto correlation correction.

Kubo (2004) has stated that the spin magnetic moment of Ni is caused by splitting of the 3d band together with negative polarization of s and p like band electrons. The occupied 3d bandwidth is too broad and exchange splitting is overestimated and this has been explained as due to LSDA which does not produce Umklapp shoulders which can be obtained from Fermi surface topology. They observe that the GWA tends to smear Umklapp peaks even in individual band studies which is caused by broadening of the Fermi surface. They also observe that the band narrowing seen in majority and minority spin bands is due to dynamical screening effects in which the use of GWA spectral function reduces by a factor.

In Huotari et al. (2007), final state effects to the electron are obtained by using the formalism of (Soininen et al., 2001) which is convoluted with the valence electron Compton profile. They observed that the spectral function consists of large quasiparticle peaks and small secondary quasiparticle peaks. The finite width of the spectra is due to the self-energy of the final state electron. They conclude that as the incident photon energy gets larger, the Compton profile gets broader. The Compton profile close to the origin is flat and similar to experiment. It has a discontinuity or slope after the Fermi momentum and an end nearing the Brillouin zone edge (Fermi surface crossing). The Compton profile peak height has been found to be lower than theoretically predicted and they conclude that this is due to correlation. Experimental features of the Fermi surface are observed to be broader compared to theory. It is proposed that the antisymmetrized geminal product (Barbiellini, 2000) can account for experiment.

In the case of sodium, Huotari et al. (2010) observed that the Fermi surface is contained in the first Brillouin zone. Sodium has a perfect spherical Fermi surface where a radial momentum density function is observed from from experimental data at the Fermi break. The band structure reduces the discontinuity of the momentum density. In the case of the LDA calculation, the discontinuity is 0.98. The valence band is the perfect parabola, the wavefunction is isotropic and the Fermi surface deviates from the sphere by 0.2 % resulting in small reduction of discontinuity. In their QMC and GWA calculations, the pseudopotentials describe core electrons and electron-phonon coupling in this region is neglected. The core corrections do not influence it as it is a smooth correction. The impulse approximation is not valid for the core electron spectra in their experiments. Band structure effects only lead to small lowering of momentum distribution where explicit electron-electron interactions are turned off via Quantum Monte Carlo calculations. Authors observe that the momentum density within GWA is close to QMC. At low energy experiments, the smearing of Compton profile due to final state effects is overwhelming and exceed experimental resolution while at high energy experiments, the spectral function vanishes and experimental resolution deviates. Experiments enable clear and direct observation of discontinuity at the Fermi surface. Their calculation account for electron-electron interaction and band structure effects. The solution describing the noninteracting crystalline systems is given by the Bloch wave function. The homogeneous electron gas is the canonical workbench to test different theoretical methods. For a noninteracting HEG the Compton profile is an inverted parabola. For an ideal Fermi gas, the momentum density is similar to the Fermi-Dirac distribution with a Compton profile resembling an inverted parabola. The final state interaction is calculated from first principles containing self-energy terms. Jellium is the simplest many body systems that describes several properties of real solids especially alkali metals.

Olevano et al. (2012) calculated the momentum distribution and Compton profile within the framework of GWA on the self-energy. The Green's function was obtained by integrating both cases of real and imaginary axis. Real axis integration is suitable for evaluating momentum distribution far from the Fermi momentum while imaginary axis integration is accurate near discontinuity. They compared their calculations of jellium and sodium to X-ray Compton scattering and quantum Monte Carlo calculations near the Fermi energy. Experimentally, the Compton profile does not resemble the inverted parabola and no discontinuity is observed in the first derivative of the Fermi momentum. As the electron density increases we expect momentum distribution to have more broadening of the Fermi energy. This is observed in the case of jellium. For strongly correlated systems, discontinuity is strongly suppressed. Thus, modification of momentum distribution and reduction of discontinuity is a correlation effect. The momentum distribution and discontinuity provide unique and unambiguous quantification of correlation. They also observe that any departure from the step function case could be due to finite temperature effects, band structure effects, anisotropy of the Fermi surface, electron-phonon interaction and electron-electron interaction. We are particularly interested in electron-electron correlation effects. They then performed integration on the imaginary portion of the ω axis to obtain the momentum distribution and observed the real part of the self-energy is smoother compared to the imaginary part of the self-energy. The correlation effects may induce contributions from higher bands. They then observed the valence electrons of sodium resemble the homogeneous electron gas from the point of view of noninteracting as well as many body interacting observables. Here, the Compton profile of the ideal Fermi gas and LDA has the form of an inverted parabola. Core electron contributions must be subtracted from experimental signal to obtain Compton profiles of valance signals.

Previous calculations that study the LPC and anisotropy compare LDA calculations directly with experiment. Li is found to contain only one electron in conduction bands with strong electron-ion interactions and the one electron picture momentum density is not a homogeneous electron gas and is highly anisotropic (Schulke et al., 1996). Its experimental break at the Fermi momentum appears close to zero and the occupation number densities show directional dependence owed to anisotropy of the electron density and Fermi surface topology. This is observed in Be as well (Huotari et al., 2007). For Al, the magnitude of EMD around the origin and higher momenta is different from experiment but subtle structures still exist. A study of the second order derivative of the Compton profile for the measured momentum density is smaller than the theoretical one at the Fermi momentum (Ohata et al., 2000). In Cu (Kubo, 2005), the Fermi surface is deformed from a sphere which makes the discontinuity in the momentum density sensitive to direction. For Cr (Kubo, 2001), anisotropic correlation effects due to 3d electrons in LPC and Wakoh-Matsumoto correlation correction were observed to differ at the origin. In studies of V and Cr (Wakoh et al., 1990), it was found that correlation effects due to 3d and core electrons are indistinguishable and density distributions should be strongly anisotropic. This agrees with our partial density of states (PDOS) as given in Figure 4 for the case of NiO and is typical of the other TMOs as well.

CHAPTER 3 : COMPUTATIONAL METHODOLOGY

In this chapter, we will discuss some formalisms, methodologies, implementations and parameterizations behind ground state (Section 3.1) and excited state calculations (Section 3.2) as implemented in the software ABINIT (Gonze et al., 2002; Gonze et al., 2009) used in this work. We also include a section on the work flow we have developed to obtain the band structures, spectral functions, momentum densities and Compton profiles (Section 3.3).

3.1 Ground State Calculation

In this section we start our discussion with the parameters concerning the construction of the unit cell and its constituent atoms. We then discuss the representation of the plane wave in terms of periodic supercells and the energy cutoff used to converge this term. This is followed by a discussion on the parameters used to sample energies at specific k-points on the system. We then delve deeper into the representation of the plane wave by discussing the norm-conserving pseudopotential method. With all these constructs described, we can discuss the implementation of the momentum density which is the central term of this work. We then discuss the improvement to the momentum density which is the cold smearing term. We finally discuss the parameters used by ABINIT to construct the band structure and partial density of states.

3.1.1 Geometry

In Table A.1 (Appendix), we present the geometrical parameters used in our calculation. ABINIT employs algorithms accounting for crystallographic properties of each crystal structure (Cracknell, 1975) we initialized so that the calculation runs at its most efficient. Each parameter is used to define the unit cell and the atoms in the cell. In this work, these parameters are initialized from a crystallographic information file (CIF). **znucl** will be initialized by the atomic number of the system we are studying. **acell** is initialized by the cell length from the CIF which are the scaling factors of the primitive vectors. **rprim** defines the primitive unit vector of the unit cell where we have used the face centered cubic, rutile and zinc-blende structure in our calculations. In these studies, the rhombohedral-tetragonal distortions typically seen below the Neel temperature are ignored (Rodl et al., 2009). In order to obtain this parameter from the CIF, we have used the cif2cell program (Björkman, 2011). **xred** is obtained from the atom site data of the CIF. **typat** is obtained from the actual locations of atoms given in xred. Ordering of terms in typat must agree with the input of the nuclear charge of the elements in the array znucl.

3.1.2 Periodic Supercells and Energy Cutoff

Calculations of supercells require handling an infinite number of noninteracting electrons represented by wavefunctions which extends over the entire solid moving in a static potential of an infinite number of nuclei and ions. The formalism to describe this wavefunction is given by the Bloch's theorem which states that in a periodic solid, the wavefunction is the product of a cell-periodic and wavelike part

$$\psi_i(r)=e^{-ik.r}f_i(r) \tag{3.1}$$

The cell-periodic part $f_i(r)$ is expanded using a basis set consisting of a discrete set of plane waves whose wave vectors are reciprocal lattice vectors of the crystal.

$$f_i(r)=\sum_G c_{i,G}e^{-iG.r} \tag{3.2}$$

Here G is a reciprocal lattice vector. Thus, each electronic wave function can be written as a sum of plane waves. This method is known as the Bloch theorem and it is the simplest and most natural formalism to implement crystals. Plane waves obtained from small kinetic energies are more important compared to large kinetic energies. Thus, the plane wave basis set can be truncated to include only plane waves with kinetic energy less than a particular cutoff energy. This produces a finite basis set. The cutoff energy should be increased until the calculated total energy has converged. The developers of ABINIT recommend consulting (Payne et al., 1992) for a thorough and complete review of these methods.

Table A.2 (Appendix) defines the parameters relevant to the setup of the self consistent field (SCF) cycle and convergence of energy. **toldfe** should be set as not smaller than about 10^{-12} of the total energy. When the convergence tolerance on the wavefunctions is satisfied, iterations will stop, so for well converged calculations **nstep** is set to a value larger than needed for full convergence. The larger **ecut** is, the better converged the calculation is. For fixed geometry, the total energy MUST always decrease as ecut is raised because of the variational nature of the problem.

3.1.3 *K*-point Sampling

A description of the electronic wave function in reciprocal states are set by *k*-points which are determined by boundary conditions applied to bulk solids. The density of allowed k-points is proportional to the volume of the solid. Thus, an infinite number of k-points models infinite electronic states occupied at each k-point. Using the previously mentioned Bloch theorem, we can calculate a finite number of electronic states as occupied at an infinite number of k-points and occupied states at each k-point will contribute to the electronic potential of the solid. Since the electronic wavefunctions at k-points close together will be identical, only a finite number of k-points are required to calculate the electronic potential and total energy of solids. For example, metallic systems require dense sets of k-points to define the Fermi surface precisely. This helps to reduce the magnitude of error in total energy due to inadequate k-point sampling. Knowing the k-points, we can provide a plane wave basis set description of the Kohn-Sham equation in reciprocal space.

$$\sum_{G'} \left[\frac{\hbar^2}{2m} |(k+G')|^2 \delta_{GG'} + V_{ion}(G-G') + V_H(G-G') + V_{xc}(G-G') \right] c_{i,k+G'} = E_i c_{i,k+G} \tag{3.3}$$

The kinetic energy only takes the diagonal component and the potential term is Fourier transformed. This Hamiltonian will be diagonalized to solve the Kohn-Sham equation. There are numerous methods proposed to sample these special sets of k-points in the Brillouin zone (Chadi et al.,1973; Monkhorst., 1976). (Setyawan et al., 2010) provides an overview of important k-points for the most common crystal structures in a high throughput calculation setup.

Table A.3 (Appendix) defines all the parameters used in setting up the k-point grid. **kptopt** constructs the k-point list based the input variables initializing the k points, their number, and their weight. Since the k points form a lattice in reciprocal space, the aim is to initialize input variables that give the reciprocal of this k-point lattice, as well as its shift with respect to the origin. The parameters **ngkpt** or **kptrlatt**, as well as **nshiftk** and **shiftk** achieves this. The k point lattice defined by ngkpt or kptrlatt is used to perform integrations of periodic quantities in the Brillouin Zone, like the density or the kinetic energy. When either ngkpt or kptrlatt is defined, kptrlen is not used as an input variable, but the length of the smallest vector will be placed in this variable, and echoed in the output file. In the case of a grid of k points, the auxiliary variables kptrlen, ngkpt or kptrlatt and prtkpt can be used to select the optimal grid. In our calculations, the parameter prtkpt is set to 1, and set **kptrlen** to an arbitrary range between 40 to 200. An output of suggested kptrlatt values will be given based on kptrlen, which can be used for convergence studies.

3.1.4 Norm-conserving Pseudopotentials

Stand alone plane wave basis sets have a shortcoming in describing expanded electron wave functions because of the large number of plane waves required to expand core orbitals and rapid oscillations of valence electron wave functions in the core. By applying the pseudopotential approximation, it allows the electronic wavefunctions to be expanded using a smaller number of plane waves. The motivation for the approximation being that physical properties of solids are more affected by the valence rather than core electrons. Thus, the core electron and its strong ionic potential are replaced with a weaker pseudopotential acting on pseudowavefunctions. The major contribution of the core wavfunction to physical properties are by enforcing the valence wavefunctions orthogonality to core states. In this section we detail the pseudopotential method based on three references, the first being (Troullier et al., 1991) who have developed a procedure to generate first principles norm-conserving pseudopotential which are said to be efficient for slowly converging several thousand plane wave expanded basis set systems such as transition metals when implemented with modern diagonalization techniques. The other two are (Payne et al., 1992; Fuchs et al., 1999) which presents technical details of the pseudopotential method.

Pseudopotentials are generated from an all electron atomic calculations. In DFT, this is obtained by assuming the spherical screening approximation and self-consistently solving the radial Kohn-Sham equation.

$$\left[\frac{-1}{2}\frac{d^2}{dr^2}+\frac{l(l+1)}{2}r^2+V(p,r)\right]r\,R_{nl}(r)=\epsilon_{nl}\,r\,R_{nl}(r) \qquad (3.4)$$

where *V(p,r)* is the self-consistent one-electron potential given by

$$V(p,r)=\frac{-Z}{r}+V_H(p,r)+V_{LDA}(\rho(r)) \tag{3.5}$$

The construction of pseudopotentials satisfies four general conditions which are

a) The valence pseudowavefunction generated from pseudopotentials should contain no nodes as a smooth pseudowavefunction is desirable.
b) The normalized atomic radial pseudowavefunction must be the same as the normalized radial all-electron wavefunction above the cutoff radius.
c) The charge enclosed within the cutoff radius for the wavefunctions must be equal.
d) Valence all-electron and pseudopotential eigenvalues must be equal.

If these conditions are met, the pseudopotential is called a norm-conserving pseudopotential. The pseudowavefunction obtained from a norm-conserving pseudopotential will then be used to obtain the screened pseudopotential

$$V_{scr,l}^{PP}(r)=\epsilon_l-\frac{l(l+1)}{2r^2}+\frac{1}{2\mathrm{r}\,R_l^{PP}(r)}\frac{d^2}{d\,r^2}[r\,R_l^{PP}(r)] \tag{3.6}$$

In this term, the radial Schrodinger equation is a second order linear differential equation whose solution is determined by

$$\frac{d}{dr}\ln[R_l(r,\epsilon)]=\frac{1}{R_l(r,\epsilon)}\frac{d\,R_l(r,\epsilon)}{dr} \tag{3.7}$$

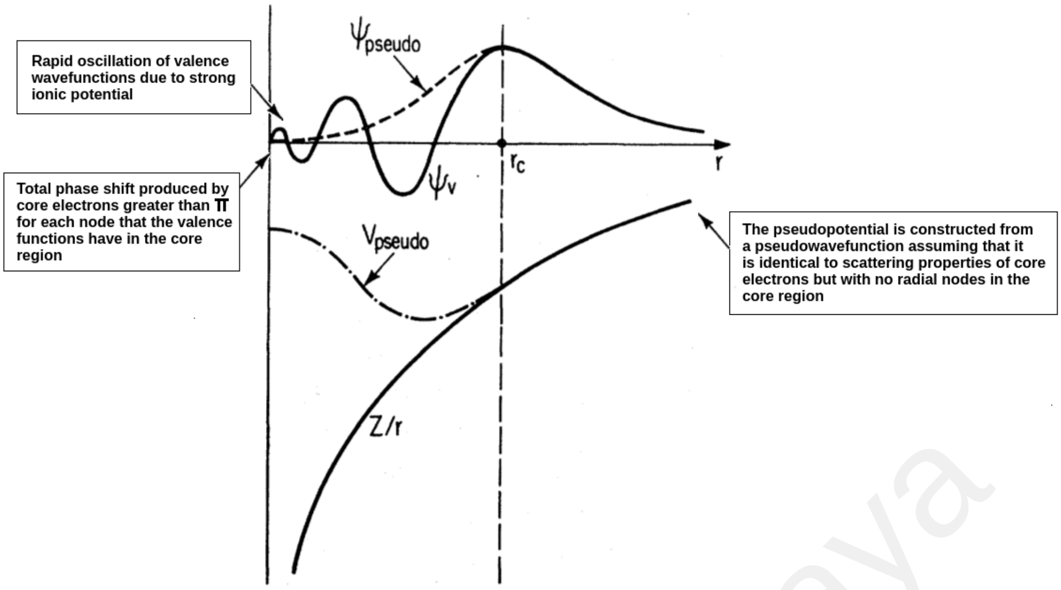

Figure 3.1: The oscillations seen in the core region maintain the orthogonality between core wavefunctions and valence wavefunctions as required by the exclusion principle. Phase shifts produced by core electrons is different for each angular momentum component of valence wave function.

If the screened all-electron potentials and pseudopotentials are identical outside the cutoff radius, the all electron wavefunction and pseudowavefunctions are proportional as well. Thus, the pseudopotential will accurately reproduce the all-electron calculation in the reference configuration it is generated. It is transferable. For a nodeless pseudowavefunction, the pseudopotential does not contain a singularity except at the origin. This ensures a continuous pseudopotential provided that the pseudowavefunction is continuous at the second derivative. Pseudowavefunctions inside and outside the core must be identical to the real wavefunction so that the two wavefunctions generate identical charge densities and the first order energy dependence of the scattering from the ion core is correct. The convergence properties of the pseudopotential are determined by the difference between the electronic energies of the different ionic configurations seen in the valence electron energy. With the screened, Hartree and exchange-correlation pseudopotential, we can then obtain the ionic pseudopotential which can be used in a self-consistent calculation

$$V_{ion}^{PP}(r)=V_{scr,l}^{PP}(r)-V_{H}^{PP}(r)-V_{xc}^{PP}(r) \tag{3.8}$$

To generate the ionic pseudopotential, its operator is given by

$$\hat{V}_{ion}^{PP}(r)=V_{ion,local}^{PP}(r)+\sum_{l} V_{nonlocal,l}(r)\,\hat{P}_{l} \tag{3.9}$$

where the local potential should be chosen such that it adequately reproduces atomic scattering for all higher angular momentum channels. Each angular momentum component of the wavefunction will use a different potential. In the case of a local pseudopotential, the potential is the same for all angular momentum components of the wavefunction and it only depends on the distance from the nucleus. However the arbitrary nature of the local potential is used to produce an accurate transferable pseudopotential. Scattering from the ion core is best described by a nonlocal pseudopotential which uses different potentials for each angular momentum component of the wavefunction. Thus, nonlocal pseudopotentials play an important role in the construction of the ionic pseudopotentials and require efficient schemes in dealing with the nonlocality of the pseudopotential. The partial projection methods are used. For the nonlocal potential, the P_l operator projects out the lth angular momentum component from the wavefunction. The nonlocal potential can be written in terms of the Kleinman-Bylander nonlocal potential (Kleinman et al.,1982)

$$V_{nonlocal}^{KB}(r)=\frac{|V_{nonlocal,l}(r)\,\phi_{l}^{PP}(r)><\phi_{l}^{PP}(r)V_{nonlocal,l}(r)|}{<\phi_{l}^{PP}(r)|V_{nonlocal,l}(r)|\phi_{l}^{PP}(r)>} \tag{3.10}$$

Here, the atomic pseudowavefunction includes the angular momentum component for which the pseudopotential was calculated.

The Schrodinger equation for a crystal using a plane-wave basis set and pseudopotential is given by

$$\sum_{j} H_{ij}(k)\, a(G_j+k)=\epsilon\, a(G_i+k) \tag{3.11}$$

where the momentum space Hamiltonian for point *k* in the Brillouin zone is given by

$$H_{ij}(k)=\frac{1}{2}\delta_{ij}\left|(G+j)^2\right|+V_{local}(G_i-G_j)+V_{nonlocal}(G_i+k-G_j+k) \tag{3.12}$$

The first term is the diagonal kinetic energy operator, the second term is the Fourier transformed local potential with the electron screening potential. The matrix elements for the nonlocal potential is given by

$$\begin{aligned} &V_{nonlocal},l(G_j+k,G_i+k)\\ &=\frac{2l+1}{4\pi\Omega}P_l(\cos\theta)\int_0^\infty V_{nonlocal}(r)\, j_l(|G_j+k|r)\, j_l(|G_j+k|r)\, r^2 dr \end{aligned} \tag{3.13}$$

which consists of the cell volume, Legendre polynomial and spherical Bessel function, which gives the amplitude of the angular momentum component of the plane wave at a distance r from the origin.

3.1.5 Momentum Density

The interaction of valence electrons of a solid and ion cores of a crystal lattice take into account momentum density of inhomogeneous electron system in terms of electron field parameters

$$\rho(p)=\frac{1}{2\pi\hbar}\int dr\int dr'\,e^{[ip.(r-r')/\hbar]}\langle\psi^{\dagger}(r)\psi(r)\rangle \tag{3.14}$$

The thermal average of N electrons

$$\langle\psi^{\dagger}(r)\psi(r)\rangle \tag{3.15}$$

is constructed from Bloch waves. This gives an electron momentum density of

$$\rho(p)=\sum_{bb'}\sum_{k}\sum_{G}n_{bb'}(k)\alpha_b^{*}(k+G)\alpha_b{}'(k+G)\delta(k+G-p/\hbar) \tag{3.16}$$

where

$$n_{bb'}(k)=\langle a_{k,b}^{\dagger}a_{k,b}\rangle \tag{3.17}$$

is the mean occupation density of Bloch states. The momentum density is obtained from the plane wave function

$$\Psi(r,t)=\sum_{k}\sum_{b}\alpha_{k,b}(t)\phi_{k,b}(r),\phi_{k,b}(r)=\frac{1}{(2\pi\hbar)^{3/2}}\sum_{G}\alpha_b(k+G)e^{i(k+G)r} \tag{3.18}$$

The factor α determines the shape of the Compton profile. The non-diagonal elements of occupation number density determines the mixing of different bands due to electron-electron interaction. The Bloch electrons are assumed to be independent scattering particles so non-diagonal elements vanish and diagonal elements representing Brillouin zone k-space of different bands represent the Fermi surface. The Compton profile of solid state electrons is determined by the occupation number density and shape of Fermi surface or Brillouin zone without non-diagonal elements. The higher momentum components also produce discontinuities for the first derivative.

3.1.6 Cold Smearing

Temperature formulation introduces systematic errors. Thus, a smearing function is required. The expression of entropy in a power series has been denoted in the previous chapter and by choosing $\tilde{\delta}(x)$ as a Dirac delta in Hermite polynomial

$$\delta(x)=\sum_{n=0}^{N} A_n H_{2n}(x) e^{-x^2} \tag{3.19}$$

where

$$A_n=(-1)^n n!4^n \sqrt{\pi}; H_o(x)=1; H_1(x)=2x; H_{n+1}=2xH_n(x)-2nH_{n-1}(x) \tag{3.20}$$

which gives the Methfessel-Paxton broadening (Methfessel et al., 1989). The Marzari-Vanderbilt broadening however constrains the occupation numbers to be positive. The broadening function is a Gaussian term multiplied by a polynomial satisfying the constraints

$$\begin{array}{lcl} \int_{-\infty}^{\infty} \tilde{\delta}(x)\,dx=1 & \rightarrow & normalization \\ \int_{-\infty}^{\infty} x\tilde{\delta}(x)dx=0 & \rightarrow & S(0)=0 \\ \int_{-\infty}^{\infty} x^2\tilde{\delta}(x)\,dx=0 & \rightarrow & Cold\,smearing \\ \int_{-\infty}^{\infty} \tilde{\delta}(x)\geqslant 0 & \rightarrow & positive\,occupancies \end{array} \tag{3.21}$$

The third term is the cold smearing broadening term which is obtained from a third order polynomial

$$\hat{\delta}(x)=\frac{1}{\sqrt{\pi}}(x^3-x^2-\frac{3}{2}ax+\frac{3}{2})e^{-x^2} \tag{3.22}$$

In Table A.4 (Appendix) we define the smearing parameters. The broadening is not based on Fermi-Dirac statistics, and **tsmear** is only a convergence parameter.

3.1.7 Band Structure and PDOS

In this section we discuss the parameters used in an ABINIT calculation to obtain the band structure and partial density of states (DOS). After an earlier self-consistent cycle calculation is performed, the density (DEN) file produced from this calculation will be used by a calculation which initializes **iscf**=-2 and **getden**=-1. The option **kssform**=3 is used to create a single Kohn-Sham states (KSS) file (double precision) containing complete information on the Kohn Sham Structure (eigenstates and the pseudopotentials used) which will be generated using the conjugate gradient algorithm. **nbdbuf** and **nbandkss** concern the details of the KSS file. The number initialized to nbandkss is the number of eigenstates in the KSS file. This number of states is forced to be the same for all k-points. The precision of the KSS file can be tuned through the input variable kssform. The constructed KSS file will be used to construct the screening calculation. The actual construction of the band structure requires information from these parameters but are presented by the parameters kptopt, **ndivk** and **kptbounds**. The negative absolute value of kptopt gives the number of segments of the band structure. The construction of the partial density of states (PDOS) is determined by the parameters **natsph, ratsph, iatsph** and **prtdos** and it was first introduced in (Christensen, 1978)**.** The advantage of using charge partitioning schemes comes from the fact that the sum of atomic DOS, for all angular momenta and atoms, integrated on the energy range of the occupied states, gives back the total charge. If this is not an issue, one could rely on the half of the nearest-neighbour distances, or any scheme that allows to define an atomic radius. Note that the choice of this radius is however critical for the balance between the s, p and d components. Indeed, the integrated charge within a given radius, behave as a different power of the radius, for the different channels s, p, d. At the limit of very small radii, the s component dominates the charge contained in the sphere. If prtdos=3, the DOS inside a sphere centered on some atom is delivered, as well as the angular-momentum projected (l=0,1,2,3,4) DOS in the same sphere. However, three additional input variables might be provided, describing the atoms that are the center of the sphere (input variables natsph and iatsph), as well as the radius of this sphere (input variable ratsph).

3.2 Excited State Calculation

In ABINIT, the ground state calculations which are described in the previous section will result in a density file and a Kohn-Sham states file which is obtained from a non-self consistent calculation. With these two files, we can then proceed to perform two types of calculations to finally obtain excited states via the GW Approximation. The first being the screening calculation and the second being the self-energy or self-energy calculation which are described in this section. However, this methodology has been known for pathologies (Jiang et al., 2010). Initial band ordering and hybrid functionals give unphysical band ordering (Lany, 2013). This is due to RPA underestimating dielectric constants and overestimates band gap energies (Lany, 2013). We finally end the section by describing how the quasiparticle renormalization factor is obtained.

3.2.1 Screening Calculation

In this section, we have highlighted the main results from (Adler, 1962; Wiser, 1963). Also relevant are the reviews by (Aryasetiawan et al., 1994; Onodera, 1973) The basic ingredients needed to perform both a screening and a self-energy calculation are the so-called oscillator matrix elements which can be evaluated by performing a fast Fourier transform (FFT) and is given by

$$\begin{aligned} M_G^{b_1 b_2}(k,q) &= \langle k-q, b_1 | e^{i(q+G).r} | k, b_2 \rangle \\ &= \sum_{G'} U^{\dagger}_{k-qb_1}(G')\, U_{kb_2}(G+G') \end{aligned} \tag{3.23}$$

The calculation of the oscillator matrix elements consists of firstly performing an FFT of the KS wavefunction from momentum space to real space, rotating the real space orbitals to obtain k-points in full Brillouin zone, computing the wavefunction product and FFT this product to finally obtain the matrix elements. With the oscillator matrix elements, we can construct the irreducible polarizability which is given by

$$\begin{aligned} &\chi^{o}_{G_1 G_2}(q,\omega) = \frac{2}{v} \sum_{k}^{BZ} \sum_{cv} M^{cv}_{G_1} [M^{cv}_{G_2}]^{\dagger} \\ &\left\{ \frac{1}{\omega + \epsilon_{ck-q} - \epsilon_{vk} - i\eta} - \frac{1}{\omega - \epsilon_{ck-q} + \epsilon_{vk} + i\eta} \right\} \end{aligned} \tag{3.24}$$

As per constructs of the Kohn-Sham Hamiltonian, only transitions between valence and conduction states contribute. The q-points in the screening matrix is obtained from all possible differences between two crystalline momenta of the wavefunctions stored in the KSS file thus determined by k-point grid from an irreducible Brillouin zone. The microscopic dielectric function is related to the irreducible polarizability by

$$\epsilon_{G_1 G_2} = \delta_{G_1 G_2} - v(q, G_1)\, \chi_{G_1 G_2}(q,\omega) \tag{3.25}$$

Therefore, the dynamically screened interaction can be written in reciprocal space as

$$W_{GG'}(q,\omega)=\frac{4\pi}{|q+G|}\epsilon_{GG'}^{-1}(q,\omega)\frac{1}{|q+G|} \tag{3.26}$$

where the dielectric matrix can be obtained from random phase approximation (RPA)

$$\begin{gathered}\hat{\epsilon}_{GG'}(q,\omega)=\delta_{(GG')}-\frac{8\pi}{|q+G||q+G'|}\sum_{vck}M_G^{vc}(k,q)M_{G'}^{vc}(k,q)\\ \{\frac{1}{\omega-\epsilon_v(k-q)-\epsilon_c(k)-i\delta}-\frac{1}{\omega-\epsilon_v(k-q)-\epsilon_c(k)+i\delta}\}\end{gathered} \tag{3.27}$$

where

$$M_G^{nm}(k,q)=\langle\Psi_{k-qn}|e^{-i(q+G)r}|\Psi_{km}\rangle \tag{3.28}$$

For imaginary frequencies we ignore the broadening factor $i\delta$

$$\begin{gathered}\hat{\epsilon}_{GG'}(q,\omega)=\delta_{(GG')}-\frac{8\pi}{|q+G||q+G'|}\sum_{k\in BZ}\sum_{vc}\sum_{R\in Gq}M_G^{vc}(k,q)M_{G'}^{vc}(k,q)\\ \{\frac{1}{i\omega-\epsilon_v(k-q)-\epsilon_c(k)}-\frac{1}{i\omega-\epsilon_v(k-q)-\epsilon_c(k)}\}\end{gathered} \tag{3.29}$$

In the case of screening calculations, **irdkss** will firstly read the KSS file from a non-SCF calculation. The number of G vectors is defined by ecuteps, while **ecutsigx** defined the number of G used in self-energy calculations. In principle the integrand function to obtain χ_o should be evaluated for each k-point in the Brillouin zone (BZ), however it is possible to reduce the number of points to be explicitly considered by taking advantage of symmetry properties. In reciprocal space, this is given by a convolution in which the number of reciprocal lattice vectors employed to describe the wavefunctions is given by ecutwfn. As is shown in Table A.6 (Appendix), **ecutwfn** is smaller than ecut, so that the wavefunctions are filtered, and some components are ignored. As a side effect, the wavefunctions are no more normalized, and also, no more orthogonal. A value of **ecuteps** between 5 and 10 Hartree often leads to converged results (at the level of 0.01 eV for the energy gap). There are other options which ABINIT can initialize for the variable **gwcalctyp** such as a Hartree-Fock (Galamić-Mulaomerović et al., 2005), Screened Exchange (von Barth et al., 1972), COHSEX (Hedin, 1965; Hedin et al., 1970) , model GW (Faleev et al., 2004; Gygi et al., 1997), HSE06 (Heyd et al., 2003), PBE0 (Adamo et al., 1999) and B3LYP (Bruneval, 2009) in both 1-shot and self-consistent calculations (von Barth et al., 1996; Holm et al., 1998) respectively. Higher levels of self-consistency both on G and W reduces level of correlation and increases discontinuity and renormalization factor (Olevano et al., 2012). **freqremax, freqremin** and **nfreqre** define the spacing of the frequency mesh along the real axis. **symchi, awtr, fftgw** and **gwmem** are responsible for improving the efficiency for the screening calculation. With these results, we can obtain spectra for the loss function and dielectric function in Equations 2.40 and 2.70.

3.2.2 Self-energy Calculation and Spectral Function

The screened interaction is separated into static bare Coulomb term and frequency dependent contributions

$$W = v + (\epsilon^{-1} - 1)v \tag{3.30}$$

Taking W into Σ splits the self-energy into

$$\Sigma(r_{1,} r_2 ; \omega) = \Sigma_x(r_1, r_2) + \Sigma_c(r_1, r_2 ; \omega) \tag{3.31}$$

The exchange self-energy is a static term and has the same term as the Fock operators

$$\Sigma_x(r_1,r_2) = -\sum_{k}^{BZ}\sum_{v}^{occ}\Psi_{nk}(r_1)\Psi_{nk}^{\dagger}(r_2)v(r_1,r_2) \tag{3.32}$$

The diagonal matrix elements of the exchange part are given by

$$\langle b,k|\Sigma_x|b,k\rangle = -\frac{4\pi}{V}\sum_{v}^{occ}\sum_{q}^{BZ}\sum_{G}\frac{|(M_G^{b_1b_1}(k,q))|^2}{|(q+G)|^2} \tag{3.33}$$

Due to the long range nature of the bare Coulomb interaction, convergence with respect to number of planewaves used in oscillators is slow. Convergence for correlation is faster as it is a short range term.

The matrix elements of the correlation part are given by

$$\begin{aligned}&\langle b,k|\Sigma_c|b,k\rangle\\ &= \frac{i}{2\pi V}\sum_{q}^{BZ}\sum_{G_1G_2}\sum_{n=1}^{\infty}(M_{G_1}^{nb_1}(k,q))^{\dagger}(M_{G_2}^{nb_2}(k,q))v_{(G_1G_2)}(q)J_{(G_1G_2)}^{(nk-q)}(q,\omega)\end{aligned} \tag{3.34}$$

The calculation of dynamical effects are placed in the *J* term. ABINIT offers either the plasmon-pole or contour deformation technique to obtain *J*. Lebègue et al. (2003) has defined these matrix elements as

$$\langle\Psi_{kn}|\Sigma_c|\Psi_{kn}\rangle = \frac{1}{\Omega}\sum_{q}\sum_{GG'}\sum_{m}M_G^{mn}(k,q)M_{G'}^{mn}(k,q)C_{GG'}^{M}(k,q,\omega) \tag{3.35}$$

where

$$C_{GG'}^{M}(k,q,\omega) = \frac{i}{2\pi}\int d\omega'\frac{W_{GG'}^{C}(q,\omega')}{\omega+\omega'-\epsilon_m(k-q)+i\delta sgn[\epsilon_m(k-q)-\mu]} \tag{3.36}$$

where $W^c = \omega - v$. The contour integral is performed on the imaginary axis as W^c is well behaved on this axis. This deformation also allows contributions from the poles of the Green's functions

$$C^{M}_{GG'}(k,q,\omega)=\frac{-1}{\pi}\int_{0}^{\infty} d\omega'' W^{C}_{GG'}(q,i\omega'')\frac{\omega-\epsilon_n(k-q)}{[\omega-\epsilon_n(k-q)]^2+\omega''^2}$$
$$\pm W^{C}_{GG'}(q+(\omega-\epsilon_n(k-q)))\Theta\{\pm(\omega-\epsilon_n(k-q))\}\Theta\{\pm(\omega-\mu)\}\Theta\{\pm(\epsilon_n(k-q)-\mu)\}$$

(3.37)

This technique is proposed to avoid dealing with quantities close to the real axis whereby the integral over real axis is transformed into integral over contour. Real axis integration is suitable for integrating momentum distribution far from the Fermi momentum while imaginary axis integration is accurate near the discontinuity (Olevano et al., 2012).

Spectral functions are described in terms of the orthonormal set of Bloch wave functions obtained from the Kohn-Sham eigenfunctions (Olevano et al., 2012). The imaginary part of the Green's function is the calculated spectral function. From this term, the occupation number density is given by

$$n_{b,b'}(k)=\pi^{-1}\int_{-\infty}^{\mu} I\,m G_{b,b'}(k,E)\,dE \tag{3.38}$$

where μ is the chemical potential. This relation only holds true for cases where the spectral function is diagonal for *b* and *b'*, and not requiring non-diagonal terms. The solution in terms of the Green's function can be written as

$$G_{b,b'}(k,E)=[E-E_{b,k}-\Sigma_{b,k}(E)]^{-1}_{b,b'} \tag{3.39}$$

The integral represents the correlation contribution to the momentum distribution from each band. Integrating the spectral function along the real axis gives the correlation contribution to evaluate the momentum distribution. The value of the correlation contribution can be obtained graphically by choosing the cumulant with the Fermi energy.

In Table A.7 (Appendix), we define the parameters used in our self-energy calculation. The algorithm implemented by **symsigma** constructs a symmetric invariant for the diagonal matrix elements of the self-energy by simply averaging the GW results within the degenerate subspace. Usually, **ecutwfn** is smaller than ecut, so that the wavefunctions are filtered, and some components are ignored. As a side effect, the wavefunctions are no more normalized, and also, no more orthogonal. Also, the set of plane waves can be much smaller for a screening calculation, than for a self-energy calculation, although a convergence study is needed to choose correctly both values. When gwcalctyp=2, the quasiparticle wavefunctions are computed and represented as linear combination of some Kohn-Sham wavefunctions. True quasiparticle wavefunctions do not differ from the Kohn-Sham (KS) wavefunction in the case of the impulse approximation. To determine the quasiparticle energies by specific k-point, **nkptgw** and **kptgw** will be used. As mentioned in the previous section, kptgw will be limited the k-points sampled in the ground state calculation and no k-point interpolation will be carried out. In this case **bdgw** designates the KS wavefunctions used as basis set. For each k-point, indeed, the quasiparticle wavefunctions are expanded considering only the KS states between the first and second value intialized to bdgw. The parameters **freqspmax, freqspmin** and **nfreqsp** will determine the range of the spectral function and its resolution.

3.2.3 Quasiparticle Renormalization Factor

The exchange correlation potential is a static, local and Hermitian approximation to the self-energy. If the difference between exchange-correlation potential v_{xc} and is Σ small **(**Lebègue et al. 2003), thus treating v_{xc} with first order perturbation theory allows us to obtain a quasiparticle (QP) Hamiltonian which can be written as a perturbation of the KS Hamiltonian

$$\hat{H}^{qp}=\hat{H}^{KS}+(\Sigma-v_{xc}) \tag{3.40}$$

which gives a zeroth order approximated non-local, energy dependent self-energy

$$e^{QP}=e^{KS}+Z\langle\psi^{KS}|\Sigma(\epsilon^{KS})-V_{xc}|\psi^{KS}\rangle \tag{3.41}$$

where

$$Z=\{1-\langle\psi^{KS}|\frac{\delta\Sigma}{\delta(\epsilon^{KS})}|\psi^{KS}\rangle\}^{-1} \tag{3.42}$$

is the renormalization factor. More specifically this allows comparison to the plasmon pole model **(**Lebègue et al. 2003) if taking the real part of the perturbation

$$\begin{gathered}\Re E_n(k)=\epsilon_n(k)\\ +Z_{nk}\langle\langle\Psi_{kn}|\langle\Re\Sigma(r,r',\epsilon_n(k))|\Psi_{kn}\rangle\rangle\rangle-\langle\langle\Psi_{kn}|\langle v_{xc}^{LDA}(r)|\Psi_{kn}\rangle\rangle\rangle\end{gathered} \tag{3.43}$$

where the renormalization factor is given by

$$Z_{nk}=1-\left\langle\Psi_{kn}\left|\frac{\delta\Re\Sigma(r,r',\epsilon_n(k))}{\delta\omega}\right|\Psi_{kn}\right\rangle \tag{3.44}$$

This term allows to put the discontinuity of the momentum density in quantitative terms. The quasiparticle renormalization factor is related to the size of the jump at the Fermi break and strength of electron-electron correlation (Soininen et al., 2001; Huotari et al., 2010). In this term, the self-energy contains electron-electron and electron phonon effects. The renormalization factor reduces with decreasing electron density as correlations build up.

3.3 Compton Profile Work Flows

In this final section, we discuss several subroutines we have used to obtain the band structures, spectral functions and momentum densities for our calculations. We finally discuss how we convert the momentum density to obtain the Compton profile.

3.3.1 Implementation of SIG

In a GWA calculation via ABINIT, the end result is two files of interest which are the Sigma file which is based on Equation (2.18) and the Quasiparticle Energies (QP) file which is based on Equation (2.14). A Sigma file will contain a full or partial list of k-points. Thus, our first step requires to either break each constituent spectral data into their respective k-points or reconstruct a set of spectra based on a chosen set of k-points. Breaking the Sigma file requires the subroutine which is essentially

Subroutine 1

```
num=$(( `sed '/b/d' $SIGfile | sed '/k/d' | wc -l` / `grep k $SIGfile | wc -l` ))
grep k "$SIGfile" | awk -v var=$SIGfile -v numlines=$num '{ printf("grep -A %d k =
%f  %f  %f %s > k.%.3f,%.3f,%.3f\n",numlines,$4,$5,$6,var,$4,$5,$6)}
```

Here, the number of lines for each k-point are counted and placed in the variable num. These lines will then be extracted and placed in files starting with “k.” To reconstruct the spectra along an arbitrary chosen set of k-points, we firstly need to use the interface subroutine which will print out the k-points available in the database and allow the user to input a chosen set of k-points from the database. This subroutine is essentially

Subroutine 2

```
ls -l k* | sed 's/^-.*k.//g' | sed 's/,/ /g'

read array[$i]

echo  ${array[$i]} >> plsmerge.txt
```

We then employ this subroutine to reconstruct our chosen spectra

Subroutine 3

```
awk '{printf("k.%.3f,%.3f,%.3f\n",$1,$2,$3)}' plsmerge.txt | sed "s/^/cat /g" | sed "s/$/

>> kpath

awk -v col=$i '{printf(“%c\t”,$col)}' kpath > SpecFunc
```

Besides the spectra, the Sigma file contains information on the Re Σ and Im Σ as well. Users thus have 3 profiles that they can choose from. If the user chooses spectral function, all spectral data will be placed into file 'SpecFunc'. The code will then determine if the calculation is spin dependent, the number of bands, number of k-points and number of frequencies in the calculation. With these values, the spectral function from the above mentioned SpecFunc file can be organized into the respective bands which allows users to select spectra from the bands of their choice. The code will then proceed to obtain the cumulant of these spectra. Finally, the code will transpose these cumulants with respect to distance of k-point from the origin. The user will then be prompt for the Fermi energy which can be obtained from a plasmon-pole model calculation. The plot obtained at this energy represents the momentum distribution of the chosen band.

The QP energies are required to determine the Fermi break in the momentum distribution. This can be obtained by having a second order fit of the band below the

Fermi energy. We have included this functionality which also allows the user to compare quasiparticle bands and ground state energy bands with one another. Similar to the case of the Sigma file, a user can choose to break a QP file or reconstruct a QP band structure against a ground state (GS) band structure. This means that the GW energies will be broken into its respective k-points and reconstructed again. As, the formatting of the ABINIT output files are similar, we will call Subroutine 1 to break the QP file. To construct the corresponding ground state energies however, a non-self consistent ground state calculation has to be performed with ABINIT and passed into this subroutine

Subroutine 4

```
var=`grep " kpt#    $i" $gwnscffile | tail -1 | awk '{printf("sgk.%.3f,%.3f,%.3f",
$8,$9,$10)}'`
grep -A 4 " kpt#   $i" $gwnscffile | sed '/^ kpt#.*$/d' | sed 's/^  //g' | sed 's/  /\n/g' | sed
'/--/d' > $var
```

To reconstruct the energies subroutine 2 is called again. The code will then obtain the ground state and quasiparticle k-points, energies and number of bands. The final step consists of indexing the energies of the ground state and quasiparticle energies by the respective k-points.

3.3.2 Reconstruction of Compton Profile from Momentum Density

The momentum distribution obtained with the above subroutines will then be transformed to the Compton profile via the steps described in this section. We firstly multiply the values of the momentum density with the momenta. The cumulant of these values gives the Compton profile as described in Equation (2.51) in Chapter 2. Using this theoretical Compton profile, we then used Mathematica to perform a Gaussian convolution to compare with the experimental result. For this convolution, its zeropadding and magnitude normalization is set to the smallest difference between the theoretical profile and experiment.

3.4 Computational Details

We finally discuss the computational details behind the three sections in Chapter 4.

3.4.1 NiO and TiO_2

We have performed two studies on the Compton profile of crystalline NiO and TiO_2. For NiO, we have initialized a rock-salt structure with lattice parameter given by 4.1684 Å. We have chosen a k-point grid of 20x20x20 which amounts to 256 k-points. For the ground state calculation we have initialized the plane wave kinetic energy cutoff as 2721 eV with a tolerance at 10^{-12} eV over 30 bands. The plane wave kinetic energy cutoff controls the number of plane waves at a given k-point while the tolerance will cause the self-consistent cycle to stop when the absolute differences between total energy is reached twice successfully. We have used the cold smearing technique to take into account the occupation of the electrons in the d-orbitals. The converged total energy is reached after 15 iterations. For the excited state calculations, we have used the contour deformation technique to obtain the spectral function. To construct the dielectric matrix, we have initialized 60 imaginary and real frequency points using frequencies in the range of -40.8 eV to 40.8 eV and 0.5 eV to 166.2 eV respectively. Its plane wave kinetic energy cutoff is set at 2721 eV with a tolerance at 10^{-12} eV and a polarizability cutoff at 270 eV over 30 bands with 20 unoccupied bands. In the excited state case, the plane wave kinetic energy cutoff determines the cut-off energy of the planewave set used to represent the wavefunctions in the formula that generates the independent-particle susceptibility while the polarizability cutoff determines the cut-off energy of the planewave set used to represent the independent-particle susceptibility. Obtaining the dielectric matrix, we can then obtain the self-energy term in which we have set the plane wave kinetic energy cutoff as 2721 eV and the spectral function consists of 1600 data points in the range between -13 to 13 eV. To check for the convergence of the excited state calculations, we have performed the routines recommended by ABINIT whereby an initial screening calculation will be used to determine the converged plane wave kinetic energy cutoff with respect to the self-energy term. With this converged term, we would then proceed to determine the converged number of bands with respect to the self-energy term. With these two terms, we can then proceed to determine the converged plane wave kinetic energy cutoff, number of bands and polarizability cutoff sequentially, with respect to the dielectric matrices which would then be checked for convergence with respect to the self-energy. Even though the size of the Monkhorst-Pack grid is 256 k-points, ABINIT only allows k-points taken from this grid to undergo contour deformation calculations. We have thus chosen two directions to construct the momentum distributions, specifically [110] with 11 k-points and [100] with 11 k-points. For TiO_2, we have initialized a rutile structure with lattice parameters 4.5888 Å-4.5888 Å-2.9576 Å. As the rutile structure requires more atoms compared to the rock-salt structure, we have chosen 2 Monkhorst-Pack grids with the size of 10x10x10 and 11x11x11. For the ground state calculation, the plane wave kinetic energy cutoff is 2993 eV with a tolerance at 10^{-9} eV over 30 bands. Convergence is achieved after 13 iterations respectively. For both NiO and TiO_2, we have used the Troullier-Martins pseudopotential with the highest angular momentum of 2 in this calculation. For the excited state calculation we have constructed the dielectric matrix out of 60 imaginary and real frequency points using frequencies in the range of 0 eV to 27.2 eV and 0.5 eV to 158 eV respectively. We finally constructed the self-energy calculation with a plane wave kinetic energy cutoff of 2993 eV with a polarizability cutoff of 270 eV. The spectral function is constructed from 1600 frequency points in the range of -5.17 eV to 5.17 eV. We have sampled 11 k-points along the directions [100] and [111] respectively. The calculations were conducted as a spin polarized antiferromagnetic system and found that there is no significant difference between spin up or spin down spectral functions.

3.4.2 NiO, CoO and FeO

We have performed three studies on the Compton profile of crystalline NiO, CoO and FeO. We have respectively initialized a rock-salt structure with lattice parameters given by 4.1684 Å, 4.2667 Å and 4.303 Å. In order to increase the sample size, we have performed integrations over 5 Monkhorst-Pack grids. The grids we chose are 9x9x9,-18x6x-18,-13x13x-13,-14x14x-14 and -15x15x-15. Its number of k-points are 110, 120, 84, 104 and 120 respectively. We have found that the ground state energies and excited state energies for each of these grids at the Γ point is consistent to three and two decimal places respectively if initalized with the following parameters. For the ground state calculation we have initialized the plane wave kinetic energy cutoff as 1700 eV with a tolerance at 10^{-12} eV over 30 bands. Calculations of 3d and 4f systems require a large number of plane waves to describe localized 3d and 4f states. We have used the cold smearing technique to take into account the occupation of the electrons in the d-orbitals. The k-point grids as mentioned above converged after 27, 23, 25, 25 and 22 self consistent iterations respectively. For the excited state calculations, we have used the contour deformation technique to obtain the spectral function. To construct the dielectric matrix, we have initialized 30 imaginary and real frequency points using frequencies in the range of of 0 eV to 27 eV and 3.3 eV to 133 eV. Its plane wave kinetic energy cutoff is set at 1700 eV with a tolerance at 10^{-12} eV and a polarizability cutoff at 270 eV over 30 bands with 20 unoccupied bands. Obtaining the dielectric matrix, we can then obtain the self-energy term in which we have set the plane wave kinetic energy cutoff as 1700 eV and the spectral function consists of 1600 data points in the range between -13 to 13 eV. Even though the size of the Monkhorst-Pack grid was in the range of 80 to 120 k-points, ABINIT only allows k-points taken from this grid to undergo contour deformation calculations. We have thus chosen three directions to construct the momentum distributions, specifically $[\bar{1}0\bar{1}]$ with 30 k-points, $[00\bar{1}]$ with 21 k-points and $[10\bar{1}]$ with 36 k-points.

3.4.3 ZnSe

We have calculated the Compton profile of crystalline ZnSe which has a metastable zincblende structure which is optically isotropic and the wurtzite structure is optically anisotropic with c as the polar axis (Oshkiri et al., 1999; Fleszar et al., 2004). We have initialized a zinc-blende structure with lattice parameters given by 5.6676 Å. We have initialized a k-point grid of 16x16x16 to sample the k-points. For the ground state calculation we have initialized the plane wave kinetic energy as 2175 eV with a cutoff at 10^{-9} eV over 75 bands. The plane wave kinetic energy cutoff controls the number of plane waves at a given k-point while the tolerance will cause the self-consistent cycle to stop when the absolute differences between total energy is reached twice successfully. We have used the cold smearing technique to take into account the occupation of the electrons in the d-orbitals. The k-point grids as mentioned above converged after 10 self consistent iterations respectively. For the excited state calculations, we have used the contour deformation technique to obtain the spectral function. To construct the dielectric matrix, we have initialized 30 imaginary and real frequency points between energies of 10 eV to -10 eV. Its plane wave kinetic energy cutoff is set at 2175 eV with a tolerance at 10^{-9} eV and a polarizability cutoff at 270 eV over 15 bands with 60 unoccupied bands. In the excited state case, the plane wave kinetic energy cutoff determines the cut-off energy of the planewave set used to represent the wavefunctions in the formula that generates the independent-particle susceptibility while the polarizability cutoff determines the cut-off energy of the planewave set used to represent the independent-particle susceptibility. Obtaining the dielectric matrix, we can then obtain the self-energy term in which we have set the plane wave kinetic energy cutoff as 2175 eV and the spectral function consists of 1600 data points in the range between -13 to 13 eV. To check for the convergence of the excited state calculations, we have performed the routines recommended by ABINIT whereby an initial screening calculation will be used to determine the converged plane wave kinetic energy cutoff with respect to the self-energy term. With this converged term, we would then proceed to determine the converged number of bands with respect to the self-energy term. With these two terms, we can then proceed to determine the converged plane wave kinetic energy cutoff, number of bands and polarizability cutoff sequentially, with respect to the dielectric matrices which would then be checked for convergence with respect to the self-energy. ABINIT only allows k-points taken from the 16x16x16 k-point grid to undergo contour deformation calculations. We have thus chosen two directions to construct the momentum distributions, specifically in the direction[110] and [100] with 11 k-points respectively. We have used the Troullier-Martins pseudopotential with a highest angular momentum of 2 in this calculation indicating that the d-orbital is included in the valence. Previous calculations assumed the 3d orbitals to be in core states because to avoid using large plane wave basis sets (Oshkiri et al., 1999;Zakharov et al., 1994). When treating semicore d-states, the choice of basis sets and convergence is important (Luo et al., 2002). Strong hybridization between semicore states and valence states result in larger nondiagonal matrix elements not accounted for causing lower 3d semicore binding energies compared to experimental values (Oshkiri et al., 1999).

CHAPTER 4 : RESULTS AND DISCUSSION

In this chapter, we show the effects of a self-energy correction on the late TMOs, TiO_2 and ZnSe. These effects are studied by observing the smearing of the occupational number before and after the Fermi break and relating it to the clustering of broadened spectral functions for the valence bands.

4.1 NiO and TiO_2

In this section, we firstly calculated the excited state and ground state band structure calculations for NiO and TiO_2. We have applied a scissor operator to shift the energies of the G point as well as the 4 k-points to the left and right of G by 4.3 eV in the case of NiO and 3.0 eV in the case of TiO_2. We then calculated the Fermi energy and Fermi momenta which will be subsequently used to obtain the spectral functions. Our spectral functions for NiO are broadened and contains shoulder similar to what has been observed in earlier studies. This is in contrast to TiO_2 which does not have broadened spectra. These functions will be used to obtain the momentum density. We explain the shape of the momentum density of NiO in terms of the cumulant functions which are obtained from broadened spectral functions as oppose to TiO_2 which have Dirac-delta like spectral functions. We then compared and explained the differences between GW Approximation and ground state momentum densities. Finally we use the momentum densities to construct the Compton profile. The profiles will be analyzed in terms of difference profiles and anisotropy. We end this section by discussing the quasiparticle renormalization factor (QPRF).

4.1.1 Band Energies

We firstly compare the calculated ground state band gaps with the excited state band gaps in Table 4.1 for NiO. At the positions of the high symmetry *k*-points *X* (0.5,0.0,0.0) and *L* (0.5,0.5,0.0), the application of the GWA seems to play its role in increasing the band gap compared to the ground state calculation. Approaching the *G* point however the agreement between band gaps seems to deteriorate in the case of GWA. The agreement near the *X* and *L* *k*-points is due to the well known effectiveness of the GWA in handling valence *p*-orbitals from the O atom (Aulbur et. al., 1999).

Table 4.1: NiO band gaps for *k*-points of interest.

Band gaps with points of interest									
	***k*-points**		**E^0_gap**	**E^GW_gap**		***k*-points**		**E^0_gap**	**E^GW_gap**
0	0	0	3.444	0.253	0	0	0	3.444	0.253
0.05	0	0	3.471	1.058	0.05	0.05	0	3.39	1.267
0.1	0	0	3.581	1.998	0.1	0.1	0	3.653	2.583
0.15	0	0	3.783	2.69	0.15	0.15	0	4.304	3.409
0.2	0	0	4.028	3.272	0.2	0.2	0	5.131	4.381
0.25	0	0	1.319	0.927	0.25	0.25	0	5.947	5.257
0.3	0	0	1.537	1.248	0.3	0.3	0	6.601	5.909
0.35	0	0	1.693	1.636	0.35	0.35	0	6.975	6.313
0.4	0	0	1.79	1.46	0.4	0.4	0	7.08	6.455
0.45	0	0	1.839	2.271	0.45	0.45	0	7.076	6.349
0.5	0	0	1.854	2.387	0.5	0.5	0	7.053	6.704
E^0_gap	Ground state band gap								
E^GW_gap	Excited state band gap								

We next compare the calculated ground state band gaps with excited state band gaps in Table 4.2 for TiO_2. In the direction [100], we observe that the GWA band gaps are generally smaller than that ground state calculation band gaps. This is due to this direction mainly populated by Ti atoms with *d*-orbital valence energies. In the case of the direction [110], agreement is better in the high symmetry *k*-point *L* (0.5,0.5,0.0). However, in the direction [111], the GWA band gaps are seen to be larger than the ground state band gaps. In these two directions, there is a strong contribution from both the Ti and O atoms. The disagreement in band gap mainly lies with the origin which mainly has the largest contribution from the Ti *d*-orbital with smaller contributions from *p*-orbitals of Ti and O.

Table 4.2: TiO_2 band gaps for k-points of interest.

Band gaps with points of interest													
K-points			**LDA**	**GWA**	***k*-points**			**LDA**	**GWA**	***k*-points**			**LDA**
0	0	0	3.115	1.667	0	0	0	3.12	1.595	0	0	0	3.115
0.091	0	0	3.022	1.745	0.091	0.091	0	2.893	1.873	0.091	0.091	0.091	2.242
0.1	0	0	3.001	1.833	0.1	0.1	0	2.855	1.939	0.1	0.1	0.1	2.217
0.182	0	0	2.862	1.823	0.182	0.182	0	2.659	1.676	0.182	0.182	0.182	3.607
0.2	0	0	2.829	1.908	0.2	0.2	0	2.641	1.727	0.2	0.2	0.2	4.243
0.273	0	0	2.742	1.748	0.273	0.273	0	2.712	1.677	0.273	0.273	0.273	5.163
0.3	0	0	2.714	1.826	0.3	0.3	0	2.781	1.854	0.3	0.3	0.3	5.233
0.364	0	0	2.684	1.701	0.364	0.364	0	3.041	1.957	0.364	0.364	0.364	4.987
0.4	0	0	2.675	1.788	0.4	0.4	0	3.216	2.095	0.4	0.4	0.4	4.908
0.455	0	0	2.694	1.721	0.455	0.455	0	3.47	2.07	0.455	0.455	0.455	4.594
0.5	0	0	2.721	1.848	0.5	0.5	0	3.531	3.349	0.5	0.5	0.5	4.515

Table 4.3: Previous reports of GWA and experimental band gaps for NiO and TiO_2.

	Previous GWA Band gaps (eV)	**Experiment (eV)**
NiO	3.75(Jiang et al., 2010), 4.8(Gonze., 2005), 5.5(Aryasetiawan et al., 1995), 3.7(Massida et al., 1997),2.4(Li et al., 2005),3.6 (Ye et al., 2010)	4.3(Sawatzky et al., 1984), (Fujimori et al., 1984), 4.0(Hufner et al., 1984)
TiO_2	3.59(Chiodo et al., 2010) , 3.78(van Schilfgaarde et al., 2006), 3.13(Malashevich et al., 2014), 3.40(Patrick et al., 2012)	3.3(Tezuka et al., 1994),3.6(Rangan et. al., 2009)

The shortcomings in straightforward GWA calculations on these TMOs and improvements by including other methods to the GWA calculations such as model GW, GWA+U, self-consistent GW and HSE have been previously reported. In their study of GWA+U of TMOs, Jiang (Jiang et al.,2010) observed that an increase in *U* affects the gaps nonlinearly due to the *p-d* hybridization conteracting the scissor operator. By applying the term *U* with GWA, they remark that energies can be improved to be better than DMFT (Georges et al., 1996). In their study of GWA for NiO, Aryasetiawan (Aryasetiawan et al., 1995) employed a nonlocal rigid shift to raise and reduce the width of Ni unoccupied e_g bands. The self-energy increases the LDA's gap to 1 eV. This band gap is seen to be very large if compared to HF, as no screening is implemented. Massida (Massida et al., 1997) firstly observed that LSDA is unable to describe localized nature of electron states and produces vanishing band gaps. By initializing a model GW, depletion of charge density in Ni and an increase in charge density in O is observed. This causes an upward shift of unoccupied *d* bands by 2.5 eV from GGA to GWA gives a bandgap of 4.2 eV. Rodl (Rodl et al., 2009) has explained that the smaller energy gaps in GWA is due to failure of the perturbational treatment of the quasiparticle equation. We show the band gaps from these studies in Table 4.3. Based on this comparison we have calculated our ground state band gap to be 3.444±2.721 eV and 3.115±0.578 eV while the excited state band gap to be 0.253±4.247 eV and 1.667±1.807 eV for NiO and TiO_2 respectively.

Our band gaps at the *G* points are clearly much smaller compared to previously performed calculations. These band gaps are dependent on the number of initialized k-points in the calculation as shown in Table 4.4. In the case of NiO, the initialization of a 20x20x20 *k*-point grid thus seems inadequate to increase the band gap at the G point where the Ni-*d* orbital valence electrons are situated as is initialized in the reduced coordinates. An increase of say a 40x40x40 *k*-points will improve the resolution of the k-point sampling by 0.025 a.u. However, this calculation would double the memory requirements from the current calculation which is 20 GB of RAM with a screening input file of 13 GB and a Kohn-Sham states file of 2 GB.

Table 4.4: An increase in size of k-point grid improves band gap value

***k*-point grid**	**Number of *k*-points**	**Band gap, eV**
5x5x5	10	-0.1315
10x10x10	47	0.079
15x15x15	120	0.1605

In a similar fashion as previous works, we thus opt to use the so called scissor operator to obtain a proper band gap for the case of GWA as has been suggested in previous works of excited state calculations of NiO (Sharma et al., 2011; Yan et al., 2013). We shift the energies of the G point as well as the 4 k-points to the left and right of the *G* by 4.3 eV (Rodl et al.,2009). This equates to the experimental band gap at the *G* point and places the valence band maximum at the *G* point with a parabolic shape (Massida et al.,1997). We present the scissor shifted band structure in Figure 4.1 (top).

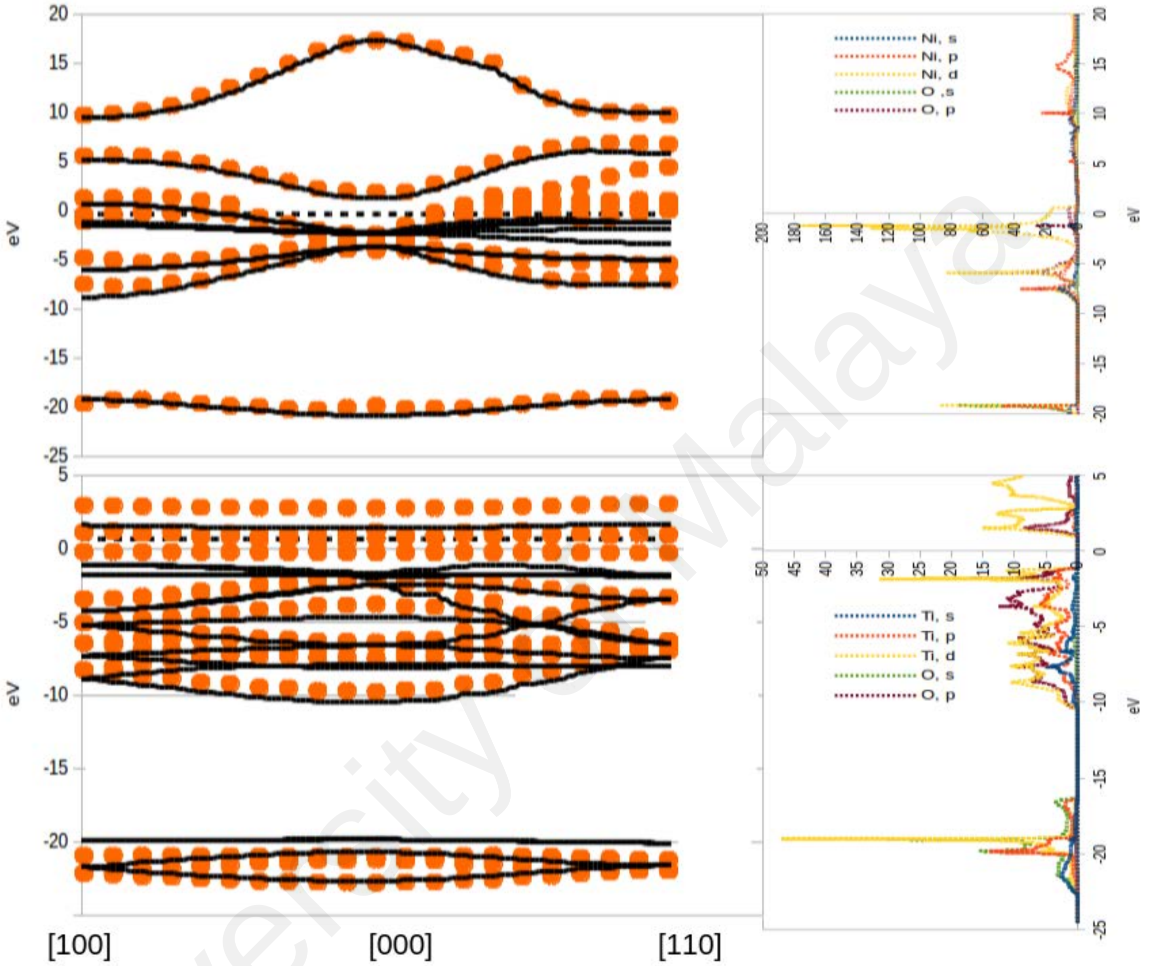

Figure 4.1: NiO (above) and TiO_2 (below) excited state (orange) and ground state (black) bandstructure and partial density of states.

As is indicated by the partial density of states in the ground state case, the largest contribution to the the valence band energy is the transition metal (TM) 3*d* orbital and a small contribution of the O 2*p* orbital. Similarly to previous observations by Rodl (Rodl et al., 2009), we observe that these bands are strongly localized with little dispersion. In that work, the functional HSE03 reduces the shifts of the O 2*p* quasiparticle valence bands and mostly affects *d*-states. Jiang (Jiang et al., 2010) observed that narrowing of valence bandwidth is due to GW energies pushing down localized *d*-orbitals in the occupied region and leaving *p*-orbital occupation. However in studies related to GWA+U, Das (Das et al., 2015) claims that increasing the Hubbard *U* term is seen to significantly increase O 2*p* character in highest valence band states thus becoming more delocalized. Here, *d*-bands saturate at high *U* due to *d*-band crossing to 4*s* states (Jiang et al., 2010).

Via the GWA, these *d*-states are strongly affected by the dynamic character of screened Coulomb interaction. Thus, screening effects in GWA causes the wavefunctions in valence bands to be more localized. This term is contained in the dielectric function which describes free electron contribution and interband transition. The d-orbital corresponds to filled t_{2g} states as reported in (Rodl et al., 2009). These t_{2g} states contain majority and minority spins (Faleev et al., 2004). Our energies also agree with Massida in that the t_{2g} and O 2*p* orbitals produce no gap in the case of GWA compared to the wider gap seen in LDA. Before the application of the scissor shift, the O 2*p* and TM 3*d* energy will be raised above the Fermi level via GWA compared to the findings of Massida (Massida et al., 1997) at -3.5 eV for O 2*p* and -1.7 eV for t_{2g} and Li (Li et al.,2005) at -8 eV for O 2*p*. Thus, a straightforward GWA without scissor operator does not shift the valence band lower compared to previous studies. We can also observe the double peak valence band DOS as seen in (Rodl et al., 2009). It is thus clear that the energies under the Fermi energy in NiO are represented by the hybridization of *p* and *d*-orbitals which are central to the discussion of a strong correlation. This highlights the importance of *d*-*p* hybridization in interpreting momentum densities and the dielectric screening broadening the spectra. Above the Fermi energy, our bands agree with the observation by Massida that the GWA pushed up the e_g orbitals and causes the shifting of the delocalized 4*s* state at a lesser magnitude than the localized d states (Li et al., 2005). Rodl (Rodl et al., 2009) observed that the 3*d* e_g states are 1 eV higher in energy due to the neglect of vertex correction in the case of NiO however a strong dispersion for the Ni 4*s* character with TM 3*d* states at *G* is due to applying the GWA+HSE. We then present the TiO_2 band structure with a shift of 3.00 eV (Zhai et al., 2007) at the *G* point in Figure 4.1 (bottom). As is indicated by the partial density of states in the ground state case, the valence energies have a hybridized contribution between a larger TM *d*-orbitals, O *p*-orbitals and smaller contributions from Ti *p*-orbitals. Below the valence energy, the contribution is mainly from the O and Ti *p*-orbitals. The conduction band has contribution mainly from the Ti *d*-orbitals and O *p*-orbitals.

By obtaining the band gaps and band energies, we can now proceed to obtain the Fermi energy and Fermi momenta. We firstly obtain the excited state Fermi energies to be -0.265 eV in the case of NiO and 0.6876 eV for the case of TiO_2. This value is obtained from the middle point between the valence band energy and conduction band energy at the *G* point. We have unsuccessfully attempted to obtain the Fermi energy directly from ABINIT via the two other methods which we will describe further. The first method involves a full calculation of all k-points via the contour deformation method. This method fails to run as it is extremely computationally demanding. However this would provide the Fermi energy for the exact initializations we are performing. The second method involves an approximation to the computationally demanding contour deformation method which is the significantly less computationally demanding plasmon pole model (Godby et al., 1989). In this method, only one frequency point at 0.0 eV is used to calculate the screening and self-energy. Using this method, with the same k-point grid and other initializations as the contour deformation case the Fermi energy indicates that the conduction band is the valence band as the plasmon pole model (PPM) itself gives a negative band gap at the G point.

We then proceed to obtain the Fermi momentum or Fermi break which is used to identify the break between occupied and unoccupied momentum densities and has the unit of a.u. It is calculated by identifying the effective mass through fitting the valence band under the Fermi energy to a second order curve for all directions of interest. The second order derivative of the inverse energy is given by

$$m^* = \hbar^2 \frac{d^2 E^{-1}}{d k^2} \tag{4.1}$$

where we assume the Planck's constant to be 1. The Fermi momenta is thus given by

$$p_F = \sqrt{m^* E_F} \tag{4.2}$$

We then calculate the Fermi momenta as given by Table 4.5. For this analysis, we are only interested in the excited state bands as they will be used in our further analysis. It was previously remarked that a difference in Fermi break along various directions is an indication of distortion in the free electron sphere (Sakurai et al., 1995). This is expected as the Fermi surface of these two oxides are not spherical.

Table 4.5: Fermi momenta for NiO and TiO_2 along *k*-points of interest.

TMO	**Fermi Moments**		
	[100], p_f/a.u.	[110], p_f/a.u.	[111], p_f/a.u.
NiO	0.2022	0.3323	
TiO_2	0.3243	0.2466	0.7896

4.1.2 Spectral Function and Momentum Densities

With the knowledge of the Fermi energy and Fermi momenta, we can now proceed to obtain the spectral functions as shown in Figure 4.2. As has been performed with the band energies, we have shifted the four *k*-points from the origin by 4.3 eV. We observe that the use of the GWA creates a spectra that broadened and contains shoulders. These characteristics of the spectra has been observed in previous calculations of NiO by GWA (Aryasetiawan et al., 1995) where the valence band could not reproduce satellite structures (Aryasetiawan et al., 1995). Massida (Massida et al., 1997) observed a satellite at -9 eV for NiO which corresponds to a 3*d* hole (Massida et al., 1997). This is consistent with experimental spectra where both a broadened quasiparticle peak and satellite structures are observed and interpreted as a transition from a d_8 ground state to a d_7 final state via the Anderson impurity calculations (Aryasetiawan et al., 1995). Aryasetiawan remarks that the GWA is able to produce weak satellite structure and is attributed to overemphasized peak in the imaginary part of the dielectric screening (Aryasetiawan et al., 1995). If compared to the spectral functions of TiO_2, as shown in Fig 4.2 (bottom), a broadening of this characteristic is not seen. We conclude that the broadening and shoulders of the spectra be due to the *d*-orbital contribution as seen in the partial density of states. This is not the case for TiO_2 as the *d*-orbital contribution in TiO_2 is significantly smaller by one order of magnitude compared to NiO. This shows that for the case of NiO, the spectral function moves away from a Dirac delta function which describes the behavior of the non-interacting electron gas. This is said to be due to the correlation terms shifting the occupancy from below to above the Fermi break. This confirms the role that correlation broadens the spectral function and the discontinuity in the momentum distribution. This shows that the impulse approximation is not obeyed more strongly in this region compared to other regions.

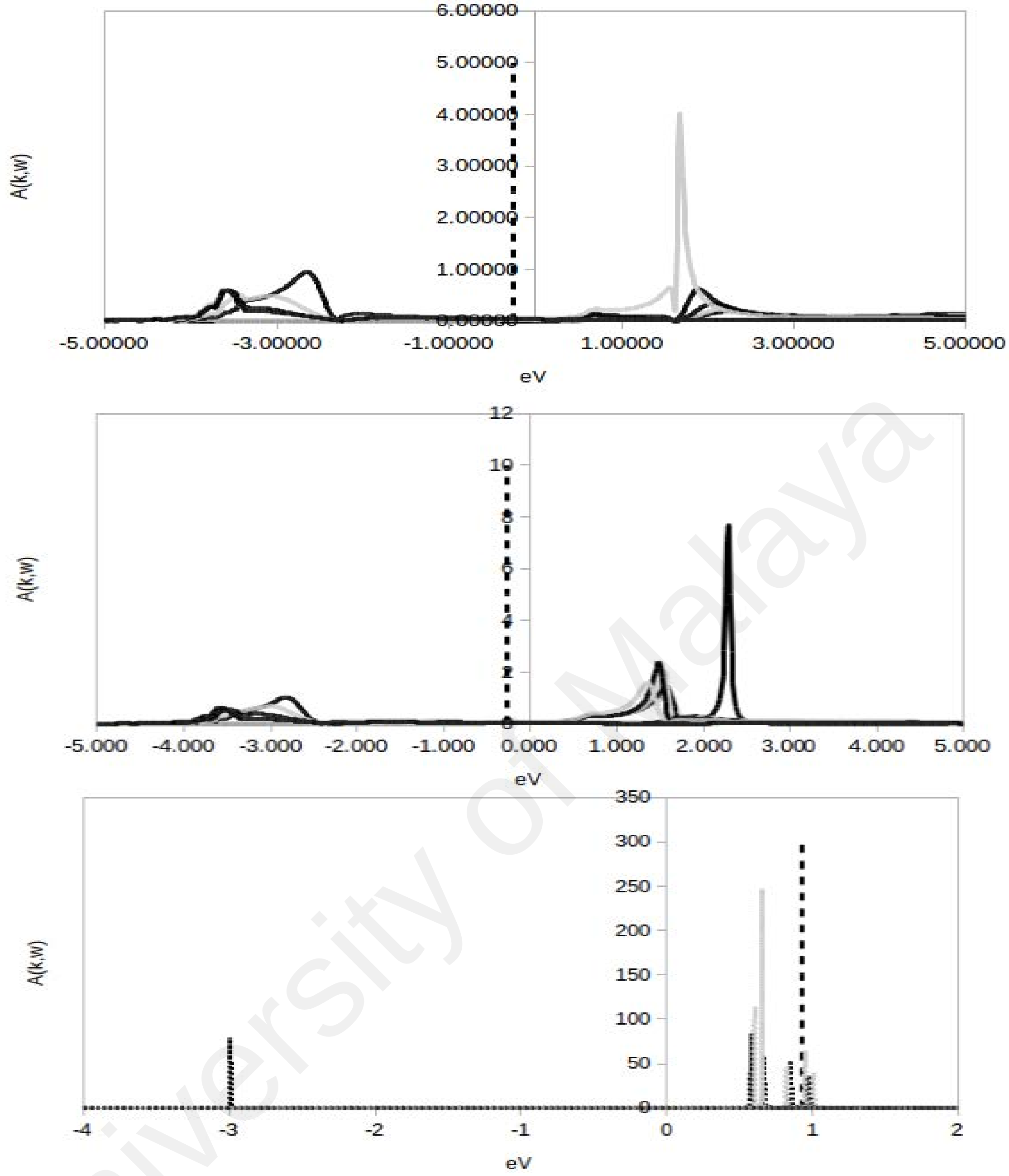

Figure 4.2: NiO spectral functions along the direction [100] (top), [110] (middle) direction and TiO_2 spectral function for the direction [100] (bottom).

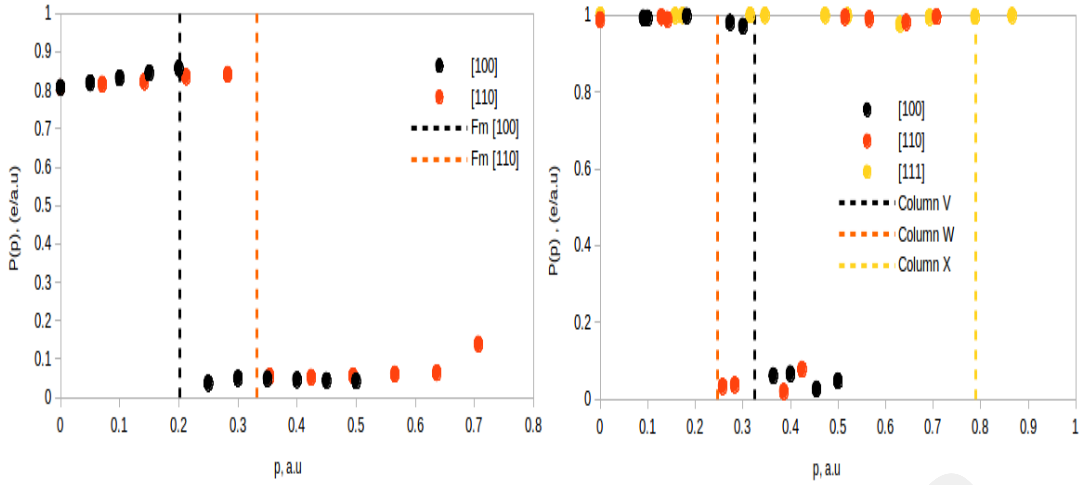

Figure 4.3: GWA momentum density for NiO (left) and TiO_2 (right).

As the spectral function will serve as input to the momentum density and subsequently to the Compton profile, we can now directly study the contribution of the *d*-orbital from the transition metal to the experimental Compton profile by this method. We can now obtain the momentum densities by taking the value of the cumulant of the spectral function over all directions from a set of *k*-points at the Fermi energy as described in Chapter 3. We present the momentum densities in Figure 4.3. At first glance we observe a clear division between high and low momenta for the case of NiO, which means that the impulse approximation is seemingly followed. TiO_2 follows this trend as well but has a unit constant momentum at low momenta with a small, non-zero density after the Fermi break. This is almost similar to the Fermi liquid case where we would expect to see a unity density at low momenta. The reason we see a non-unity momentum density in the case of NiO can be explained by observing the cumulant function of the previously developed spectral functions as shown in Figure 4.4.

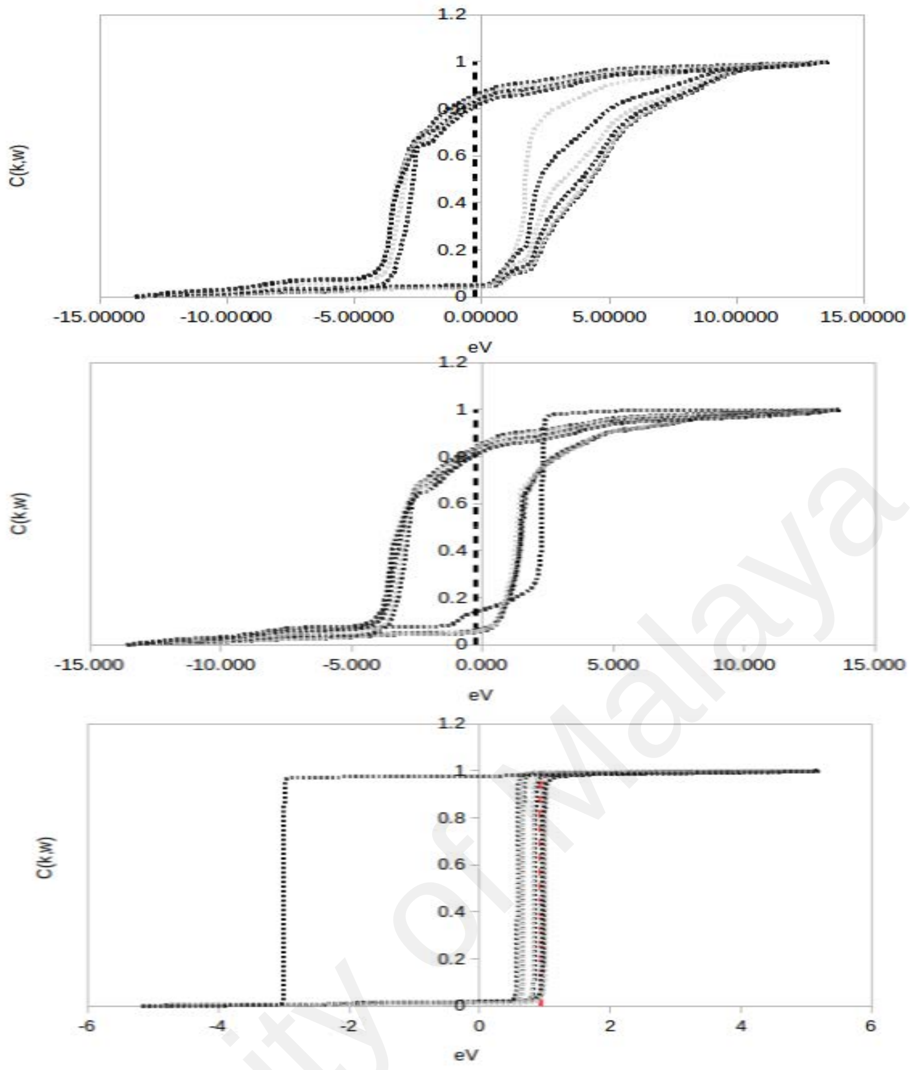

Figure 4.4: NiO cumulant function for the direction [100] (top), [110] (middle) and TiO_2 cumulant function for the direction [100] (bottom).

In the case of TiO_2, an almost Dirac-delta spectra, function instantly accumulates to unity. In the case of NiO, the shoulders and broadening of the spectra accumulate to unity only at higher energies. We have now shown the importance that is played by the self-energy from a GWA calculation to shape the momentum densities of two different TMO systems. When the cumulant of this spectra is obtained to construct the momentum density, we find that the broadening contributes to its inclusion into the momentum density below the Fermi energy. This cumulant will naturally not be at unity at the Fermi energy owing to the curving of the momentum density.

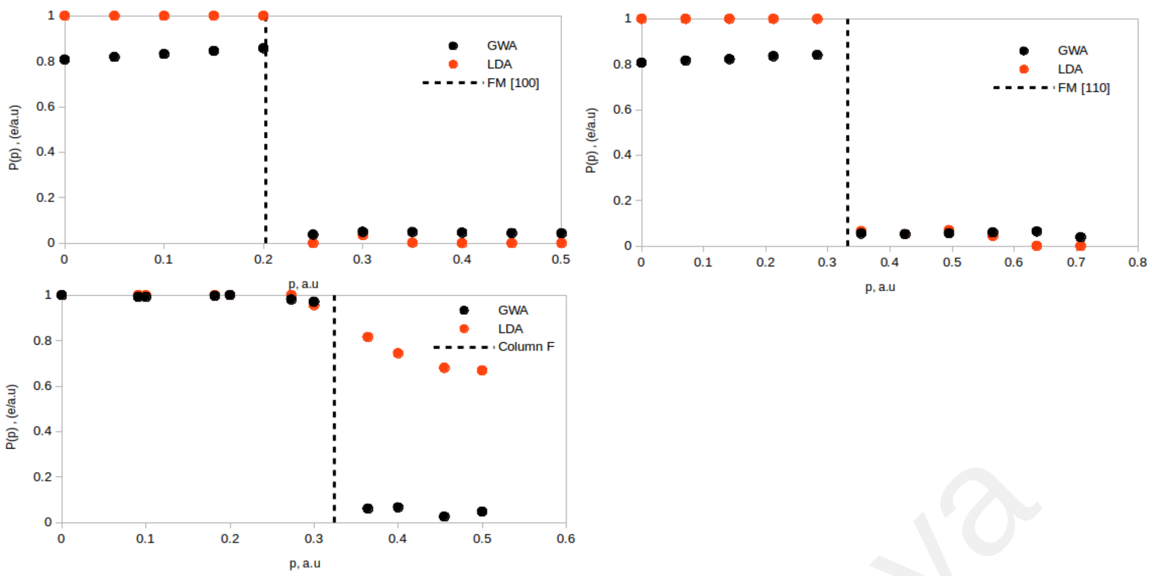

Figure 4.5: GWA vs LDA momentum densities for NiO for the direction [100] (above left), [110] (above right) and TiO_2 for the direction [100] (bottom left).

We now perform a comparison between the ground state and excited state momentum densities as shown in Figure 4.5. For NiO, in both directions, it is now obvious that the inclusion of the self-energy makes the step function momentum density in LDA resemble the Fermi-Dirac distribution as seen in the GWA case. In both directions, from the origin to the *k*-point before the Fermi break, the GWA momentum density is ~17 % smaller than the LDA density. In the case of TiO_2, the GWA momentum densities follow the same trend as the LDA momentum densities. However, at the middle k-points of direction [110] of TiO_2 and after the Fermi break for the direction [100] and [111] the occupancy undergoes cold smearing to an occupancy different than that of the GWA case as shown in Figure 4.3. We will show in our comparison with experimental profiles that our GWA Compton profile has better agreement compared to the LDA calculations.

This supports the use of GWA to obtain Compton profiles as it has been reported by Aryasetiawan (Aryasetiawan et al., 1995) which states that GWA can be regarded as HF without screening , in which the screening term leads to a larger reduction of gap due to long range correlations. This difference to spectra in lower momenta is caused by the interplay of the values of the frequency, ground state energy, real and self-energy as given by Equation 2.113. Physically, this broadening is said to be due to the finite lifetime width of the spectral function reacting slower to change of momentum and energy transfer of probing energies. It involves final state electrons where the excited particle is polarized by the tightly bound core electrons and the hole it leaves behind. This polarization is directly obtainable from our first principles calculation Equation (2.109) and used to obtain the final self-energy. Just from a simple comparison of ground state and excited state densities, it is obvious that polarization plays a significant role in the interpretation of the momentum density.

4.1.3 Compton Profiles

With the momentum density, we can proceed to obtain the Compton profiles for both GWA and LDA cases. These profiles are compared with the experimental Compton profiles of Fukamachi (Fukamachi et al., 1973) for both directions in NiO and the profiles of Limandri (Limandri et al., 2014) and difference profile of Joshi (Joshi et al., 2007) for the direction [100] in the case of TiO_2. In their work, Fukamachi have stated that they have used a solid state detector and multichannel pulse height analyzer. The radiation is 59.54 keV γ-rays from ^{241}Am (100 mCi) with a scattering angle fixed at 165^o for profiles measured along three major axes [100], [110] and [111]. Counts are accumulated in five days until the peak value reaches $8x10^4$ counts. We initialized a Gaussian convolution of 0.57 a.u in the case of NiO and 0.28 a.u in the case of TiO_2. The results are shown in Figure 4.6. For the case of NiO, our Compton profiles are shown to provide a good fit to previous experimental results. This is shown in the small differences in the difference profiles between the theoretical and experimental plots. In both cases of NiO, there is larger disagreement in GWA compared to LDA at the origin.

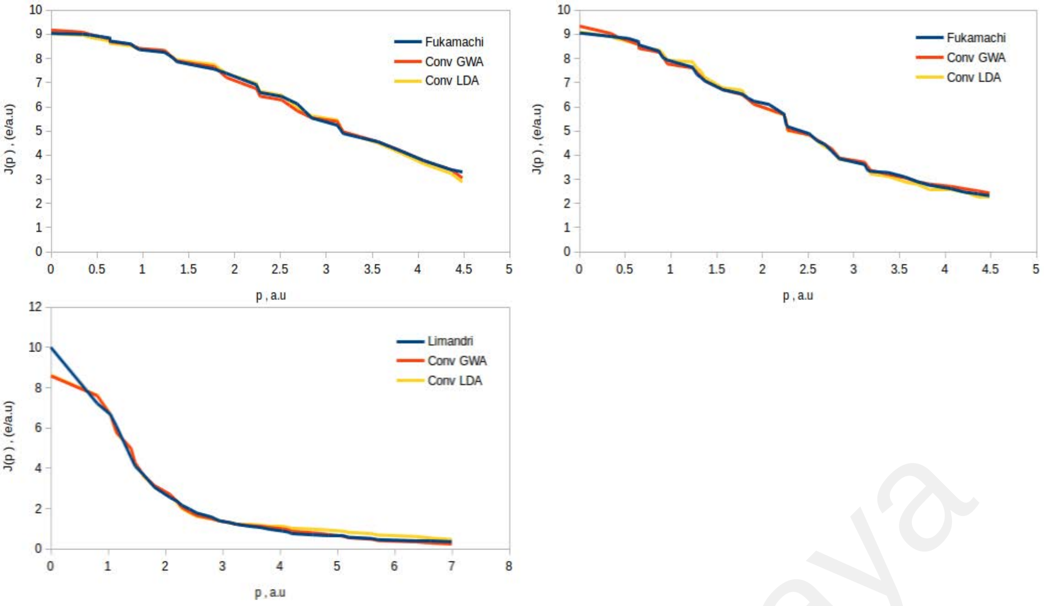

Figure 4.6: Compton profile for NiO for the direction [100] (above left), [110] (above right) and TiO_2 for the direction [100] (bottom left).

Table 4.6: Sum of difference profiles for NiO along two directions of interest.

Sum of Difference Profiles		
	GWA	**LDA**
[100]	2.995925	3.30137
[110]	3.071575	3.81246167

This means that the non-unity GWA momentum densities at the origin should resemble its LDA counterparts by decreasing its broadening. This might be achievable by an increase in k-point resolution. The decrease in low momenta from the ground state calculation is due to the valence energy contribution. It is in line with what has been observed in experimental profiles which is said to be a discrepancy with LDA calculations and has been observed in other works as well. Using the localized ion model, (Chiba et al.,1974) has calculated positron angular correlation curves of NiO single crystals and observed that the discrepancy with experiment is fairly large in the low momentum region as well. However above the origin, NiO seems to have better agreement compared to LDA except a large disagreement between 1.7-2.7 a.u in the

[100] direction. This section is attributed to an O atom and the difference profile overshoots as the quantity of p-orbitals is smaller for the valence band.

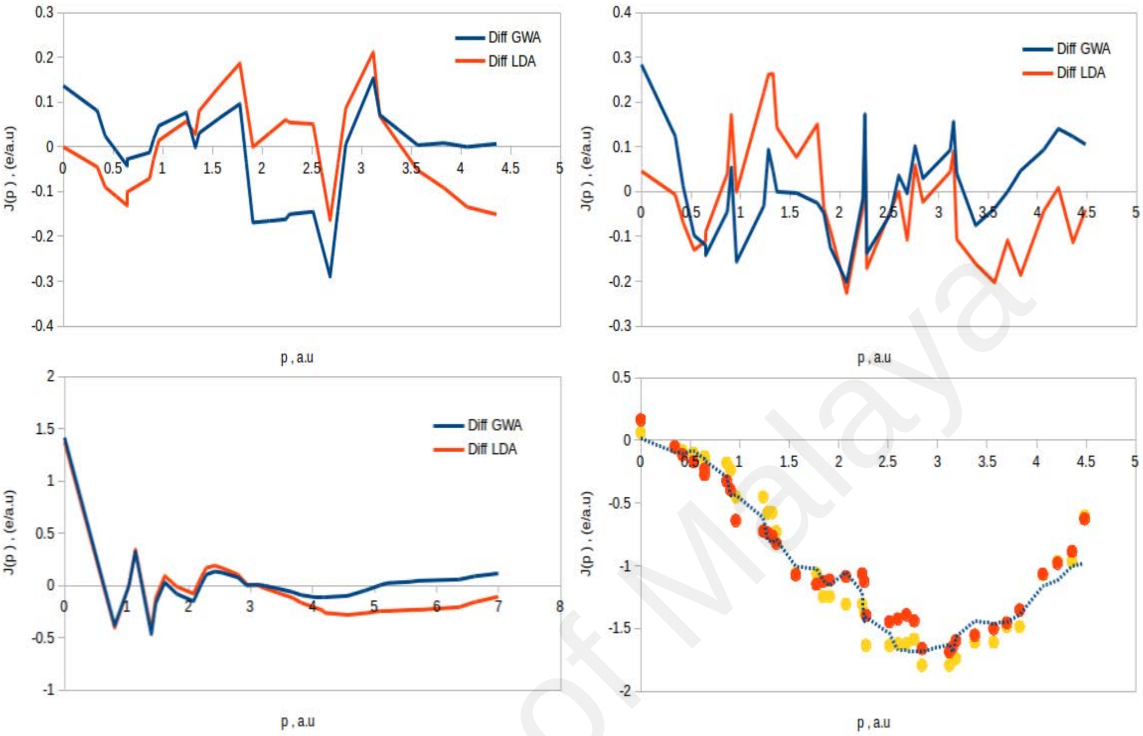

Figure 4.7: Difference profiles for NiO for the direction [100] (above left), [110] (above right) and TiO_2 for the direction [100] (bottom left). Comparison of anisotropy (bottom right) for NiO with experiment.

Nevertheless, if we take the sum of the absolute values of the difference profiles in Table 4.6 we observe that that the GWA profile has a better agreement compared to LDA. We are also able to find good agreement between the anisotropy of Fukamachi with our calculation as shown in the Figure below. Fukamachi compared his experimental profile with a model based *d*-electron formalisms of (Azaroff, 1974) and wavefunctions of (Clementi, 1965). The anisotropy reveals that the GWA and LDA follow the results of Fukamachi in which submaxima structure is non-existent.

Table 4.7: QPRF for TiO_2 and NiO along all calculated k-points.

NiO *k*-points			**QPRF**	$\delta\Sigma/\delta E$	**TiO_2 *k*-points**			**QPRF**	$\delta\Sigma/\delta E$
0.5	0	0	0.407	-1.456	0.5	0	0	0.727	-0.375
0.45	0	0	0.415	-1.407	0.455	0	0	0.716	-0.397
0.4	0	0	0.384	-1.601	0.4	0	0	0.707	-0.414
0.35	0	0	0.362	-1.76	0.364	0	0	0.714	-0.401
0.3	0	0	0.32	-2.125	0.3	0	0	0.692	-0.445
0.25	0	0	0.308	-2.242	0.273	0	0	0.704	-0.42
0.2	0	0	0.288	-2.476	0.2	0	0	0.688	-0.454
0.15	0	0	0.283	-2.532	0.182	0	0	0.699	-0.43
0.1	0	0	0.302	-2.306	0.1	0	0	0.695	-0.44
0.05	0	0	0.381	-1.627	0.091	0	0	0.7	-0.428
0	0	0	0.43	-1.325	0	0	0	0.701	-0.427
0.05	0.05	0	0.351	-1.846	0.091	0.091	0	0.7	-0.429
0.1	0.1	0	0.288	-2.471	0.1	0.1	0	0.691	-0.447
0.15	0.15	0	0.273	-2.669	0.182	0.182	0	0.7	-0.429
0.2	0.2	0	0.266	-2.761	0.2	0.2	0	0.685	-0.459
0.25	0.25	0	0.259	-2.856	0.273	0.273	0	0.708	-0.413
0.3	0.3	0	0.249	-3.02	0.3	0.3	0	0.707	-0.415
0.35	0.35	0	0.24	-3.163	0.364	0.364	0	0.701	-0.427
0.4	0.4	0	0.236	-3.24	0.4	0.4	0	0.689	-0.451
0.45	0.45	0	0.228	-3.385	0.455	0.455	0	0.698	-0.432

In the case of TiO_2, the calculated Compton profile is shown to be in agreement with the experimental difference profile of Joshi where it is shown that the GWA reproduces a smaller difference profile at higher momenta compared to the LDA and the larger disagreement at the origin in both the GWA and LDA case. In our case we observe that the calculated GWA momentum density as shown in the Figure above constructs a better Compton profile compared to LDA. Joshi remarked that only a higher momenta profile agrees with experiment and this is attributed to core electron contributed while disagreement is seen in the origin. Joshi calculated the Lam-Platzman correction based on free atom profiles and observed that the theoretical values are lower than experiment in low momenta. They conclude that full atom profiles are inadequate to obtain the Compton profiles and state a preference for Hartree-Fock LCAO (HF) methods to obtain difference profiles which have better agreement with experiment. Linear combination of atomic orbitals have been remarked to be in better agreement to construct Compton profiles compared to plane wave methods. The construction of the profile from GWA contour deformation spectral function is possible via the code FIESTA which is based on Gaussian basis sets. However this code is not distributed by their developers.

Finally we compare the QPRF of NiO and TiO_2 for the band under Fermi energy as shown in Table 4.7. As is shown in Equation (3.44), as the change in the correlation part of the self-energy gets larger the QPRF gets smaller. This means that the correlation portion of the self-energy is more significant in NiO compared to TiO_2. This confirms the previous result of the spectral broadening.

4.2 NiO, CoO and FeO

In this section, we firstly calculated the excited state and ground state band structure calculations for NiO, CoO and FeO. We observe that NiO can produce a larger band gap compared to FeO and CoO via GWA We then calculated the Fermi energy and Fermi momenta which will be subsequently used to obtain the spectral functions. We observe that NiO has twice broadened spectra compared to FeO and CoO. These functions will be used to obtain the momentum density. We then compared and explained the differences between GWA and ground state momentum densities. Finally we use the momentum densities to construct the Compton profile. The profiles will be analyzed in terms of difference profiles and anisotropy. The difference profile reveals that in the direction $[00\bar{1}]$, the correlation correction is smaller in the low momenta compared to $[\bar{1}0\bar{1}]$ while the higher momenta goes to zero. The amplitude of the anisotropy of NiO is seen to be larger than FeO and CoO.

4.2.1 Band Energies

We firstly compare the band gaps between ground state and excited state calculations as shown in Table 4.8.

Table 4.8: Band gaps for NiO, CoO and FeO along the [00$\bar{1}$] and [10$\bar{1}$] direction.

***k*-points**			**Band gaps, eV**					
			NiO		**CoO**		**FeO**	
			E^0_gap	**E^GW_gap**	**E^0_gap**	**E^GW_gap**	**E^0_gap**	**E^GW_gap**
0	0	0	3.443	0.473	2.335	-0.678	1.903	-0.773
-0.056	0	-0.056	3.395	1.384	2.375	0.149	1.955	-0.03
-0.111	0	-0.111	3.769	2.529	2.838	1.502	2.438	1.278
-0.154	0	-0.154	4.364	3.358	3.471	2.578	3.088	2.295
-0.2	0	-0.2	5.131	4.316	4.254	3.584	3.875	3.272
-0.25	0	-0.25	5.947	5.101	5.07	4.514	0.281	0.352
-0.308	0	-0.308	6.679	5.798	0.16	0.316	0.191	0.334
-0.357	0	-0.357	7.005	6.113	6.227	5.414	0.644	-0.557
-0.4	0	-0.4	7.081	6.156	6.366	5.994	0.627	-0.677
-0.444	0	-0.444	7.077	5.967	6.327	5.94	0.081	-0.603
-0.467	0	-0.467	7.073	5.945	6.301	5.889	0.114	-0.623
			NiO		**CoO**		**FeO**	
			E^0_gap	**E^GW_gap**	**E^0_gap**	**E^GW_gap**	**E^0_gap**	**E^GW_gap**
0	0	0	3.444	0.479	2.335	-0.678	1.903	-0.773
0	0	-0.067	3.496	1.312	2.452	0.069	2.042	0.015
0	0	-0.133	3.709	2.408	2.738	1.372	2.315	1.088
0	0	-0.154	3.801	2.67	2.844	1.771	2.421	1.461
0	0	-0.2	4.029	3.081	0.929	0.328	1.029	0.361
0	0	-0.267	1.398	1.156	1.251	0.772	1.349	0.793
0	0	-0.308	1.565	1.418	1.402	1.117	1.501	1.083
0	0	-0.357	1.71	1.667	1.531	1.405	1.625	1.368
0	0	-0.4	1.79	1.674	1.599	1.619	1.687	1.562
0	0	-0.462	1.845	2.196	1.641	1.708	1.724	1.598
0	0	-0.467	1.847	2.198	1.643	1.749	1.724	1.642

E^0_gap	Ground state band gap
E^GW_gap	Excited state band gap

In similar fashion as the previous section, we observe that the GWA band gap has disagreement with the LDA band gap at k-points near the origin. We thus opt to increase the GWA band gap by employing a scissor shift to ensure that the band gaps are similar to the experimentally obtained band gaps. For NiO, the scissor shift is 4.3 eV, for CoO and FeO the scissor shift is 2.4 eV (Terakura et al., 1984).

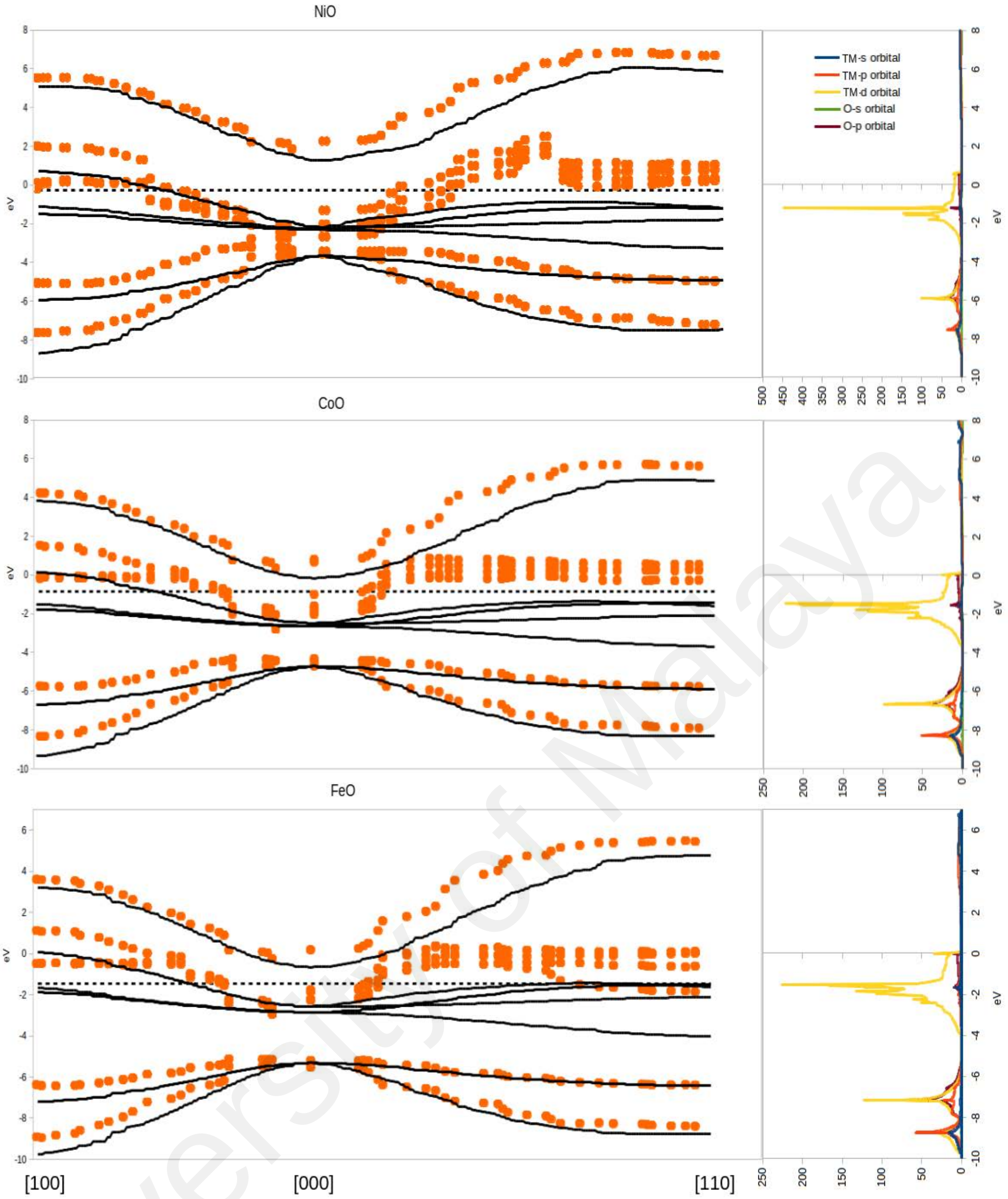

Figure 4.8: Band structure and partial density of states for NiO, CoO and FeO.

We present the band structure and partial density of states in Fig 4.8. From the partial density of states, we observe that the valence band consists of a large contribution of TM *d*-orbital with a small contribution of O *p*-orbital. NiO has the largest contribution of d-orbital compared to FeO and CoO. If a scissor shift were not applied, our band gap for FeO and CoO would agree with a previous study where t_{2g} bands fail to open up (Das et al., 2015). From the partial density of states, we observe that the conduction band consists of TM *d* and *p* orbital contribution while the top of it consists of Ni 4*s* orbital contribution. In the case of NiO, we also observe that our GWA calculation has a larger gap between the conduction and valence band energies in a similar way as the ground state energies compared to the case of FeO and CoO.

Similar to the previous section with NiO, all oxides shows broad valence band maximum shoulders due to flat 3*d* t_{2g} bands with a small O 2*p* contribution (Rodl et al., 2009; Das et al., 2015; Aryasetiawan et al., 1995). Similarly to our previous section, we did not observe a decrease in energy and Fermi levels to lie within the t_{2g} states as previously reported by Rodl. Jiang (Jiang et al., 2010) has remarked that the cubic crystal field environment without symmetry breaking makes ground state high spin configurations degenerate which predicts a metallic state in band theory for the case of FeO and CoO. In the case of CoO, Das (Das et al., 2015) observed that GGA fails to yield non-zero band gap because the measured gap may be influenced by strong correlations. Using self-consistent GWA, they observe the converged band gap to be 4.78 eV.

Table 4.9: Fermi momenta of the NiO, CoO and FeO along the $[00\bar{1}]$ and $[\bar{1}0\bar{1}]$ direction.

	$[00\bar{1}]$, p_F /a.u.	**$[\bar{1}0\bar{1}]$, p_F /a.u.**
NiO	0.1996	0.2180
CoO	0.2033	0.1566
FeO	0.1689	0.1615

Table 5.1: Fermi energy of the NiO, CoO and FeO.

	Fermi Energy, eV
NiO	-0.3
CoO	-0.842
FeO	-1.439

In Table 4.9, we present the Fermi momentum of the oxides studied. These values play the role of revealing where the break between the high momentum density and low momentum density is located. We have initialized the oxide systems in this study with the same crystal structure and thus the Fermi momentum is expected to show the same trend in both directions. In the same way as the previous section, we obtain the Fermi energies as the midpoint between the conduction and valence band of the G point. These values are shown in Table 5.1.

4.2.2 Spectral Function and Momentum Densities

Knowing the Fermi energy, we are now able to study the spectral functions of these oxides as shown in Figure 4.9. The spectral function reflects the poles of one-electron Green's function as it is related to electron removal and addition energies. In both directions, we observe that the spectra below the Fermi energy are more broadened compared to that above the Fermi energy. A deeper look into the valence energy spectra shows that NiO has twice broadened spectra compared to FeO and CoO. As this spectral function was constructed from the valence energy band, differences in spectra between the oxides can be explained by looking back to the partial density of states. We observe that NiO has twice the contribution of *d*-orbitals compared to FeO and CoO. We propose that this larger contribution creates a much broader spectra in the case of NiO.

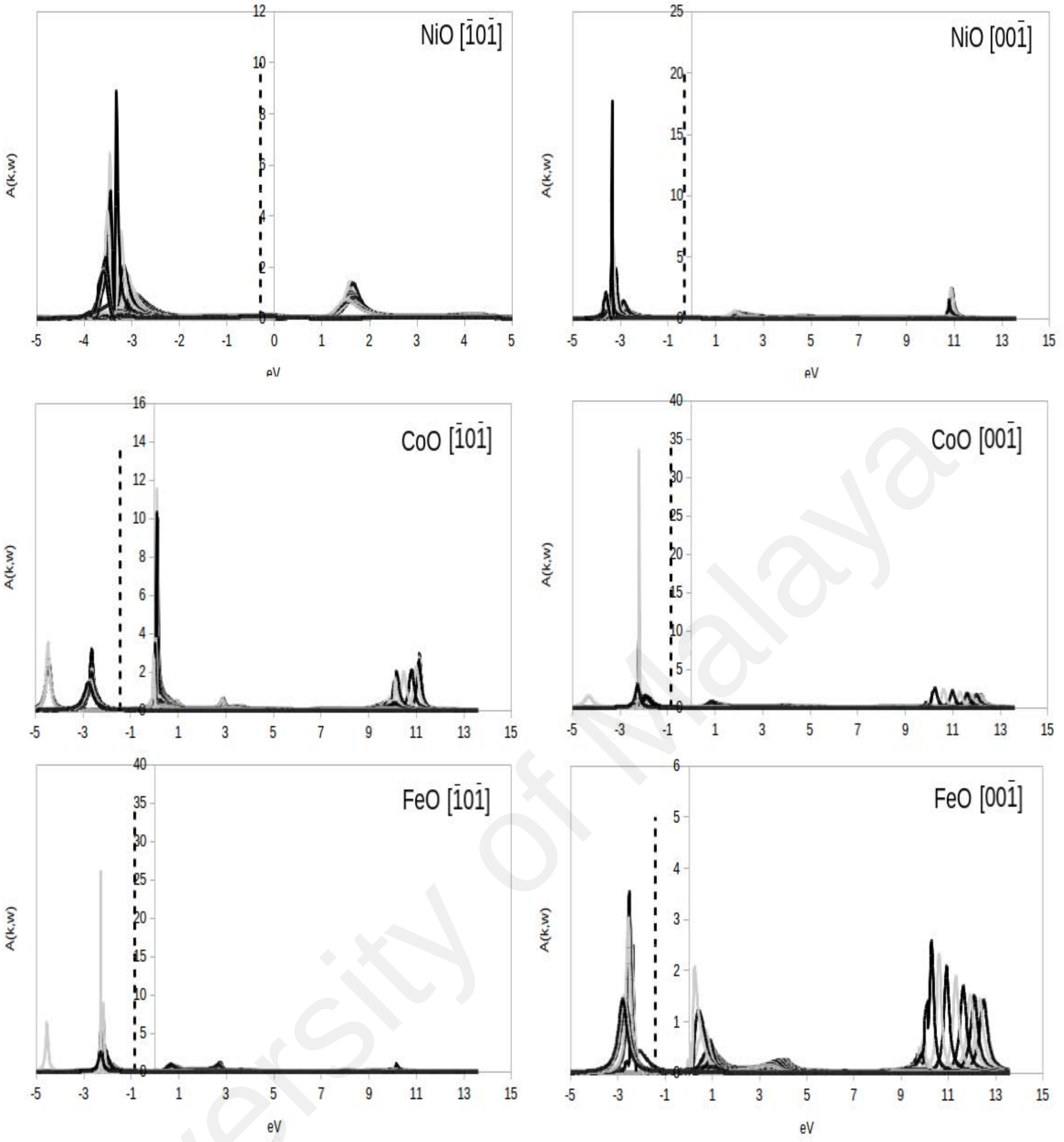

Figure 4.9: Spectral functions of the NiO, CoO and FeO along the [$00\bar{1}$] and [$\bar{1}0\bar{1}$] direction.

With our insight into the spectral functions of the oxides, we are able to study their momentum densities as presented in Figure 5.1. For systems which do not have an isotropic Fermi surface, we expect directional dependence in their momentum densities. This is especially true for the case of transition metals. This consequence is observed in densities along the direction [001] to have a lower Fermi break compared to the direction [101]. In similar case to NiO in the previous section, we observe that the GWA momentum densities are not at unity before the Fermi break. In the LDA case, they are at unity. We initially observed that in the case of CoO, the density for the *k*-points at the Fermi break are all lowered compared to those near the origin and in the case of FeO, the densities before the Fermi break are uniformly around 0.6. This can be explained by observing that the scissor shifts of spectra below the Fermi break are initialized as smaller for FeO and CoO compared to NiO. These spectra nearer to the Fermi break are misrepresented in the momentum density as the peak in the cumulant goes above the Fermi break.

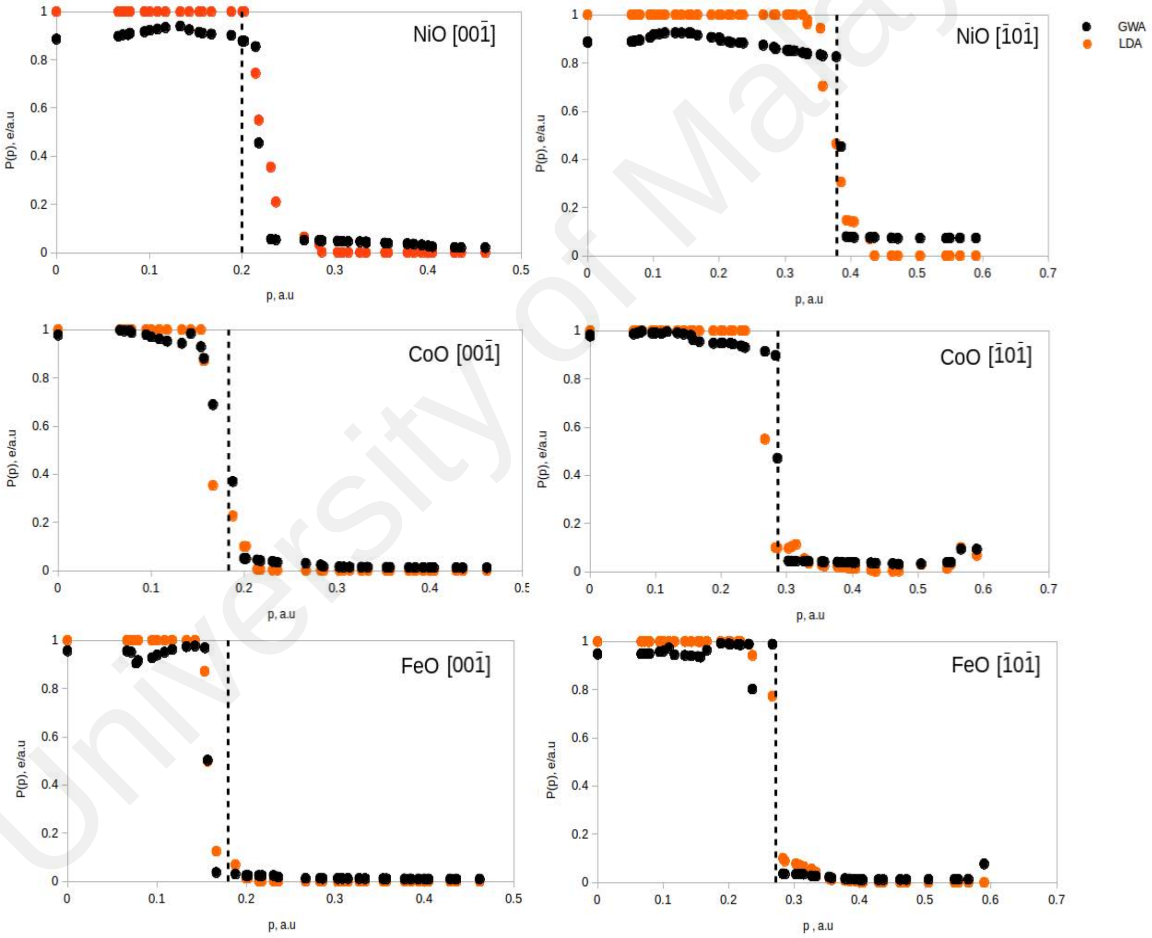

Figure 5.1: Momentum densities of the NiO, CoO and FeO along the [00$\bar{1}$] and [$\bar{1}$0$\bar{1}$] direction.

This issue can be solved by fitting these spectra to a Lorentzian given by

$$l(\omega) = \frac{Z_{QP}}{\pi} \frac{\eta}{(\omega - \omega_O)^2 + \eta^2} \tag{4.1}$$

where Z_{QP} sets the amplitude of the fit, ω_o sets the position of the energy of the spectral peak and η is the fitting parameter, and using *l(ω)* to construct the momentum density. This approach was introduced by Olevano (Olevano et al., 2012) to account for misrepresentation of the spectra as a result from being constructed with an insufficient amount of *k*-points.

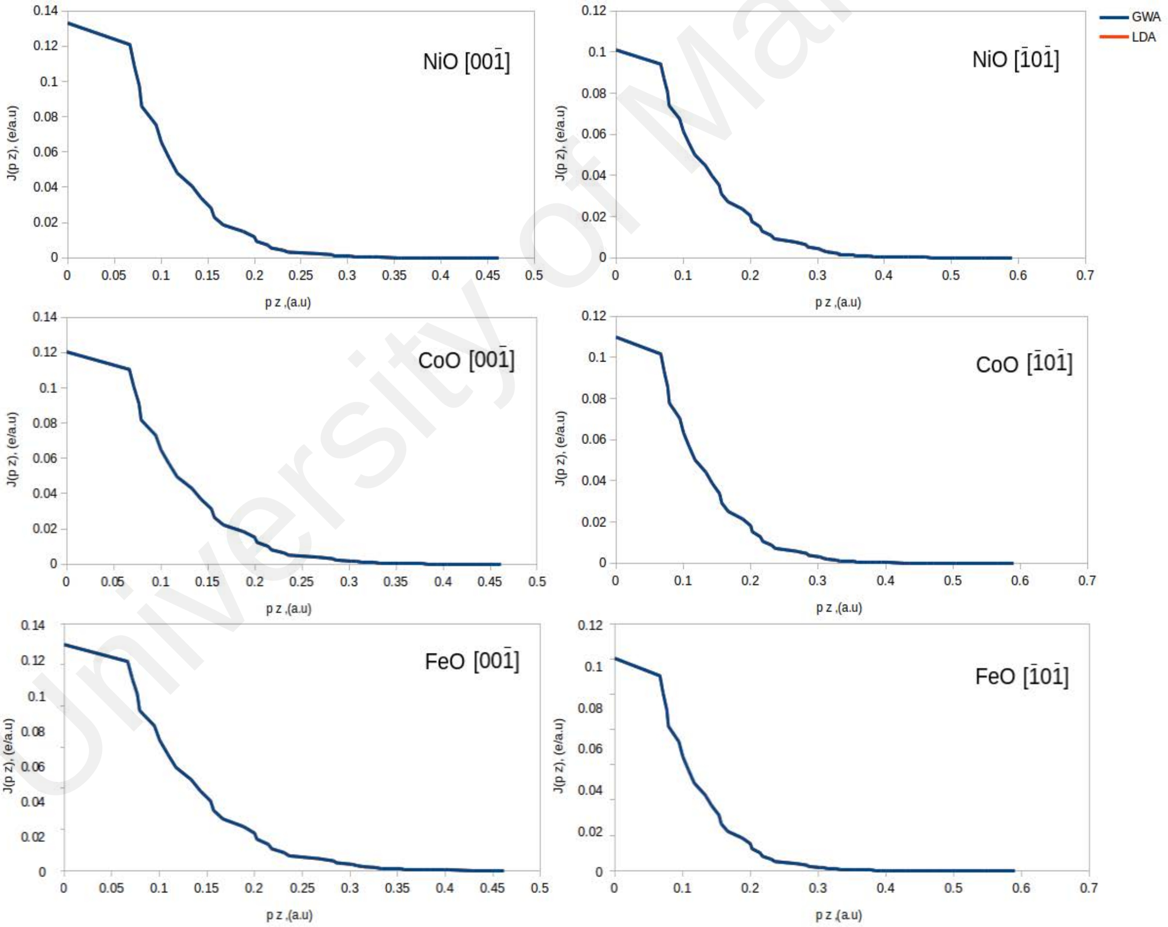

Figure 5.2: Compton profiles of NiO, CoO and FeO along the [00$\bar{1}$] and [$\bar{1}$0$\bar{1}$] direction.

This is due to low momentum occupation near the Fermi surface as the quasiparticle lifetime goes to infinity. Our use of this method is justified in this study as we observe negative band gaps for certain *k*-points in the case of CoO and FeO which indicates an insufficient amount of *k*-points to construct the spectra.

In previous comparisons of calculated momentum density at the valence band to experiment at equilibrium temperature we expect to observe a step function that is unity at the origin. Smearing of occupancy is then observed before and after the Fermi break followed by a drop to zero occupancy at the Fermi break with a step-wise discontinuity until the Brillouin zone edge. This indicates a transfer of occupancy from below to above the Fermi break typical of many body effects (Olevano et al., 2012). From our results, we observe that compared to the case of the noninteracting electron gas, there is occupancy above the Fermi break. This is due to the use of GWA to obtain the momentum densities which lowers the profile before the Fermi break compared to LDA and increases it in the higher momentum regions. This smearing is thus due to the self-energy which increase as electron density increases and we can expect further increase in occupancy above the Fermi momentum. In this high density limit, kinetic energies dominate. At momenta greater than the Fermi break, the core asymmetry dominates. At momenta less than the Fermi break, kinetic energy is the highest and the valence band dominates (Sternemann 2000). In our case, the self-energy term provides the value for the correlation. This makes the momentum density a closer fit to experimental observations. The experimental peak height is due to neglect of exchange and correlation effects. These effects play the role of promoting electrons from low to high momentum states and it reflects the degree of core and conduction electron correlation.

In order to obtain a GWA calculation that is close to experiment, the initial LDA band energies have to be very close to the quasiparticle band energies. ABINIT ensures this by using the KS states as the input to its GWA calculation. Continuity across the Fermi break indicates electron correlation typical of *d*-orbitals. The NiO momentum distributions are more occupied in the low momentum region compared to FeO and CoO which are almost equal.

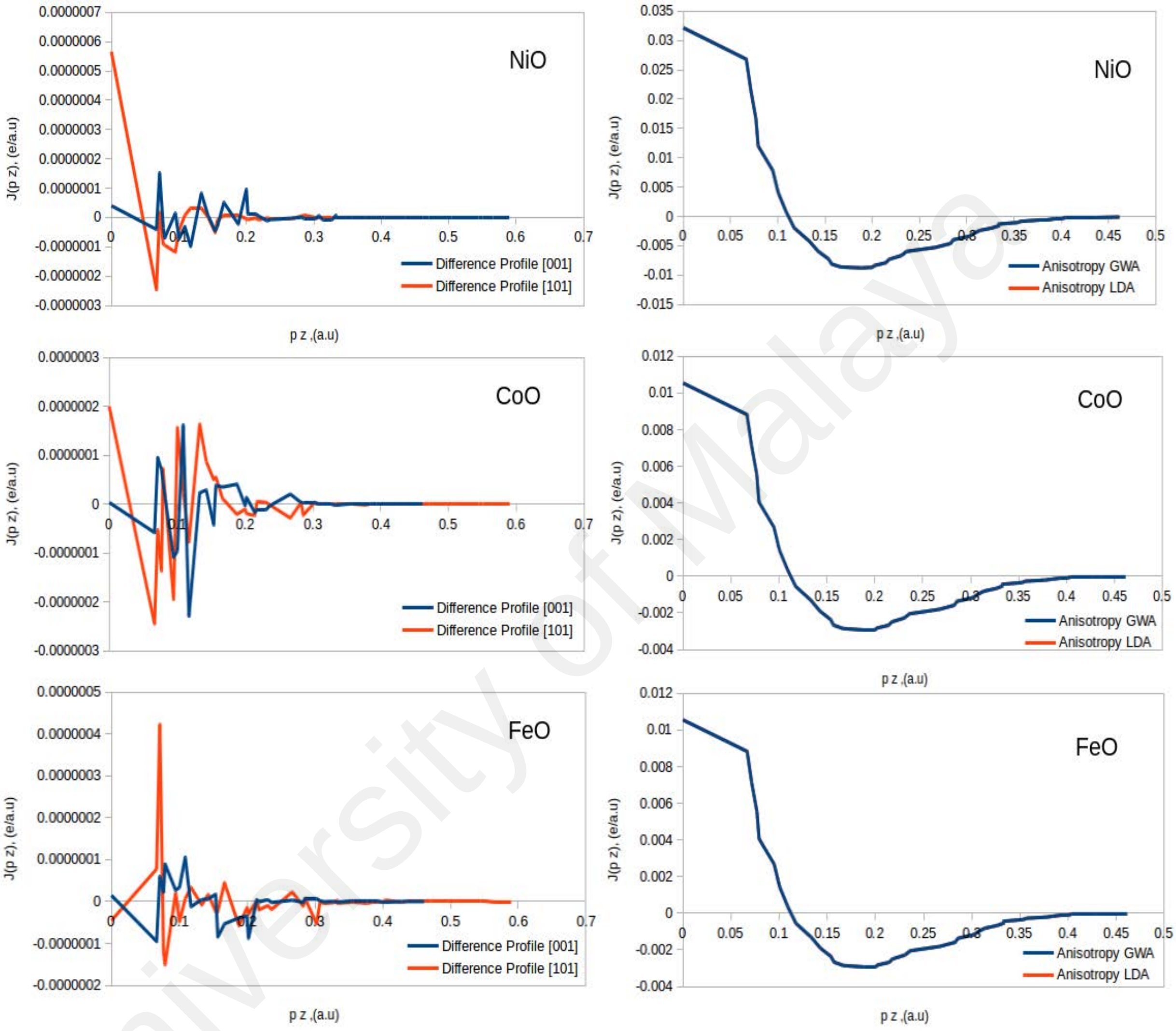

Figure 5.3: Difference profiles (left) and anisotropy (right) for NiO, CoO and FeO.

This lends credence to the well known behavior of NiO as a strongly correlated system. A lack of smearing before and after the Fermi break is typical of spectra without broadening as seen in LDA calculations. In our case, this smearing is directly related to the broadening of the spectral function as shown in Equation 2.66 which requires as input the self-energy correction. Thus, the positioning of the Fermi energy and the role played by the self-energy term to broaden the spectra highlight the importance of these tools in studying electron correlation in momentum densities.

4.2.3 Compton Profiles

Now that we have obtained the momentum density, we can proceed to construct the Compton profile (Figure 5.2) and study its correlation correction and anisotropy (Figure 5.3). We performed a Gaussian convolution on the calculated Compton profile of 0.57 a.u as initialized in the previous section for NiO. We notice that the difference between GWA and LDA Compton profiles is not observed in the figure. However the difference profile in Figure 5.3 points out important characteristics between them. The difference profiles follow from the previous study of Cardwell as discussed in the previous chapter. We notice in all three oxides that in the direction $[00\bar{1}]$, the correlation correction is smaller in the lower momenta compared to $[\bar{1}0\bar{1}]$ while the higher momenta which corresponds to the core states goes to zero. An explanation to this can be seen in the partial density of states calculated specifically from *k*-points over the directions $[00\bar{1}]$ and $[\bar{1}0\bar{1}]$ respectively as shown in Figure 5.4. As the *d*-orbital contribution to the valence energy for the direction $[00\bar{1}]$ is larger compared to $[\bar{1}0\bar{1}]$, we propose this explanation as the reason of the difference in magnitude of the correlation correction near the origin. This PDOS is for the ground state case but similarly reflects the orbital contribution as the excited state case. In comparing individual *k*-points, the largest difference lies with the *k*-points near the origin. This is the region where the TM atom is initialized and has the highest contribution of *d*-orbital. A lower calculated profile at the origin compared to experiment is a common observation in previous studies. Huotari, (Huotari et al., 2007) observed this in their study using an analytical spectral function to convolute with their experimental valence Compton profile in the case of Be. In their study the width of their spectra grows with increasing electron density. Other studies include (Wakoh et al., 1990; Kralik et al., 1998; Schulke et al., 1996; Baruah et al., 1999; Wakoh et al., 2000; Bross, 2004;Makkonen et al., 2005). An explanation for this observation has been given by Anastassopoulos (Anastassopoulos et al., 1991) who attributed it normalization of the Compton profile in a limited k-space.

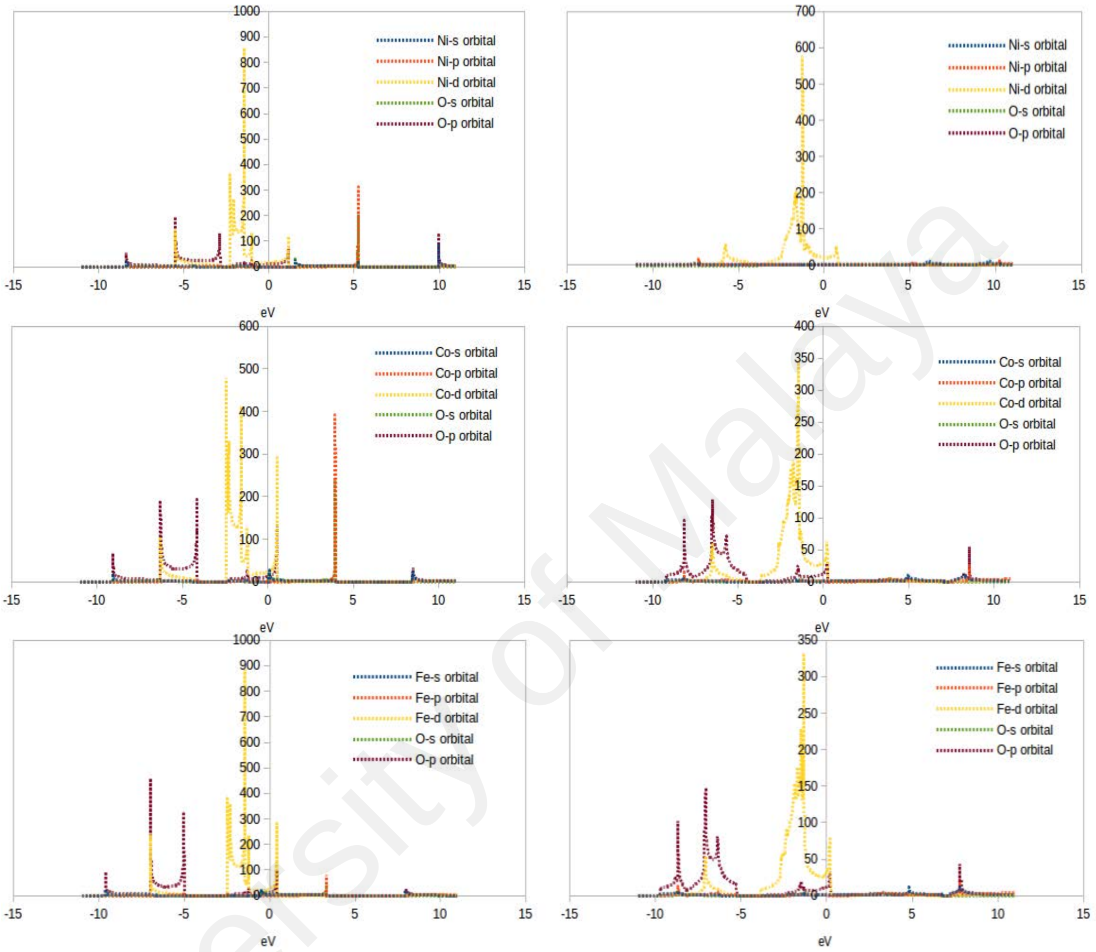

Figure 5.4: PDOS for NiO, CoO and FeO along z-direction (left) and along x-z direction (right).

The difference profile reflects fluctuations in the intermediate density. This region is affected by conduction electrons (Cardwell et al., 1989). A large difference between the LDA and GWA momentum density at the intermediate level shows that the self-energy has a strong effect in this region. These effects play the role of promoting electrons from low to high momentum states and reflect the degree of core and conduction electron correlation. In our case, the self-energy term provides the value for the correlation. Besides self-energy, other physical properties that can affect the momentum density at the Fermi break was provided by Anastassopoulos (Anastassopoulos et al., 1991) for Ni where the occupation transfer between occupied to non-occupied side of discontinuity is due to thermal excitations and non-local correlation effects. Sternemann has studied the role by played temperature in their study of the Compton profile of Al and Li. They observed that the Compton profile narrows with increasing temperature and is attributed to variations in the lattice constants and can be explained well by a free electron model with correlated occupation number density in the case of Al. After the Fermi break, Li is observed to show large difference from experiment as temperature increases.

We are also able to study the anisotropy between directions by plotting the difference between two directions in Figure 5.3. Structure in these difference profiles originate from the Umklapp contributions, Fermi surface distortion from a sphere, band structure effects and interaction of electron bands with Brillouin zone (BZ) faces (Ohata et al., 2000). Thus, the momentum dependent terms that contribute to anisotropy are the occupation function and the Bloch wave amplitude (Rollason et al., 1987). Directional anisotropies are useful in removing systematic errors in experimental and theoretical results (Baruah et al., 1999). In previous studies, events in the anisotropy profile show in terms of oscillatory structure and have been attributed to energetic and geometrical constraints. (Rollason et al., 1987) observed that the positions of oscillations in their calculated anisotropy profile is the same as experiment but of larger magnitude. The origin of these oscillations is said to be due to non-local correlations smearing momentum density and populate empty regions. Anastaspoulous (Anastassopoulos et al., 1991) observed that the oscillatory structure in large momenta due to a decrease of *s*-orbital contribution leaving only *d*-orbital contribution. Sundarajan (Sundarajan et al., 1988) also observed that their calculated oscillatory anisotropic profiles magnitudes are larger but their peak positions agree. Their anisotropic occupation numbers of Ni are due to not just the first BZ but higher BZs as well. In our studies, we did not observe oscillatory structure in agreement with the results of the previous section. However, the amplitude of the anisotropy of NiO is seen to be larger than FeO and CoO. This is due to the momentum density for NiO being more broadened in both directions. This broadening in GWA momentum densities compared to LDA densities also explains the differences seen in the anisotropy. In comparing anisotropies between experiment and calculation of Be, Huotari (Huotari et al., 2000) observed a larger amplitude in calculation compared to experiment and attributed it to asymmetry of valence electron profiles induced by spectral function and vertex correction. This confirms the importance of *d*-orbital component in NiO compared to FeO and CoO.

4.3 ZnSe

DFT calculations using the LDA functional produces reliable ground state properties of solids hence useful for structural studies such as finding lattice constants (Zakharov et al., 1994) but not suitable in describing energy levels of Zn 3*d* semicore states, spin-orbit coupling, crystal field splitting energy (Kharazanov et al., 2006) and band gaps of solids (Fleszar et al., 2005). Semicore states are highly localized and the choice of exchange correlation functional is important for calculating the quality of Kohn-Sham orbitals (Luo et al., 2002). The large error between LDA eigenvalues for localized semicore states compared to experimental values has been explained by Aryasetiawan (Aryasetiawan et al., 1996). For these states, a large contribution is obtained from polarization where an overestimation of exchange correlation energy is seen between 3*d* electron and 3*s*-3*p* core. To rectify these problems with LDA for the case of ZnSe, many corrections have been proposed. Oshikiri (Oshikiri et al., 1999) has stated that using gradient corrections by the GGA functional does not significantly improve the band gap due to a lack of nonlocality and energy dependence in the exchange correlation potential. Kharazanov (Kharazanov et al., 2007; Kharazanov et al., 2006) has proposed the use of LDA+*U* to rectify the band gap problem and observed that the empirically defined *U* and *J* term corrects the Zn 3*d* energy levels, suppresses hybridization, improve band gap estimation and causes the height of peaks in DOS corresponding to Zn 3*d* states to become larger compared to LDA which means that the semicore 3*d* states become more localized than pure LDA. They have also stated that exact exchange DFT can obtain good agreement with experimental band gaps and 3*d* energy levels. Gürel (Gürel et al., 2012) has applied the Tran-Blaha modified Becke-Johnson functional and observes that the band gap and band dispersion curves can be reproduced accurately without the need for shifts. However, they have reported that this functional underestimates spin-orbit splitting. Zakharov (Zakharov et al., 1994) included partial core corrections in the exchange and correlation terms to account for nonlinearity of exchange and correlation potential in region where core and valence charge densities overlap and found that core corrections are more important for conduction bands than valence bands.

The GWA has also been proposed to improve band gaps and semicore binding energies (Luo et al., 2002) as it is capable of taking account nonlocality and dynamic correlations (Oshikiri et al., 1999). The self-energy term from GWA contains information on the electron-electron interaction in terms of the electrostatic Hartree potential and the non-Hermitean, energy dependent and spatially non-local operator (Fleszar et al., 2005). There have been various previous implementations of GWA in studying ZnSe. Self-energy corrections for semicore states were performed by Aryasetiawan (Aryasetiawan et al., 1996). They report accurate results for localized as well as delocalized states especially to experimental binding energies. Nevertheless, there is still no agreement against systems with strong Coulomb correlation effects (Kharazanov et al., 2007). Fleszar (Fleszar et al., 2005) compared the RPA self-energy with the plasmon pole model for the binding energies of cation semicore d-states and observed that the PPM causes the GW energy gaps to get larger, the semicore states to be more bound and the occupied bandwidths to undergo an opposite shift. Plasmon-pole models have a frequency dependence in screening which makes the calculations significantly more efficient where only the response matrices at zero frequency is calculated instead of a dense mesh of frequencies. The self-energy integration was performed analytically. Luo (Luo et al., 2002) also applied a generalized PPM to obtain frequency dependent dielectric matrices to construct the screened Coulomb interaction. Oshkiri (Oshikiri et al., 1999) applied the random phase approximation (RPA) where the exchange correlation corrections to electron excitation energies are taken into account via non-local energy dependent and non-Hermitean self-energy operator. They observed that the RPA overscreens and lowers 3*d* semicore binding energy. Zakharov (Zakharov et al., 1994) applied the Levine-Louie model dielectric function as input to the GWA and observed that the corrections to conduction bands have more complicated character than corrections to valence bands.

4.3.1 Band Energies

In this work, we firstly compared our ground state and excited state band structure with previous results. We observe that relatively good agreement is reached with previous studies for band energies below the Fermi energy. Bands above the Fermi energy do not show much difference transitioning from LDA to GWA compared to previous studies. This may be attributed to the various methodologies and basis sets to obtain the band energies in previous studies. The LDA band gap in this present study is in agreement with LDA calculation of previous studies while the GWA band gap is in agreement with other one shot GWA studies such as that by (Chen et al., 2014) and Fleszar (Fleszar et al., 2005). We then proceed to obtain the spectral function and momentum distributions. We have used a scissors shift of the magnitude 1.3 eV on the Fermi energy of our calculation which was -1.7885 eV to obtain the spectral functions and momentum densities. With the momentum distributions, we then proceed to obtain the Compton profile. From the outset, the GWA profiles seems to be in better agreement compared to the LDA profile. This is confirmed in our study on the difference profiles which we compared with the experimental and theoretical results of Ahuja (Ahuja et al., 2007).

Table 5.2: Comparison of LDA and GWA band energies from our present study with previous studies over three high symmetry *k*-points.

Band energies												
	Present Study		Gurel			Zakharov		Fleszar			Oshkiri	
Band energies	LDA	GWA	MBJ LDA	GGA (PBE)	Theory & Exp	LDA	GWA	LDA	GWA	GW-psp	LDA	GWA
G1v	-12.491	-16.31	-13.02	-13.27	-13.49	-12.92	-13.49	-13.23	-12.9	-13.66	-13.42	-13.27
G15v	-5.5182	-4.23						-6.69	-7.3	-7.42	-7.02	-8.82
G12d	-5.5182	-4.23						-6.33	-6.98	-7.04	-6.72	-8.75
G15v	0	0	0	0	0	0	0	0	0	0	0	0
G1c	1.8677	1.915	2.67	1.26	2.84	1.45	2.84	1.02	2.37	2.46	1.07	3.1
G15c	6.33995	6.409	6.5	5.79	7.67	6.12	7.67				5.85	7.95
L1v	-11.7	-17.35	-12.28	-12.49	-12.44	-11.88	-12.44	-12.15	-12.15	-12.8		
L1v	-5.3691	-4.868	-4.85	-5.23	-5.23	-4.92	-5.23	-5.12	-5.12	-5.6		
L3v	-0.0367	-2.008	-0.79	-0.87	-0.81	-0.76	-0.81	-0.88	-0.88	-0.94		
L1c	3.10984	3.749	3.61	2.52	4.14	2.74	4.14					
L3c	6.95926	7.962	6.91	6.4	8.18	6.63	8.18	2.31	3.68	3.76		
X1v	-11.432	-25.911	-12.02	-12.21	-12.07	-11.52	-12.07	-12.15	-11.89	-12.51		
X3v	-4.02	-6.4	-4.38	-4.77	-5.03	-4.7	-5.03	-4.86	-4.79	-5.09		
X5v	-1.3698	-4.04	-2.03	-2.19	-2.08	-1.96	-2.08	-2.2	-2.2	-2.38		
X1c	3.57541	3.505	3.78	3	4.41	3.09	4.41	2.79	3.92	3.94		
X3c	4.02628	4.089	4.25	3.47	5.01	3.64	5.01					

They obtained the Compton profile from LDA, GGA and B3LYP functionals where an effective core pseudopotential was used to obtain the valence electron calculation with the Bloch states consisting of Zn *d* and Se *sp* components. In our work, we observe between 0-1.5 a.u, there is *a* better agreement to the previous study via the GWA difference profile compared to the LDA difference profile. Above, 1.5 a.u, both cases show no agreement with the previous study. We conclude that improvement to the pseudopotential technique to obtain the Compton profile is possible if the sharp Fermi break of the momentum distribution between *a* high and low momenta becomes more smeared. Using the broadened spectral functions via the contour deformation method to obtain the momentum distributions, the GWA is natural tool to achieve this via the contribution from the dielectric screening to the quasiparticle energies.

The physical properties of ZnSe can be determined by initalizing localized semicore d electrons with valence sp electrons (Rocquefelte et al., 2005). In comparison to previous calculations (Zakharov et al., 1994; Ahuja et al., 2007), we have determined that the valence bands account for the 7th, 8th and 9th bands. We present the band structure and partial density of states (PDOS) in Figure 1. These bands are accounted by three regions as seen in the PDOS. The first region is in the range of -3 to 0.2 eV has mainly *p*-orbital components from Zn and Se. The second region is in the range of -5.2 to 3 eV has mainly *p*-orbital components from Se and *s*- and *d*-orbital components from Zn. The third region is in the range -6 to -6.7 eV consists of a well localized Zn 3d contribution with Se *p*-orbital components. Referring to Table 5.2, the present study shows that the lowest energy band for all three high symmetry *k*-points seems to be in agreement in the case of LDA but is almost twice the energy in the case of GWA. However, relatively good agreement is reached with previous studies for bands below the Fermi energy for the Γ point while the X and L points are slightly larger as LDA transitions to GWA.

The energy bands above the Fermi energy does not show much difference transitioning from LDA to GWA compared to previous studies. Differences may be attributed to the various methodologies and basis sets to obtain the band energies. These discrepancies have also been reported in studies involving the GW method where full GW calculations undergo contraction of valence bands while GW-pseudopotential method undergoes expansion of valence bands if compared to LDA (Fleszar et al., 2004). As reported in previous studies (Aryasetiawan et al., 1996; Karazhanov et al., 2006; Fleszar et al., 2004; Luo et al., 2002; Oshkiri et al., 1999), we also observe underbinding of 3*d* orbitals to the top of the valence bands. This hybridization with Se 2*p* bands falsifies band dispersions and reduces band gaps and contradicts XPS findings (Karazhanov et al., 2006). It has been reported by (Zakharov et al., 1994) 3*d* levels included in the valence causes strong *p*-*d* orbital hybridization and is responsible for reduction of gap and appearance of strong 3*d* levels. When Zn 3*d* electrons are placed into the core of the pseudopotential, the top of the VB structures change minimally for LDA and GGA. It is concluded that Zn 3*d* is responsible for the order of states (Karazhanov et al., 2006).

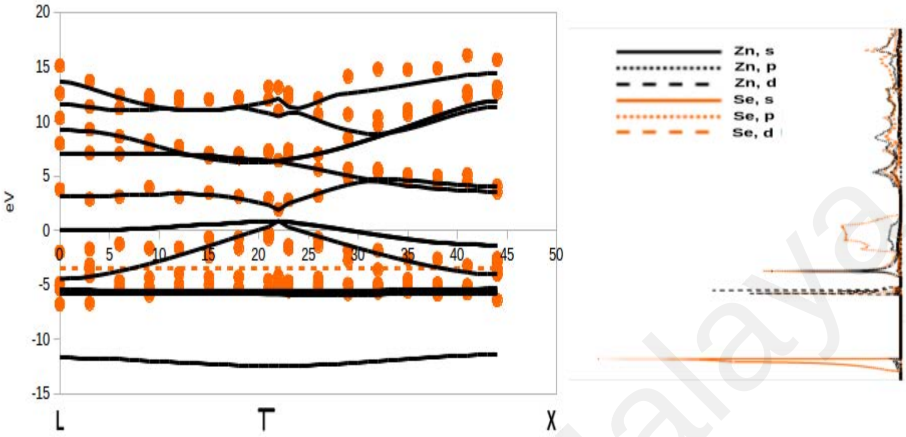

Figure 5.5: Band structure and partial density of states of ZnSe along three high symmetry k-points. The horizontal dashed line represents the Fermi energy.

The calculated gap is obtained from the energy difference between the lowest conduction band and the top of the valence band at the *Γ* point as shown in Table 5.3. The LDA band gap in this present study is in agreement with LDA calculation of previous studies. As has been reported previously, the error in calculation of the band gap using LDA or GGA is more severe in semiconductors due to a poor description of strong Coulomb correlation effects for narrow *d*-band electrons which originates from the mean field character of Kohn-Sham equations (Karazhanov et al.,2007; Karazhanov et al.,2006). The *d*-electrons as valence produces a smaller gap due to *p*-*d* hybridization of upper valence band with *d*-states resulting in upward repulsion causing a reduction in gap (Zakharov et al.,1994). Use of the GGA functional, hybrid functionals and the *U* term seems to increase the band gap but still far from the experimental value.

Table 5.3: Comparison of band gaps of LDA and GWA energies with previous studies.

Band gaps, Ev								
Gurel	MBJLDA	2.67	Oshkiri	GWA	3.1	Madelung	Expt	2.82
	GGA(PBE)	1.26			2.84			
	GGA (PBE+ΔE)	2.82	Gurel	GW	2.24, 2.58			
	LDA(PW)	1.5	Zakharov	GWA	2.84			
	GGA(PBE)	1.47		L3v-L1c, GW	4.95			
Zakharov	LDA	1.45		X5v-X1c,GW	6.49			
Fleszar	LDA	0.88	Fleszar	GWA	2.24			
Luo	GGA	1.32		GW-RPA	2.58			
Chen	PBE	1..23		GW Vertex	2.33			
	PBE(0.25)	2.92		GW-RPA Vertex	2.68			
Rocquefeite	GGA(PBE)	2.69	Luo	GWA	2.51			
Karazhanov	LDA	1.0793		Updated GWA	2.69			
	GGA	1.3349	Chen	GWA(0)	2.28			
	LDA+U	1.4214		GWA(0.25)	3.06			
				QSGW (PBE)	2.56			
				Self-cons. QSGW	3.26			
Present study	LDA	0.983 ± 2.679		GWA	1.915±2.585			

4.3.2 Spectral Functions and Momentum Densities

The quasiparticle shift originates from the competition between the widening effect of the pure exchange part and opposite effect of correlation part of self-energy for the valence band maximum (Fleszar et al., 2004). The contour deformation method agrees with a previous assessment in (Fleszar et al., 2004) where the plasmon pole model creates a larger quasiparticle shift compared to LDA for the valence band maximum (VBM). Our GWA band gap is in agreement with other one shot GWA studies such as that by Chen (Chen et al., 2014) and Fleszar (Fleszar et al., 2004). We agree with previous reports that GW-pseudopotential/GW-RPA with a one shot perturbation still cannot reproduce experimental energies containing semicore electrons (Fleszar et al., 2004). Application of the Quasiparticle Self-consitent GW (QSGW) or Vertex function with RPA seems to increase the band gap closer to experiment.

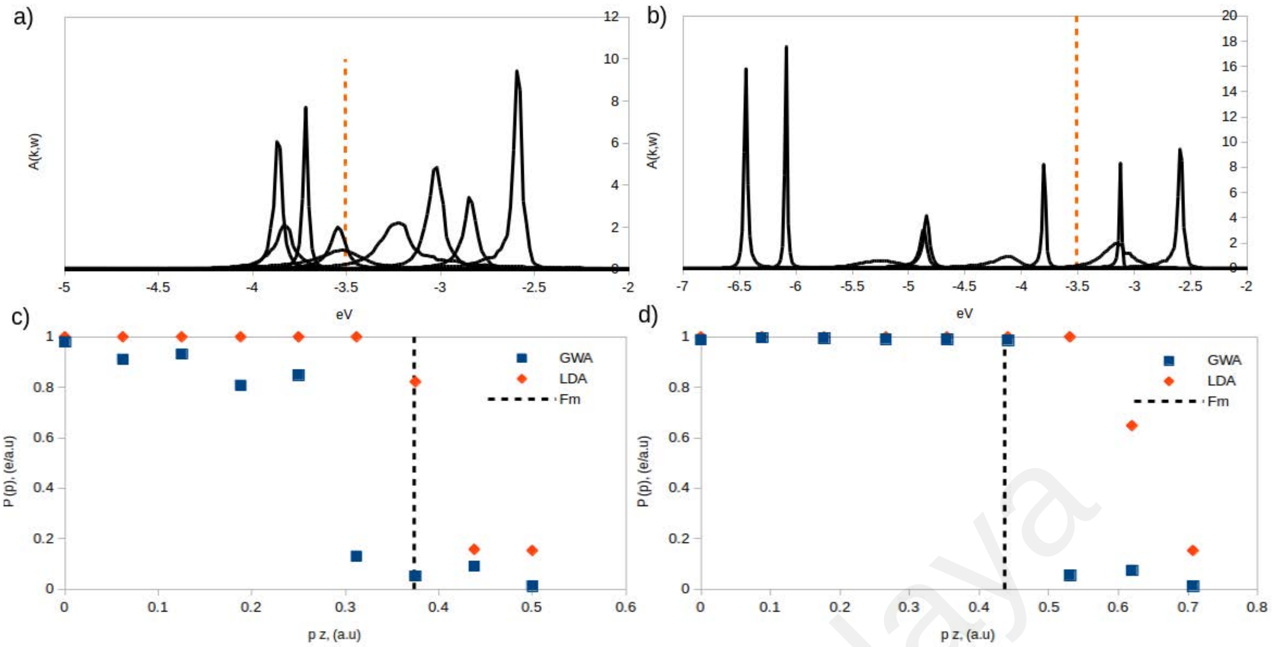

Figure 5.6: (a) and (b) represent spectral functions in directions [100] and [110] respectively. The vertical dotted line represents the Fermi energy of -3.0717 eV. (c) and (d) represent momentum densities obtained from the occupation number and spectral functions for LDA and GWA respectively. We compare these momentum densities to a hypothetical best-fit momentum densities. The vertical dotted lines represent the Fermi momentum at 0.4158 a.u. and 0.5310 a.u. for [100] and [110] respectively.

The scissor operator is the simplest method to correct the LDA band gap. A rigid shift of conduction band states up to experimentally determined locations provide a good first approximation for determining the band gap. However whether a scissor operator is applicable to semiconductors with strong Coulomb correlation effects is still open (Karazhanov et al., 2007). In previous studies, the scissor shift of 1.3 eV for ZnSe-zb was applied to the study of refractive indices of isoelectronic chalcogenides where the conduction band was shifted rigidly with respect to the top of the valence band until the correct band gap was obtained (Rocquefelte et al., 2005). In this work, we have used a shift of 0.9 eV on the Fermi energy of our calculation which was -2.577 eV to obtain the spectral functions as given in Figure 5.6(a) and (b). As described by Olevano (Olevano et al., 2012), we choose the value of the cumulant of the spectral function at the Fermi energy for each calculated k-point to construct the momentum density as shown Figure 5.6 (c) and (d).

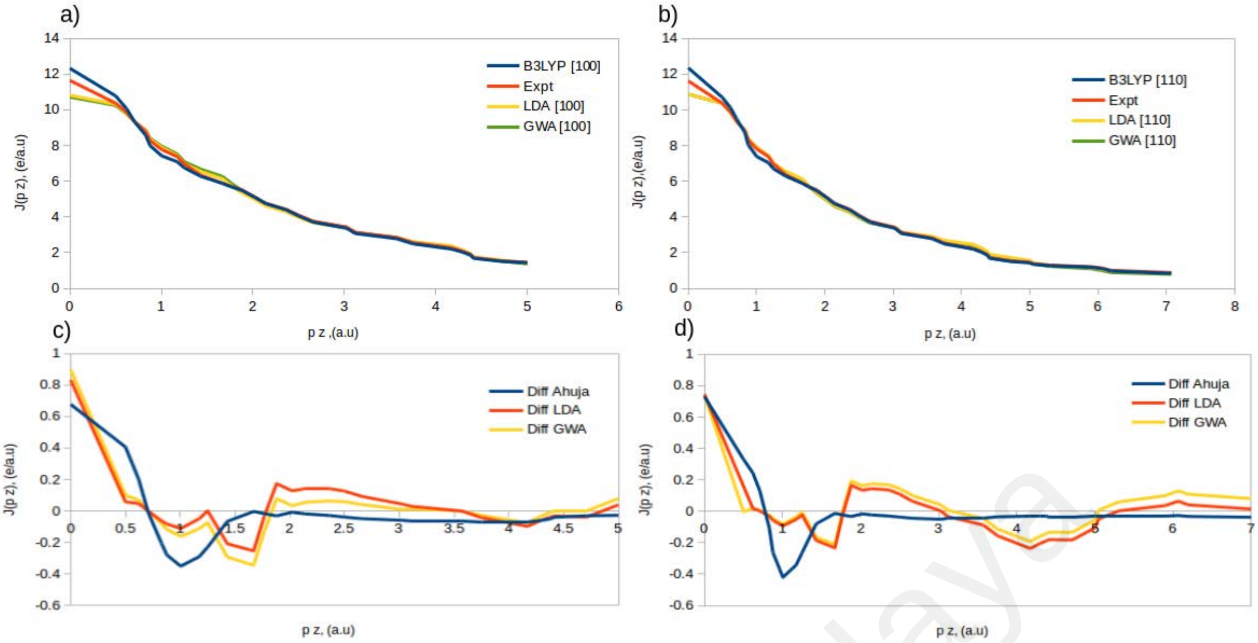

Figure 5.7: (a) and (b) compares the convoluted Compton profile using LDA and GWA energies against experimental and theoretical Compton profiles from a previous study in directions [100] and [110]. (c) and (d) represents the difference profiles in directions [100] and [110].

4.3.3 Compton Profiles

The unconvoluted Compton profile is obtained by firstly fitting the momentum density obtained as described above with the Fermi-Dirac distribution. We then multiply the fitted function with its respective momenta and integrate this result to obtain the unconvoluted profile. We then perform convolution with a Gaussian of 0.38 a.u using Mathematica in order to compare with a previous study by Ahuja (Ahuja et al., 2007). This value represents the resolution function of the instrument normalized to the free atom profile (Vyas et al., 2010). Our convolution is normalized to fit the experimental data for the directions [100] and [110] respectively and is shown in Figure 5.7 (a) and (b).

Compton profile data is interpreted in terms of the difference between pairs of directional profiles (Ahuja et al., 2007). This eliminates residual systematic errors like failure of impulse approximation, Bremstrahlung contribution, multiple scattering and isotropic core contribution. In their study of the difference profiles, Ahuja observes the use of the B3LYP functional gives the best fitting to experiment. We have thus compared their difference profile to the difference profile obtained from comparing our LDA and GWA profiles with their experimental data as shown Figure 5.7 (c) and (d). Between 0-1.5 a.u, both cases seem to improve on the difference profile of Ahuja. There is slightly better agreement via the GWA difference profile compared to the LDA difference profile. Above, 1.5 a.u, the GWA Compton profile generally shows better agreement compared to LDA especially in the direction [100]. Nevertheless, in this range Ahuja's study still shows better agreement to experiment. In previous studies, the difference profiles in this region is said to not change with respect to experiment because the contribution to this momentum region is due to inner electrons unaffected by compound formation (Vyas et al., 2010). Any discrepancies from experiment are related to pseudopotential calculations which have been observed to overestimate momentum density at J(0) while the reverse trend is seen at J(4)-J(1.5) (Ahuja et al., 2007). We thus conclude that improvement to the pseudopotential technique to obtain the Compton profile is possible as the momentum distribution becomes more smeared at the Fermi break between high and low momenta at the cost of the neglecting the sharp Fermi break. The GWA is natural tool to achieve this via the contribution from the dielectric screening to the quasiparticle energies.

CHAPTER 5 : CONCLUSION

In this work, we have performed first principles calculations on crystalline late TMOs, TiO_2 and ZnSe to obtain their respective energies, spectral functions, momentum densities and Compton profiles. For NiO and TiO_2 we have calculated our ground state band gap to be 3.444±2.721 eV and 3.115±0.578 eV while the excited state band gap to be 0.253±4.247 eV and 1.667±1.807 eV for NiO and TiO_2 respectively. In the case of NiO, the excited state band gaps for *k*-points near the origin and at the origin respectively are much smaller compared to ground state calculations. This can be attributed to shortcomings in the GWA to account for d-orbital contributions and the limitations of computational resources as discussed in the text. We have thus opt to apply a scissor operator to shift the energies of the G point as well as the 4 k-points to the left and right of *G* by 4.3 eV in the case of NiO. The valence band energy is observed to have its largest contribution from the TM 3*d* orbital and a small contribution from the O 2*p* orbital. These bands are seen to be strongly localized with a weak dispersion. However, they are not shifted to a lower energy compared to previous works unless a scissor shift is applied. Above the Fermi energy, GWA is seen to push the *d*-orbitals and 4*s* state to a slightly higher energy. Similarly, the valence energies of TiO_2 are seen to have a hybridized contribution between TM *d*-orbitals, O *p*-orbitals and a small contribution from Ti *p*-orbitals. After obtaining the Fermi energy and momenta, we then present the spectral function of these oxides. Our spectral functions for NiO are broadened and contains shoulder similar to what has been observed in earlier studies. This is in contrast to TiO_2 which does not have broadened spectra. This is attributed to the smaller contribution of *d*-orbital to TiO_2 for the valence energies compared to NiO. With the spectral functions, we can proceed to obtain the momentum densities. We explain the shape of the momentum density of NiO in terms of the cumulant functions which are obtained from the broadened spectral functions as oppose to TiO_2 which have Dirac-delta like spectral functions. This shows the importance played by the self-energy from a GWA calculation to shape the momentum densities of two different TMO systems. In comparing the LDA and GWA momentum densities, the GWA NiO momentum density is seen to be 17 % smaller compared to the LDA in the lower momentum region. In the high momentum region, the GWA TiO_2 momentum density is much smaller compared to LDA. With these two types of momentum densities we can now perform a comparison of their Compton profiles to previous studies. NiO is observed to generally have a good fit with previous experimental results. However, a larger disagreement in GWA compared to LDA is observed in the origin of the difference profiles. This can be improved with an increased resolution of *k*-points. Nevertheless, the sum of absolute values of the difference profiles is smaller in the case of GWA compared to LDA indicating generally better agreement. Its anisotropy agrees with previous experimental results in which submaxima structure is non-existent. For TiO_2, we observe that the GWA reproduces a smaller difference profile at higher momenta compared to LDA. Our profile agrees with previous results at lower momenta with a disagreement seen at the origin. We conclude by observing that our QPRF indicates that the correlation portion of the self-energy is more significant in NiO compared to TiO_2.

In our study of NiO, CoO and FeO, we similarly observed that the excited state band gaps are much smaller for *k*-points near the origin compared to the ground state band gaps. We thus applied a scissor shift to these *k*-points to improve agreement with the experimental band gaps. We observe that NiO can produce a larger band gap compared to FeO and CoO via GWA. All oxides show broad valence band shoulders but disagree with the valence band energies of previous calculations with the scissor operator. With the Fermi energy and momenta we obtained the spectral functions of these oxides. We observe that NiO has twice braodened spectra compared to FeO and CoO. This has been attributed to the twice larger *d*-orbital contribution as observed in the partial density of states. With the spectral functions, then proceed to construct the momentum density. For the cause of FeO and CoO, we have firstly improved on the lowered density near the Fermi break by fitting the spectral functions of these *k*-points to a Lorentzian. Our momentum densities show difference to the noninteracting electron gas where we observe occupancy above the Fermi break attributed to the GWA. The NiO momentum density is more occupied in the low momentum region compared to FeO and CoO and this confirms the role of NiO as a strongly correlated system. With the momentum density, we can proceed to construct the Compton profile. GWA and LDA Compton profile are seen to generally not show any difference. However, the difference profile reveals that in the direction [001], the correlation correction is smaller in the low momenta compared to [101] while the higher momenta goes to zero. This is similarly attributed to a larger *d*-orbital contribution along [001] as observed in the partial density of states. The large fluctuation at the intermediate level in both directions reflect that the self-energy has a large effect in this region. Our anisotropy does not reflect oscillatory structures as compared to previous studies. However the amplitude of the anisotropy of NiO is seen to be larger than FeO and CoO. This is attributed to asymmetry of valence electron profiles induced by spectral functions and vertex corrections.

In our study of ZnSe, we firstly compared our ground state and excited state band structure with previous results. We observe that relatively good agreement is reached with previous studies for band energies below the Fermi energy. Bands above the Fermi energy do not show much difference transitioning from LDA to GWA compared to previous studies. This may be attributed to the various methodologies and basis sets to obtain the band energies in previous studies. The LDA band gap in this present study is in agreement with LDA calculation of previous studies while the GWA band gap is in agreement with other one shot GWA studies. Specifically we have calculated our ground state band gap to be 0.983±2.679 eV while the excited state band gap to be 1.915±2.585 eV. We then proceed to obtain the spectral function and momentum distributions. We have used a scissors shift of the magnitude 1.3 eV on the Fermi energy of our calculation which was -1.7885 eV to obtain the spectral functions and momentum densities. With the momentum distributions, we then proceed to obtain the Compton profile. From the outset, the GWA profiles seems to be in better agreement compared to the LDA profile. This is confirmed in our study on the difference profiles which we compared with the previous experimental and theoretical results. They obtained the Compton profile from LDA, GGA and B3LYP functionals where an effective core pseudopotential was used to obtain the valence electron calculation with the Bloch states consisting of Zn *d* and Se *sp* components. In our work, we observe between 0-1.5 a.u, there is better agreement to the previous study via the GWA difference profile compared to the LDA difference profile. Above, 1.5 a.u, both cases show no agreement with the previous study. We conclude that improvement to the pseudopotential technique to obtain the Compton profile is possible if the sharp Fermi break of the momentum distribution between high and low momenta becomes more smeared. Using the broadened spectral functions via the contour deformation method to obtain the momentum distributions, the GWA is natural tool to achieve this via the contribution from the dielectric screening to the quasiparticle energies.

Our work has shown that the GWA contour deformation method with the scissor shift to calculate calculate Compton profiles is able to provide better agreement to previous experimental results compared to ground state calculations. This is specifically attributed to the broadening of the spectral function used to obtain the Compton profiles. With this broadening and results from the projected density of states, we are able to explicitly determine angular momentum orbital contribution to Compton profiles. A future endeavor might consist of applying muffin tin or projector augmented wave basis sets which have been shown to be computationally cheaper to obtain the band energies and spectral functions.

REFERENCES

Adamo, C., & Barone, V. (1999). Toward reliable density functional methods without adjustable parameters: The PBE0 model. *The Journal of Chemical Physics, 110*(13), 6158-6170.

Adler, S. L. (1962). Quantum theory of the dielectric constant in real solids. *Physical Review, 126*(2), 413-417.

Aguiar, J. C., Mitnik, D., & Di Rocco, H. O. (2015). Electron momentum density and Compton profile by a semi-empirical approach. *Journal of Physics and Chemistry of Solids, 83*, 64-69.

Ahuja, B. L., & Heda, N. L. (2007). Electron momentum density in ZnSe: Theory and experiment. *Radiation Physics and Chemistry, 76*(6), 921-928.

Akinaga, H., & Shima, H. (2010). Resistive random access memory (ReRAM) based on metal oxides. *Proceedings of the IEEE, 98*(12), 2237-2251.

Anastassopoulos, D. L., Priftis, G. D., Papanicolaou, N. I., & Bacalis, N. C. (1991). Calculation of the electron momentum density and Compton scattering measurements for nickel. *Journal of Physics: Condensed Matter, 3*(9), 1099-1104.

Anisimov, V. I. (2000). Strong coulomb correlations in electronic structure calculations. CRC Press.

Aryasetiawan, F., & Gunnarsson, O. (1994). Product-basis method for calculating dielectric matrices. *Physical Review B, 49*(23), 16214-16218.

Aryasetiawan, F., & Gunnarsson, O. (1995). Electronic structure of NiO in the GW approximation. *Physical Review Letters, 74*(16), 3221-3225.

Aryasetiawan, F., & Gunnarsson, O. (1996). 3 d semicore states in ZnSe, GaAs, and Ge. *Physical Review B, 54*(24), 17564-17568.

Aryasetiawan, F., & Gunnarsson, O. (1998). The GW method. *Reports on Progress in Physics, 61*(3), 237-241.

Aryasetiawan, F., & Karlsson, K. (1996). GW spectral functions of Gd and NiO. *Physical Review B, 54*(8), 5353-5357.

Aulbur, W. G., Jönsson, L., & Wilkins, J. W. (1999). Quasiparticle calculations in solids. *Solid State Physics*, *54,* 1-218.

Azaroff, L. V., Kaplow, R., Kato, N., Weiss, R. J., Wilson, A. J. C., & Young, R. A. X-ray Diffraction, 1974.

Bader, R. F. (1990). Atoms in molecules: a quantum theory, vol 22, International series of monographs on chemistry.

Bansil, A., & Kaprzyk, S. (1997). *High Resolution Compton Scattering: A New Probe of Fermiology and Electron Correlation Effects.* In Materials Science Forum (Vol. 255, pp. 129-134). Trans Tech Publications.

Barbiellini, B. (2000). A natural orbital method for the electron momentum distribution in matter. *Journal of Physics and Chemistry of Solids*, *61*(3), 341-344.

Barbiellini, B. (2014). Natural orbital functional theory and pairing correlation effects in electron momentum density. *Low Temperature Physics*, *40*(4), 318-322.

Barbiellini, B., & Bansil, A. (2004). Dyson orbitals, quasi-particle effects and Compton scattering. *Journal of Physics and Chemistry of Solids, 65*(12), 2031-2034.

Barnes, S. E. (1991). Theory of positron annihilation in the spinon-holon picture. *Journal of Physics and Chemistry of Solids, 52*(11), 1525-1533.

Baruah, T., Zope, R. R., & Kshirsagar, A. (1999). Full-potential LAPW calculation of electron momentum density and related properties of Li. *Physical Review B, 60*(15), 10770-10774.

Bechstedt, F., Del Sole, R., Cappellini, G., & Reining, L. (1992). An efficient method for calculating quasiparticle energies in semiconductors. *Solid State Communications*, *84*(7), 765-770.

Becke, A. D., & Edgecombe, K. E. (1990). A simple measure of electron localization in atomic and molecular systems. *The Journal of Chemical Physics*, *92*(9), 5397-5403.

Björkman, T. (2011). CIF2Cell: Generating geometries for electronic structure programs. *Computer Physics Communications, 182*(5), 1183-1186.

Bourke, J. D., & Chantler, C. T. (2012). Electron energy loss spectra and overestimation of inelastic mean free paths in many-pole models. *The Journal of Physical Chemistry A, 116*(12), 3202-3205.

Bourke, J. D., & Chantler, C. T. (2015). Momentum-dependent lifetime broadening of electron energy loss spectra: a self-consistent coupled-plasmon model. *The Journal of Physical Chemistry Letters, 6*(3), 314-319.

Bostwick, A., Speck, F., Seyller, T., Horn, K., Polini, M., Asgari, R., ... & Rotenberg, E. (2010). Observation of plasmarons in quasi-freestanding doped graphene. *Science*, *328*(5981), 999-1002.

Bross, H. (2004). The local density approximation limit of the momentum density and the Compton profiles of Al. J*ournal of Physics: Condensed Matter, 16*(41), 7363-7367.

Bruneval, F. (2009). GW Approximation of the Many-Body Problem and Changes in the Particle Number. *Physical Review Letters*, *103*(17), 176403-176407.

Cardwell, D. A., & Cooper, M. J. (1989a). The effect of exchange and correlation on the agreement between APW and LCAO Compton profiles and experiment. *Journal of Physics: Condensed Matter, 1*(47), 9357-9361.

Cardwell, D. A., Cooper, M. J., & Wakoh, S. (1989b). Compton scattering studies of electron correlation effects in chromium. *Journal of Physics: Condensed Matter, 1(*3), 541-545.

Carlsson, G. A., Carlsson, C. A., Berggren, K. F., & Ribberfors, R. (1982). Calculation of scattering cross sections for increased accuracy in diagnostic radiology. I. Energy broadening of Compton scattered photons. *Medical physics, 9*(6), 868-879.

Chadi, D. J., & Cohen, M. L. (1973). Special points in the Brillouin zone. *Physical Review B, 8*(12), 5747-5751.

Chen, W., & Pasquarello, A. (2014). Band-edge positions in G W: Effects of starting point and self-consistency. *Physical Review B, 90*(16), 165133-165137.

Chiba, T., & Tsuda, N. (1974). Anisotropy in the angular correlation curves of NiO. *Applied Physics*, *5*(1), 37-40.

Christensen, N. E. (1978). Spin-orbit projected d densities-of-states of Pd, Ag, Pt, and Au. *Journal of Physics F: Metal Physics, 8*(3), L51-55.

Clementi, E. (1965). Tables of atomic functions. *IBM Journal of Research and Development*, *9*(1), 87-89.

Cooper, M. J. (1985). Compton scattering and electron momentum determination. *Reports on Progress in Physics*, *48*(4), 415-419.

Cooper, M. J., Cooper, M., Mijnarends, P. E., Mijnarends, P., Shiotani, N., Sakai, N., & Bansil, A. (2004). *X-ray Compton scattering* (No. 5). Oxford University Press on Demand.

Cracknell, A. P. (1975). *Group theory in solid-state physics*. Halsted Press.

Csanak, G., Taylor, H. S., & Yaris, R. (1971). Green's function technique in atomic and molecular physics. *Advances in Atomic and Molecular Physics*, *7*, 287-361.

Curtarolo, S., Setyawan, W., Hart, G. L., Jahnatek, M., Chepulskii, R. V., Taylor, R. H., ... & Mehl, M. J. (2012). AFLOW: An automatic framework for high-throughput materials discovery. *Computational Materials Science, 58*, 218-226.

Das, S., Coulter, J. E., & Manousakis, E. (2015). Convergence of quasiparticle self-consistent G W calculations of transition-metal monoxides. *Physical Review B, 91*(11), 115105-115109.

Faleev, S. V., Van Schilfgaarde, M., & Kotani, T. (2004). All-Electron Self-Consistent G W Approximation: Application to Si, MnO, and NiO. *Physical Review Letters, 93*(12), 126406-126410.

Fleszar, A., & Hanke, W. (2005). Electronic structure of II B− VI semiconductors in the GW approximation. *Physical Review B, 71*(4), 045207-045211.

Friedrich, C., & Schindlmayr, A. (2006). Many-body perturbation theory: The GW approximation. *NIC Series*, 31, 335-339.

Fuchs, M., & Scheffler, M. (1999). Ab initio pseudopotentials for electronic structure calculations of poly-atomic systems using density-functional theory. *Computer Physics Communications, 119*(1), 67-98.

Fukamachi, T., Hosoya, S., Iway, K., & Hayakawa, K. (1973). Anisotropy of Compton profile found in nickel oxide single crystal. *Physics Letters A*, *42*(7), 477-478.

Galamić-Mulaomerović, S., & Patterson, C. H. (2005). Band structures of rare-gas solids within the GW approximation. *Physical Review B, 71*(19), 195103-195108.

Georges, A., Kotliar, G., Krauth, W., & Rozenberg, M. J. (1996). Dynamical mean-field theory of strongly correlated fermion systems and the limit of infinite dimensions. *Reviews of Modern Physics, 68*(1), 13-113.

Godby, R. W., & Needs, R. J. (1989). Metal-insulator transition in Kohn-Sham theory and quasiparticle theory. *Physical Review Letters, 62*(10), 1169-1173.

Goedecker, S., Teter, M., & Hutter, J. (1996). Separable dual-space Gaussian pseudopotentials. *Physical Review B, 54*(3), 1703-1707.

Gonze, X., Amadon, B., Anglade, P. M., Beuken, J. M., Bottin, F., Boulanger, P., ... & Deutsch, T. (2009). ABINIT: First-principles approach to material and nanosystem properties. *Computer Physics Communications, 180*(12), 2582-2615.

Gonze, X., Beuken, J. M., Caracas, R., Detraux, F., Fuchs, M., Rignanese, G. M., ... & Torrent, M. (2002). First-principles computation of material properties: the ABINIT software project. *Computational Materials Science, 25*(3), 478-492.

Grüneis, A., Kresse, G., Hinuma, Y., & Oba, F. (2014). Ionization potentials of solids: the importance of vertex corrections. *Physical Review Letters*, *112*(9), 096401-096405.

Gürel, H. H., Akinci, Ö., & Ünlü, H. (2012). First principles calculations of Cd and Zn chalcogenides with modified Becke–Johnson density potential. *Superlattices and Microstructures, 51*(5), 725-732.

GW/BSE Fiesta code. (n.d.). Retrieved October 26, 2016, from http://perso.neel.cnrs.fr/xavier.blase/fiesta/index.html

Gygi, F., & Baldereschi, A. (1986). Self-consistent Hartree-Fock and screened-exchange calculations in solids: Application to silicon. *Physical Review B, 34*(6), 4405-4409.

Hamada, N., Hwang, M., & Freeman, A. J. (1990). Self-energy correction for the energy bands of silicon by the full-potential linearized augmented-plane-wave method: Effect of the valence-band polarization. *Physical Review B, 41*(6), 3620-3624.

Hawkes, D. J., & Jackson, D. F. (1980). An accurate parametrisation of the x-ray attenuation coefficient. *Physics in Medicine and Biology*, *25*(6), 1167-1171.

Hedin, L. (1965). New method for calculating the one-particle Green's function with application to the electron-gas problem. *Physical Review, 139*(3A), A796-800.

Hedin, L. (1999). On correlation effects in electron spectroscopies and the GW approximation. *Journal of Physics: Condensed Matter, 11*(42), R489-493.

Hedin, L., & Lundqvist, S. (1970). Effects of electron-electron and electron-phonon interactions on the one-electron states of solids. *Solid State Physics*, *23*, 1-181.

Heisenberg, W. (1925). Quantum-theoretical re-interpretation of kinematic and mechanical relations. *Zeitschrift für Physik, 33*, 879-893.

Held, K., Taranto, C., Rohringer, G., & Toschi, A. (2011). Hedin Equations, GW, GW+ DMFT, and all that: *The LDA+ DMFT approach to strongly correlated materials*. Retrieved from https://arxiv.org/pdf/*1109.3972*

Heyd, J., Scuseria, G. E., & Ernzerhof, M. (2003). Hybrid functionals based on a screened Coulomb potential. *The Journal of Chemical Physics, 118*(18), 8207-8215.

Hohenberg, P., & Kohn, W. (1964). Inhomogeneous electron gas. *Physical Review, 136(*3B), B864-B870.

Holm, B., & von Barth, U. (1998). Fully self-consistent GW self-energy of the electron gas. *Physical Review B, 57*(4), 2108-2112.

Huefner, M., Ghosh, R. K., Freeman, E., Shukla, N., Paik, H., Schlom, D. G., & Datta, S. (2014). Hubbard gap modulation in vanadium dioxide nanoscale tunnel junctions. *Nano Letters*, *14*(11), 6115-6120.

Huotari S, Soininen J A, Pylkkänen T, Hämäläinen K, Issolah A, Titov A, McMinis J, Kim J, Esler K, Ceperley D M and Holzmann M (2010). Momentum distribution and renormalization factor in sodium and the electron gas. *Physical Review Letters*, *105*(8), 086403-086407.

Huotari, S., Hämäläinen, K., Manninen, S., Kaprzyk, S., Bansil, A., Caliebe, W., ... & Suortti, P. (2000). Energy dependence of experimental Be Compton profiles. *Physical Review B, 62*(12), 7956-7960.

Huotari, S., Sternemann, C., Volmer, M., Soininen, J. A., Monaco, G., & Schülke, W. (2007). High-resolution Compton line shapes: Fermi break of beryllium. *Physical Review B, 76*(23), 235106-235110.

Imada, M., Fujimori, A., & Tokura, Y. (1998). Metal-insulator transitions. *Reviews of Modern Physics, 70*(4), 1039-1043.

Imambekov, A., Schmidt, T. L., & Glazman, L. I. (2012). One-dimensional quantum liquids: Beyond the Luttinger liquid paradigm. *Reviews of Modern Physics, 84*(3), 1253-1257.

Jeong, D. S., Thomas, R., Katiyar, R. S., Scott, J. F., Kohlstedt, H., Petraru, A., & Hwang, C. S. (2012). Emerging memories: Resistive switching mechanisms and current status. *Reports on Progress in Physics*, *75*(7), 076502-076506.

Jiang, H., Gomez-Abal, R. I., Rinke, P., & Scheffler, M. (2010). First-principles modeling of localized d states with the GW@ LDA+U approach. *Physical Review B, 82*(4), 045108-045112.

Jones, R. O., & Gunnarsson, O. (1989). The density functional formalism, its applications and prospects. *Reviews of Modern Physics, 61*(3), 689-693.

Joshi, K. B., & Sharma, B. K. (2007). Electronic structure and momentum density distribution of titanium dioxide. *Journal of Alloys and Compounds, 440*(1), 51-56.

Karazhanov, S. Z., Ravindran, P., Kjekhus, A., Fjellvåg, H., Grossner, U., & Svensson, B. G. (2006). Electronic structure and band parameters for ZnX (X= O, S, Se, Te). *Journal of Crystal Growth, 287*(1), 162-168.

Karazhanov, S. Z., Ravindran, P., Kjekshus, A., Fjellvåg, H., & Svensson, B. G. (2007). Electronic structure and optical properties of Zn X (X= O, S, Se, Te): A density functional study. *Physical Review B, 75*(15), 155104-155108.

Kleinman, L., & Bylander, D. M. (1982). Efficacious form for model pseudopotentials. *Physical Review Letters, 48(*20), 1425-1429.

Kohn, W., & Sham, L. J. (1965). Self-consistent equations including exchange and correlation effects. *Physical Review, 140*(4A), A1133-1137.

Králik, B., Delaney, P., & Louie, S. G. (1998). Correlation effects in the Compton profile of silicon. *Physical Review Letters, 80*(19), 4253-4257.

Kubo, Y. (2001). Electron correlation effects on Compton profiles of Cr in the GW approximation. *Journal of Physics and Chemistry of Solids*, *62*(12), 2199-2203.

Kubo, Y. (2004). Electron correlation effects on magnetic Compton profiles of nickel in the GW approximation. *Journal of Physics and Chemistry of Solids*, *65*(12), 2077-2082.

Kubo, Y. (2005). Electron correlation effects on Compton profiles of copper in the GW approximation. *Journal of Physics and Chemistry of Solids*, *66*(12), 2202-2206.

Kubo, Y. (1996). Compton profiles of Li in the GW approximation. *Journal of the Physical Society of Japan, 65*(1), 16-18.

Kubo, Y. (1997). Effects of electron correlations on Compton profiles of Li and Na in the GW approximation. *Journal of the Physical Society of Japan, 66*(8), 2236-2239.

Lam, L., & Platzman, P. M. (1974). Momentum density and Compton profile of the inhomogeneous interacting electronic system. I. Formalism. *Physical Review B, 9*(12), 5122.

Lany, S. (2013). Band-structure calculations for the 3 d transition metal oxides in G W. *Physical Review B, 87*(8), 085112-085116.

Lebègue, S., Arnaud, B., Alouani, M., & Bloechl, P. E. (2003). Implementation of an all- electron GW approximation based on the projector augmented wave method without plasmon pole approximation: Application to Si, SiC, AlAs, InAs, NaH, and KH. *Physical Review B, 67*(15), 155208-155212.

Li, J. L., Rignanese, G. M., & Louie, S. G. (2005). Quasiparticle energy bands of NiO in the G W approximation. *Physical Review B, 71*(19), 193102-193106.

Limandri S. P., Fadanelli R. C., Behar M., Nagamine L. C., Fernández-Varea J. M., Abril I., Garcia-Molina R., Montanari C. C., Aguiar J. C., Mitnik D. and Miraglia J. E. (2014). Stopping cross sections of TiO_2 for H and He ions. *The European Physical Journal D, 68*(7), 194-198.

Lundqvist, B. I., & Lydén, C. (1971). Calculated momentum distributions and Compton profiles of interacting conduction electrons in lithium and sodium. *Physical Review B, 4*(10), 3360-3364.

Luo, W., Ismail-Beigi, S., Cohen, M. L., & Louie, S. G. (2002). Quasiparticle band structure of ZnS and ZnSe. *Physical Review B, 66*(19), 195215-195219.

Luttinger, J. M. (1960). Fermi surface and some simple equilibrium properties of a system of interacting fermions. *Physical Review, 119*(4), 1153-1157.

Makkonen, I., Hakala, M., & Puska, M. J. (2005). Calculation of valence electron momentum densities using the projector augmented-wave method. *Journal of Physics and Chemistry of Solids, 66*(6), 1128-1135.

Manninen, S., & Paakkari, T. (1991). Anisotropy in the electron momentum distribution of silver. *Physical Review B, 44*(7), 2928-2932.

Martens K., Radu I. P., Mertens S., Shi X., Nyns L., Cosemans S., Favia P., Bender H., Conard T., Schaekers M., & De Gendt S. (2012). The VO2 interface, the metal-insulator transition tunnel junction, and the metal-insulator transition switch On-Off resistance. *Journal of Applied Physics*, *112*(12), 124501-124505.

Marzari, N. (1996). *Ab-initio molecular dynamics for metallic systems.* (Doctoral dissertation). University of Cambridge.

Marzari, N., Vanderbilt, D., & Payne, M. C. (1997). Ensemble density-functional theory for ab initio molecular dynamics of metals and finite-temperature insulators. *Physical Review Letters, 79*(7), 1337-1340.

Marzari, N., Vanderbilt, D., De Vita, A., & Payne, M. C. (1999). Thermal contraction and disordering of the Al (110) surface. *Physical Review Letters, 82*(16), 3296-3300.

Massidda, S., Continenza, A., Posternak, M., & Baldereschi, A. (1997). Quasiparticle energy bands of transition-metal oxides within a model GW scheme. *Physical Review B, 55*(20), 13494-13499.

Matsumoto, I., Kwiatkowska, J., Maniawski, F., Bansil, A., Kaprzyk, S., Itou, M., ... & Shiotani, N. (2000). A Compton scattering study of an Al–Li disordered alloy single crystal. *Journal of Physics and Chemistry of Solids, 61*(3), 375-378.

Mattuck, R. D. (2012). *A guide to Feynman diagrams in the many-body problem.* (2nd Ed). Courier Corporation.

Methfessel, M. P. A. T., & Paxton, A. T. (1989). High-precision sampling for Brillouin-zone integration in metals. *Physical Review B, 40*(6), 3616-3620.

Migdal, A. B. (1957). The momentum distribution of interacting Fermi particles. *Soviet Physics. Journal of Experimental and Theoretical Physics, 32*, *399*-400.

Monkhorst, H. J., & Pack, J. D. (1976). Special points for Brillouin-zone integrations. *Physical Review B, 13*(12), 5188-5192.

Ng, T. K., & Dabrowski, B. (1986). Off-shell self-energy effects and the dynamic structure factor of an electron liquid. *Physical Review B, 33*(8), 5358-5362.

O'regan, B., & Grätzel, M. (1991). A low-cost, high-efficiency solar cell based on dye-sensitized colloidal TiO_2 films. N*ature*, *353*(6346), 737-741.

Ohata, T., Itou, M., Matsumoto, I., Sakurai, Y., Kawata, H., Shiotani, N., ... & Bansil, A. (2000). High-resolution Compton scattering study of the electron momentum density in Al. *Physical Review B, 62*(24), 16528-16532.

Olevano, V., Titov, A., Ladisa, M., Hämäläinen, K., Huotari, S., & Holzmann, M. (2012). Momentum distribution and Compton profile by the ab initio GW approximation. *Physical Review B*, *86*(19), 195123-195127.

Onida, G., Reining, L., & Rubio, A. (2002). Electronic excitations: density-functional versus many-body Green's-function approaches. *Reviews of Modern Physics, 74*(2), 601-605.

Onodera, Y. (1973). Microscopic Dielectric Constant in Insulators. *Progress of Theoretical Physics, 49*(1), 37-45.

Oshikiri, M., & Aryasetiawan, F. (1999). Band gaps and quasiparticle energy calculations on ZnO, ZnS, and ZnSe in the zinc-blende structure by the GW approximation. *Physical Review B, 60*(15), 10754-10759.

Payne, M. C., Teter, M. P., Allan, D. C., Arias, T. A., & Joannopoulos, J. D. (1992). Iterative minimization techniques for ab initio total-energy calculations: molecular dynamics and conjugate gradients. *Reviews of Modern Physics, 64*(4), 1045-1049.

Peng, H. Y., Li, Y. F., Lin, W. N., Wang, Y. Z., Gao, X. Y., & Wu, T. (2012). Deterministic conversion between memory and threshold resistive switching via tuning the strong electron correlation. *Scientific Reports, 2*, 442-446.

Peter, M., Jarlborg, T., Manuel, A. A., & Barbiellini, B. (1993). What can positrons contribute to high-Tc superconductivity?. *Zeitschrift für Naturforschung A, 48*(1-2), 390-397.

Platzman, P. M. (1974). Inelastic X-Ray Scattering from Electrons in Matter. In *Elementary Excitations in Solids, Molecules, and Atoms* (pp. 31-64). Boston, Massachusetts: Springer .

Platzman, P. M., & Tzoar, N. (1970). Magnetic scattering of x rays from electrons in molecules and solids. *Physical Review B, 2*(9), 3556-3560.

Prange, M. P., Rehr, J. J., Rivas, G., Kas, J. J., & Lawson, J. W. (2009). Real space calculation of optical constants from optical to x-ray frequencies. *Physical Review B, 80(15), 155110-155114.*

Pyykko, P. (2011). The physics behind chemistry and the periodic table. *Chemical Reviews, 112*(1), 371-384.

Pyykkö, P., Tokman, M., & Labzowsky, L. N. (1998). Estimated valence-level Lamb shifts for group 1 and group 11 metal atoms. *Physical Review A, 57*(2), R689-693.

Rocquefelte, X., Whangbo, M. H., & Jobic, S. (2005). Structural and electronic factors controlling the refractive indices of the chalcogenides ZnQ and CdQ (Q= O, S, Se, Te). *Inorganic Chemistry, 44*(10), 3594-3598.

Rödl, C., & Bechstedt, F. (2012). Optical and energy-loss spectra of the antiferromagnetic transition metal oxides MnO, FeO, CoO, and NiO including quasiparticle and excitonic effects. *Physical Review B, 86*(23), 235122-235126.

Rödl, C., Fuchs, F., Furthmüller, J., & Bechstedt, F. (2009). Quasiparticle band structures of the antiferromagnetic transition-metal oxides MnO, FeO, CoO, and NiO. *Physical Review B, 79*(23), 235114-235119.

Rollason, A. J., Schneider, J. R., Laundy, D. S., Holt, R. S., & Cooper, M. J. (1987). Electron momentum density in nickel. *Journal of Physics F: Metal Physics, 17(*5), 1105-1109.

Sakurai, Y., Tanaka, Y., Bansil, A., Kaprzyk, S., Stewart, A. T., Nagashima, Y., ... & Shiotani, N. (1995). High-resolution Compton scattering study of Li: Asphericity of the Fermi surface and electron correlation effects. *Physical Review Letters, 74(*12), 2252-2256.

Saniz, R., Barbiellini, B., & Denison, A. (2002). Compton scattering, positron annihilation properties of quantum dots. *Physical Review B, 65*(24), 245310-245314.

Schülke, W., Stutz, G., Wohlert, F., & Kaprolat, A. (1996). Electron momentum-space densities of Li metal: A high-resolution Compton-scattering study. *Physical Review B, 54(*20), 14381-14385.

Sharma, S., Dewhurst, J. K., Sanna, A., & Gross, E. K. U. (2011). Bootstrap approximation for the exchange-correlation kernel of time-dependent density-functional theory. *Physical Review Letters, 107*(18), 186401-186405.

Sholl, D., & Steckel, J. A. (2011). *Density functional theory: A practical introduction.* John Wiley & Sons.

Soininen, J. A., Hämäläinen, K., & Manninen, S. (2001). Final-state electron-electron interaction in Compton scattering. *Physical Review B, 64*(12), 125116-125120.

Stefanucci, G., & Van Leeuwen, R. (2013). *Nonequilibrium many-body theory of Quantum Systems: A Modern Introduction*. United Kingdom: Cambridge University Press.

Sternemann C, Hämäläinen K, Kaprolat A, Soininen A, Döring G, Kao C C, Manninen S and Schülke W (2000). Final-state interaction in Compton scattering from electron liquids. *Physical Review B, 62*(12), R7687-R7691.

Sternemann, C., Buslaps, T., Shukla, A., Suortti, P., Döring, G., & Schülke, W. (2001). Temperature influence on the valence Compton profiles of aluminum and lithium. *Physical Review B, 63*(9), 094301-094305.

Strinati, G. (1988). Application of the Green’s functions method to the study of the optical properties of semiconductors. *La Rivista del Nuovo Cimento (1978-1999), 11*(12), 1-86.

Sundararajan, V., Asokamani, R., & Kanhere, D. G. (1988). Anisotropies of Compton profiles in nickel. *Physical Review B, 38*(17), 12653-12657.

Suortti, P., Buslaps, T., Honkimäki, V., Metz, C., Shukla, A., Tschentscher, T., ... & Kheifets, A. S. (2000). Fermi-surface and electron correlation in Al studied by Compton scattering. *Journal of Physics and Chemistry of Solids, 61*(3), 397-401.

Terakura, K., Oguchi, T., Williams, A. R., & Kübler, J. (1984). Band theory of insulating transition-metal monoxides: Band-structure calculations. *Physical Review B, 30*(8), 4734-4738.

Troullier, N., & Martins, J. L. (1991). Efficient pseudopotentials for plane-wave calculations. *Physical Review B, 43*(3), 1993.

Uehling, E. A. (1935). Polarization effects in the positron theory. *Physical Review*, *48*(1), 55-59.

Vinson, J., Rehr, J. J., Kas, J. J., & Shirley, E. L. (2011). Bethe-Salpeter equation calculations of core excitation spectra. *Physical Review B, 83*(11), 115106-115120.

von Barth, U., & Hedin, L. (1972). A local exchange-correlation potential for the spin polarized case. i. *Journal of Physics C: Solid State Physics, 5*(13), 1629-1633.

von Barth, U., & Holm, B. (1996). Self-consistent GW_0 results for the electron gas: Fixed screened potential W 0 within the random-phase approximation. *Physical Review B, 54*(12), 8411-8415.

Vyas, V., & Sharma, B. K. (2010). Study of bonding in ZnSe and CdTe by Compton scattering technique. *Chalcogenide Letters, 7*(5), 325-327.

Wakoh, S., & Matsumoto, M. (1990). Correlation correction on Compton profiles of V and Cr. *Journal of Physics: Condensed Matter, 2*(4), 797-801.

Wakoh, S., Matsumoto, M., & Tokii, M. (2000). Compton profiles of aluminium corrected by the electron correlation effect. *Journal of Physics: Condensed Matter, 12*(47), 9725-9729.

Wiser, N. (1963). Dielectric constant with local field effects included. Physical Review, 129(1), 62.

Wolfram Research, Inc., Mathematica, Version 8.0, Champaign, IL (2010).

Woicik, J. C. (Ed.). (2016). *Hard x-ray photoelectron spectroscopy (HAXPES)*. Heidelberg, New York, Dordrecht, London: Springer.

Yan, J., & Nørskov, J. K. (2013). Calculated formation and reaction energies of 3 d transition metal oxides using a hierarchy of exchange-correlation functionals. *Physical Review B, 88*(24), 245204-245208.

Zakharov, O., Rubio, A., Blase, X., Cohen, M. L., & Louie, S. G. (1994). Quasiparticle band structures of six II-VI compounds: ZnS, ZnSe, ZnTe, CdS, CdSe, and CdTe. *Physical Review B, 50*(15), 10780-10784.

Zhai, H. J., & Wang, L. S. (2007). Probing the electronic structure and band gap evolution of titanium oxide clusters (TiO_2) n-(n= 1-10) using photoelectron spectroscopy. *Journal of the American Chemical Society, 129*(10), 3022-3026.

LIST OF PUBLICATIONS AND PAPERS PRESENTED

1. **Khidzir, S. M.**, Maulida, F., & Wan Abdullah, W. A. T. (2017). GW approximation study of the Compton profile of ZnSe. *Radiation Effects and Defects in Solids*, *172*(7-8), 664-677.
2. **Khidzir, S. M.**, Halid, M. F. M., & Abdullah, W. W. (2016). Compton profiles of NiO and TiO_2 obtained from first principles GWA spectral function. *Chinese Physics B*, *25*(6), 067105.
3. **Khidzir, S. M.**, Ibrahim, K. N., & Wan Abdullah, W. A. T. (2016). GW approximation study of late transition metal oxides: Spectral function clusters around Fermi energy as the mechanism behind smearing in momentum density. *Modern Physics Letters B*, *30*(14), 1650162.